AD_____

Award Number: W81XWH-F€ÆÆ̈Ëï Î ï

TITLE: Œ̈Úæç^¦•@̨Á⁄¦æ̨ą̃*Á⁄¦[*¦æ̨ Ḱ̈Úč å^ą̃*Á⁄æ̀*^c^åÆÖ¦˘*ÆÖ^¦ą̃c^¦ˆÁ̀•ą̃*Á́
Þæ̨[]æ̀cã̀¦^•Á̧Q̧Á́Ö¦^æ̀c⁄Ôæ̨&^¦Á́Öã̆*}[•ã̃Á̀æ̨åÁ⁄@¦æ̨}ˆÁ́

PRINCIPAL INVESTIGATOR: Úæ̃|Á̂ÔÈ⁄Y̧æ̨*Ê̂Ú̧@ȮÈ

CONTRACTING ORGANIZATION: P[̧æ̀åÁ̀Ẅ̨ą̃c^¦•ã̃ˆ
    Y̧æ̀@̨¸*¢}̧Ê̂Ö̂Ô̈Á̂Ǵ€í JÁ́

REPORT DATE: U&¢à^¦Á̂Ǵ€FG

TYPE OF REPORT: Annual Ù̆{{æ̀ˆ

PREPARED FOR: U.S. Army Medical Research and Materiel Command
        Fort Detrick, Maryland 21702-5012

DISTRIBUTION STATEMENT: Approved for public release; distribution unlimited

The views, opinions and/or findings contained in this report are those of the author(s) and should not be construed as an official Department of the Army position, policy or decision unless so designated by other documentation.

			Form Approved
REPORT DOCUMENTATION PAGE			*Form Approved* OMB No. 0704-0188

Public reporting burden for this collection of information is estimated to average 1 hour per response, including the time for reviewing instructions, searching existing data sources, gathering and maintaining the data needed, and completing and reviewing this collection of information. Send comments regarding this burden estimate or any other aspect of this collection of information, including suggestions for reducing this burden to Department of Defense, Washington Headquarters Services, Directorate for Information Operations and Reports (0704-0188), 1215 Jefferson Davis Highway, Suite 1204, Arlington, VA 22202-4302. Respondents should be aware that notwithstanding any other provision of law, no person shall be subject to any penalty for failing to comply with a collection of information if it does not display a currently valid OMB control number. **PLEASE DO NOT RETURN YOUR FORM TO THE ABOVE ADDRESS.**

1. REPORT DATE *(DD-MM-YYYY)* October 2012	2. REPORT TYPE Annual Summary	3. DATES COVERED *(From - To)* 15 September 2011 - 14 September 2012

4. TITLE AND SUBTITLE	5a. CONTRACT NUMBER
A Partnership Training Program: Studying Targeted Drug Delivery Using Nanoparticles In Breast Cancer Diagnosis and Therapy	5b. GRANT NUMBER W81XWH-10-1-0767
	5c. PROGRAM ELEMENT NUMBER
6. AUTHOR(S) Paul C. Wang, Ph.D.	5d. PROJECT NUMBER
	5e. TASK NUMBER
E-Mail: pwang@howard.edu	5f. WORK UNIT NUMBER

7. PERFORMING ORGANIZATION NAME(S) AND ADDRESS(ES) Howard University Washington, DC 20059	8. PERFORMING ORGANIZATION REPORT NUMBER

9. SPONSORING / MONITORING AGENCY NAME(S) AND ADDRESS(ES) U.S. Army Medical Research and Materiel Command Fort Detrick, Maryland 21702-5012	10. SPONSOR/MONITOR'S ACRONYM(S)
	11. SPONSOR/MONITOR'S REPORT NUMBER(S)

12. DISTRIBUTION / AVAILABILITY STATEMENT
Approved for Public Release; Distribution Unlimited

13. SUPPLEMENTARY NOTES

14. ABSTRACT
In the second year of this training grant, 11 faculty members, 7 postdocs, 4 graduate and 6 undergraduate students from 6 departments at the Howard University have been trained in the use of nanoparticles as targeted drug delivery vehicles for cancer diagnosis and therapy. Ten seminars and workshops in cancer, molecular imaging, and nanomedicine have been offered. The trainees have received hands-on training in MRI, optical imaging, cell biology lab techniques, and small animal handling. The two research projects have progressed well. We have improved controlling the size of liposome with a heat sonic method. We studied the stability of surface coating of quantum dots as a model for studying potential toxicity of nanoparticles. We have shown that A-dmDT(390)-scfbDb(PSMA), a single chain Fv fragments of antibody with diphtheria toxin, demonstrates good dual targeted imaging and therapeutic properties. We have shown that a contrast agent encapsulated in liposome with transferrin as a targeting ligand has higher uptake in breast cancer cells and in tumor bearing animals. This year, there are 11 research projects utilizing the facility of the Nanomedicine Core. The Core has become a synergy center, drawing multidisciplinary research using nanotechnology for cancer research.

15. SUBJECT TERMS
training, nanotechnology, breast cancer, diagnosis, therapy, imaging, drug delivery

16. SECURITY CLASSIFICATION OF:			17. LIMITATION OF ABSTRACT	18. NUMBER OF PAGES	19a. NAME OF RESPONSIBLE PERSON USAMRMC
a. REPORT U	b. ABSTRACT U	c. THIS PAGE U	UU	98	19b. TELEPHONE NUMBER *(include area code)*

Standard Form 298 (Rev. 8-98)
Prescribed by ANSI Std. Z39.18

Table of Contents

A Partnership Training Program – Studying Targeted Drug Delivery Nanoparticles in Breast Cancer Diagnosis and Therapy

I. INTRODUCTION

In this program, we proposed to establish a Nanomedicine Core to train faculty and students at Howard University to pursue molecular imaging of breast cancer using nanoparticles as targeted drug delivery vehicles. This is a partnership with the Johns Hopkins University In Vivo Cellular Molecular Imaging Center and the Nanotechnology Characterization Lab at NCI-Frederick. At Howard University, this partnership involves a multidisciplinary consortium of four departments: Radiology, Radiation Oncology, Molecular Biology and Biochemistry, and Electrical Engineering. The program has two components, a research component and a broad training component. The Howard University trainees will obtain training through collaborative research and by participation in a broad based training program. Renowned experts in nanomedicine and molecular imaging will participate in the training through mentoring research, seminars, workshops, and by offering laboratory internships. This transfer of nanomedicine techniques will support ongoing, long-term breast cancer research at Howard University. The major goal is to provide faculty trainees and their students at Howard with updated nanomedicine techniques to apply to independent breast cancer research, thus enhancing their ability to educate the next generation of scientists. The program objectives are:
1. Train new researchers in breast cancer using modern nanomedicine techniques.
2. Offer lectures, seminars, workshops, and laboratory internships in nanotechnology and molecular imaging.
3. Conduct two proposed research projects.
4. Establish a Nanomedicine Core to support long-term sustainable research.
5. Research concept development and submission of competitive grants in breast cancer imaging.

II. BODY

Molecular imaging and functional MRI continue to provide new insights into the etiology, diagnosis, and treatment of breast cancer. In clinic, these methods have made a significant impact in breast cancer diagnosis and in monitoring response to therapy. As our understanding of breast cancer advances, we further recognize the complexities of this disease and the urgent need for individualized characterization and treatment. Recent exciting advances in the application of MR methods for breast cancer research have resulted from the development of contrast agents (CAs) that generate receptor-targeted or molecular-targeted contrast. Targeted CAs can be directed to cell surface receptors using antibodies [1, 2] or 'smart' agents activated by specific enzymes, or based on the expression of detectable reporters [3, 4]. These molecular imaging capabilities, in combination with the strong functional imaging capabilities of MR methods, allow molecular-functional characterization of cancer and the physiological microenvironment of tumors [5]. Non-invasive MR can play an important role in the molecular-functional characterization of breast cancer for detection, drug delivery, development of therapeutics, and monitoring of treatment response. Lately, the development of nanotechnology has also had a dramatic impact on diagnosis and treatment [6-8]. Among many possible applications of nanotechnology in medicine, the use of various nanomaterials as pharmaceutical delivery systems for drugs, DNA, and imaging agents has gained increasing attention. Many nanoparticle-based drug delivery and drug targeting systems have been approved by FDA or are under development [9-11]. Their use aims to minimize drug degradation, prevent undesirable side effects, and increase drug bioavailability and the

fraction of drug dosage delivered to the pathological area.

In order to achieve the goals of this training program, we have proposed conducting two research projects and a broad-based training program to train researchers at Howard University in the field of the application of nanotechnology in targeted drug delivery. In conjunction with these activities, we also proposed establishing a University Nanomedicine Core to promote and facilitate campus-wide research and training. The following progress report is a summary of the accomplishments for the second year in the areas: (i) research, (ii) training, (iii) establishment of Nanomedicine Core, and (iv) alignment with the Statement of Work.

II.1. Research Projects

Project 1:   Study the physicochemical characteristics of nanoparticles as MR contrast agent delivery system with the dynamic contrast enhancement pattern for clinical applications

The use of nanoparticles for biomedical applications continues to grow rapidly, particularly in imaging and drug delivery applications. The extraordinary properties of nanoparticles, such as flexible composition, large surface to volume ratio, various shape and small size, and optical properties, contribute to the novel applications in diagnostic imaging and therapy [12-17]. Commonly used nanoparticles include liposomes, micelles, dendrimers, quantum dots, polymeric nanoparticles, gold nanoparticles and magnetic nanoparticles. The unique physical and chemical properties of a nanoparticle significantly influence its interactions with tissues and cells. Better understanding of these interactions will greatly assist in the design of smart drugs and targeted CAs delivery, with great potential for molecular-based diagnostics and therapeutics.

Liposome preparation and characterization.   In this study, we have constructed liposomal nanoparticles with contrast agents (CA), Magnevist (Mag) and Carboxyfluorescein (CF), as payloads. The NIR-labeled Transferring (Tf) was coupled to the fluorescently labeled liposomes (Lip) for targeted delivery of CAs to breast cancer cells (Figure 1). This year we continue to improve liposome preparation techniques by fusing different methods of preparation (sonication, homogenization, and heating) and protein conjugation (electrostatic interaction and covalent conjugation). The latest improved version of preparing liposomes is a temperature controlled sonication method followed by Tf covalent conjugation. We have established protocols to characterize physicochemical properties of nanoparticles, including size distribution, surface charge, encapsulation efficiency, and ligand linkage on the surface.
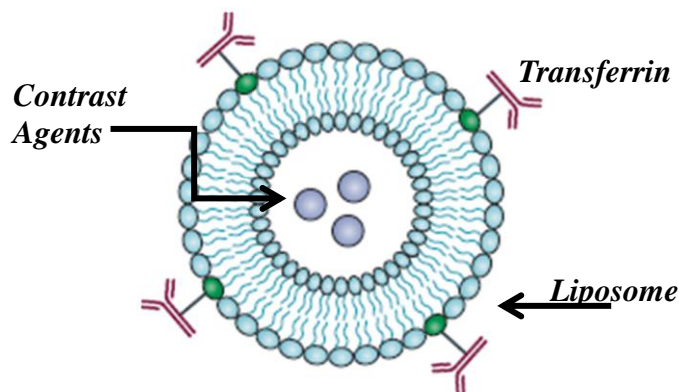
Figure 1. Schematic draw of the liposomal nanoparticle.

Liposomal nanoparticles in vitro uptake.   The CF-encapsulated, fluorescently labeled liposomes, with or without Tf coupled to the surface, were used to study the targeting specificity in vitro. The size of the liposome was 120-130 nm in diameter. The targeting efficiency of the probes (Tf-Lip-CA) was evaluated using MDA-MB-231-luc cells grown as monolayers in vitro. Flow cytometry showed that the cellular fluorescent intensities for Tf, Lip-CA, and Tf-Lip-CA were 1.8, 7.0 and 16 folds higher than untreated controls, respectively (Figure 2). Confocal microscopy showed a 1.5-2 fold increase of the cellular uptake of Tf conjugated probe compared to the uptake of dye only or liposome encapsulated with dye. The targeting specificity of the Tf moiety was studied by a blocking experiment, which has shown a 65% decrease in cellular uptake in cells that were pretreated with a 3-fold higher concentration of Tf for 1 hour.
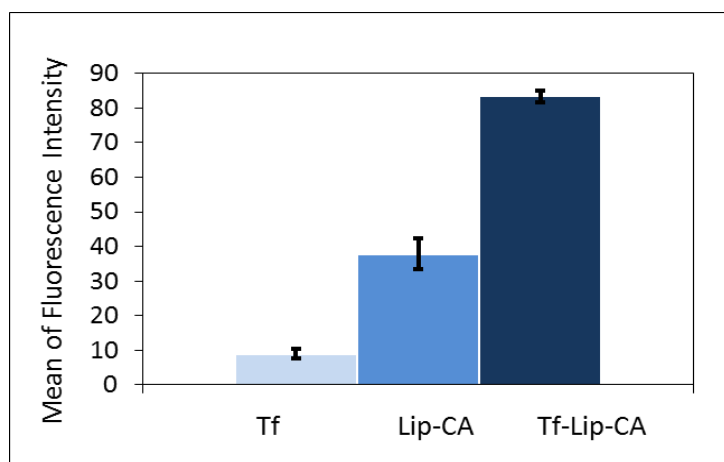
Figure 2. Mean of the flow cytometry intensity for Tf, Lip-CA, and Tf-Lip-CA.

Study toxicity of nanoparticles   For any nanoparticle to be successfully used in clinic, it has to overcome the potential toxicity in the body. After administering nanoparticles in the body, the nanoparticles may be recognized and captured by the reticuloendothelial system (RES). Capture by the RES may lead to loss of the functionalities of nanoparticles and aggregation in the body. The aggregated nanoparticles may be entrapped in the liver, lung and other part of body due to capillary occlusion. Toxicity can be as a result of degradation of nanoparticles, releasing toxic material such as cadmium in quantum dots. To avoid recognition by the RES, nanoparticles are commonly modified with various surface coatings. Trioctylphosphine oxide (TOPO) is a commonly used surface coating material for semiconductor quantum dot nanocrystals (QDs). We have used NMR spectroscopy to monitor the stability of TOPO coatings on QDs as a model to demonstrate the potential toxicity of nanoparticles for biomedical imaging. This study has shown that TOPO-QDs are relatively unstable, and TOPO can be cleaved from QDs in the presence of nucleophilic agents such as thiol, which is widely distributed in tissue and body fluids. This research provides preliminary information about the potential risks presented by the degradation of nanoparticles in physiological systems. The detailed experimental procedures and results were included in a manuscript to be submitted to the Journal of Colloid and Interface Science (Appendix 3.1).

Efficacy of nanoparticle targeted delivery   Using nanoparticle to deliver drugs or CAs to target a specific biomarker has great potential for improving therapeutic effect and diagnostics specificity and

sensitivity. Near-infrared fluorescence (NIRF) imaging is a sensitive technique for monitoring the uptake of molecular probes at the molecular level. In this study, we tested the delivery efficiency of tumor-seeking fluorescent nanoparticles by attaching more than one targeting moiety. The probes consisted of one or two glucosamine (GlcN) moieties conjugated to dye (cypate (cyp)). Both cyp-GlcN and cyp-2GlcN NIRF probes exhibited good tumor-targeting properties in cancer cell cultures and live mice, but the cyp-2GlcN probe, with two targeting moieties, showed the higher uptake with good retention characteristics in vivo. The results of this work were published in the Journal of Molecular Imaging and Biology (Appendix 3.2).

Another approach to improve the efficacy of delivering liposomal nanoparticles is using pH-sensitive peptides as targeting ligands. In solid tumors, the increased glucose catabolism results in production of lactate and H^+ ions, which are pumped out into the extracellular space producing an acidic environment. In this study, we used a pH-sensitive nanoprobe to demonstrate good tumor-targeting properties in breast cancer xenografts in vivo (Figure 3). This pH-sensitive peptide can either serve as an anchor for nanoparticles to attach to the cancer cell membrane or insert nanoparticles into the cell. The pH-sensitive property has potential for improving targeted drug delivery. The preliminary results of this study were reported on the Howard University Health Sciences Research Day 2012 (Appendix 3.3).
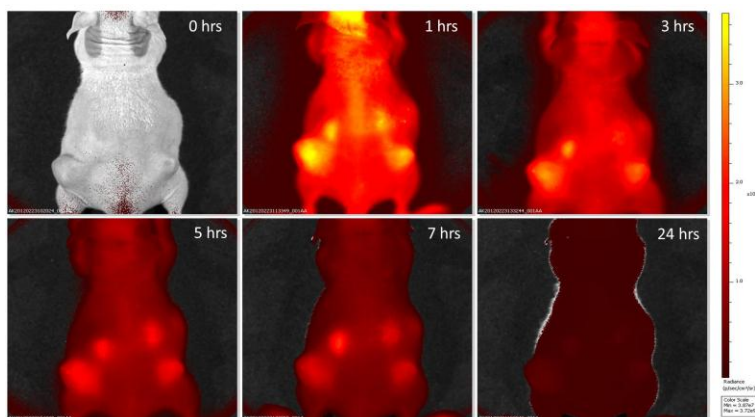
Figure 3. Optical detection of tumor after i.v. administration of pHLIP containing nanoparticles.

Project 2:   Development of multifunctional nanoparticles for breast cancer diagnosis and treatment – Using anti-VEGFR-2 immunotoxin as dual purpose ligand and chemotherapeutics as encapsulated payload

Angiogenesis is fundamental to sustaining the growth, invasion and metastasis of tumors [18,19]. Vascular endothelial growth factors (VEGF)/receptors are the primary and most potent inducers of tumor angiogenesis [20,21]. Members of the VEGF family (VEGF-A to F, PIGF) stimulate cellular responses by binding to the receptors (VEGFR-1 to 3) on the cell surface, inducing dimerization and activation through transphosphorylation [19-21]. Activation of the VEGF signal pathway promotes endothelial cell survival, proliferation, migration and vascular permeability. VEGFR-2 appears to mediate almost all of the known cellular responses to VEGF and is a critical target for tumor suppression [19-22]. Most of the VEGF inhibitors inhibit the VEGF signal pathway, rather than kill the endothelial cells directly. In this study, we proposed using a diphtheria immunotoxin fused with single-chain Fv (scFv) fragments of

monoclonal antibodies (mAbs), to achieve targeted cell killing while at the same time maintaining the low non-target cell toxicity. In this study we hypothesize that anti-VEGFR-2 immunotoxin nanoparticles will achieve synergistic efficacy through combined anti-angiogenics, chemotherapeutic cytotoxicity and targeted delivery while limiting their nonselective toxicity.

Tumor targeting and therapeutic potential of the immunotoxin. This year, we finished a proof-of-principle study using a bivalent immunotoxin generated by fusing a fold-back single-chain diabody derived from the Fv fragments of an anti-PSMA monoclonal antibody with a truncated diphtheria toxin (DT) containing the activity and translocation domains [A-dmDT390-scfbDb(PSMA)]. In this study, a PSMA-positive and a PSMA-negative cancer cell lines were treated with immunotoxin A-dmDT390-scfbDb(PSMA) to study the tumor targeting specificity and therapeutic potential of the immunotoxin. Cellular accumulation of A-dmDT390-scfbDb(PSMA) increased with increasing incubation times and concentrations in LNCaP cells. The proportion of apoptotic LNCaP cells increased upon incubation with increasing doses of the fold-back immunotoxin. Optical imaging and MRI with the Alexa Fluor 680-labeled A-dmDT390-scfbDb(PSMA) confirmed the specific targeting and therapeutic efficacy of this immunotoxin towards PSMA-positive LNCaP solid tumor xenografts in athymic nude mice. The results of this work were submitted to the Journal of Advanced Healthcare Materials (Appendix 3.4). Currently, we are testing an anti-murine (VR16) and an anti-human (1121) anti-VEGFR-2 bivalent scFv (biscFv) fold-back immunotoxin by fusing deletion-mutated diphtheria toxin (dmDT390) with fold-back biscFv diabody. We will test this construct in breast cancer cells and animal models in the coming year.

Antimetastatic effect of multifunctional nanoparticles. The current trend of nanoparticle-based clinical applications is the combination of 'imaging' and 'therapeutic' agents as one system to achieve both imaging and therapeutic purposes at the same time. In this study, we tested an option of adding an antimetastatic functionality, which can be used in the final nanoparticle construct. We probed the potential payload, gadolinium metallofullerenol nanoparticles (f-NPs), for their antimetastasis activity. We demonstrated that f-NPs inhibited the production of matrix metalloproteinase (MMP) enzymes and further interfered with the invasiveness of cancer cells in vitro. In the animal study, the invasive primary tumor treated with f-NPs showed significantly less metastasis to the ectopic site along with the decreased MMP expression. Based on this data, we conclude that f-NPs have antimetastasis effects and speculate that utilization of f-NPs may provide a new strategy for the treatment of tumor metastasis. The results of this work were published in the Journal of Nanomedicine: Nanotechnology, Biology and Medicine (Appendix 3.5).

II.2. Broad Based Training Components

The Molecular Imaging Laboratory has regular bi-weekly group meetings, journal clubs, and seminars. Some seminars have been arranged through webinars sponsored by the imaging vendors, thus giving an opportunity to the Howard University community to attend seminars given by experts from around the world, followed by very productive and fruitful local discussions. The bi-weekly group meetings engage participants in discussing the current status of research projects, analyzing the experimental issues of the current research, review progress, and exchange ideas, and have been the primary mode of interaction between Howard researchers and collaborating experts. Through participation in the Imaging Core-sponsored seminars and workshops, and interaction with Imaging Core staff, a multidisciplinary nanomedicine research community has been established and many fruitful exchanges of research ideas generated. Significant common synergies of interests have been identified,

and much multidisciplinary research collaboration will be developed. The faculty trainees have also attended seminars at JHU ICMIC. The HU and JHU partnership leaders have been coordinating the training efforts through meetings and emails. The participants of the program have submitted grants to NIH, CDMRP, and NSF together with the partnership leaders. We believe that trainees engaged in this training program gain the interdisciplinary knowledge and skills they need to lead multidisciplinary research in the area of nanomedicine. The seminars and workshops organized at Howard University, as well as at the Johns Hopkins University and other institutions, are listed as following:

Seminars and workshops

1. Writing for Biomedical Publication. Chris Papasian, Ph.D., September 26, 2011, Howard University Health Science Research Development Symposium.
2. Neurospectroscopy: the past, present, and future. Oluseyi Awodele, 3rd year medical student. October 4, 2011, Radiology Department, Howard University Hospital.
3. An Introduction to Flow Cytometry. Ina Schulte, Ph.D., Abcam Scientific, October 11, 2011, webinar broadcasted in the Molecular Imaging Laboratory, Howard University Hospital Cancer Center.
4. Mechanism and uses of a membrane peptide that target tumors and other acidic tissues in vivo. Chung-Shieh Wu, Ph.D., November 3, 2011, Howard University Hospital Cancer Center.
5. The Road to Research Advancement. Thomas A. Mellman, M.D., November 17, 2011, Howard University College of Medicine.
6. Determining the Impact of New Therapeutic Approaches: Advancing Imaging in Animals. Matthias Nahrendorf, M.D., Ph.D. and Patrick McConville, Ph.D. sponsored by PerkinElmer, December 7, 2011, webinar broadcasted in the Molecular Imaging Laboratory, Howard University Hospital Cancer Center.
7. Not Networking 101—Building Relationships for Success. Nick Oswald, Ph.D., December 14, 2011, webinar broadcasted in the Molecular Imaging Laboratory, Howard University Hospital Cancer Center.
8. Targeting Tumor Acidity. Yana Reshetnyak, Ph.D., January 24, 2012, Howard University Hospital Cancer Center.
9. Key Secrets of Spectroscopy for Life Sciences. Robert R. Alfano, Ph.D. and Stavros Demos, Ph.D. sponsored by BioOptics World, January 31, 2012, webinar broadcasted in the Molecular Imaging Laboratory, Howard University Hospital Cancer Center.
10. Computational Biology & Bioinformatics, Biomedical Imaging and Proteomics. Drs. Paul C. Wang, William M. Southerland, Sergei Nekhai, Core Laboratories RCMI workshop, January 31 & February 1, 2012, Howard University.
11. Two-photon microscopy: How, why and what. John M. Girkin, Ph.D. sponsored by BioOptics World, February 7, 2012, webinar broadcasted in the Molecular Imaging Laboratory, Howard University Hospital Cancer Center.
12. A Ligand-Centric Approach for Function Prediction. Sona Vasudevan, Ph.D., March 8, 2012, Howard University College of Medicine.
13. Beyond the Diffraction Limit: Advances and Applications of Super-Resolution Imaging. Joerg Bewersdorf,Ph.D., Catherine Galbraith, Ph.D. & Markus Sauer, Ph.D. sponsored by Leica Microsystem, March 28, 2012, webinar broadcasted in the Molecular Imaging Laboratory, Howard University Hospital Cancer Center.
14. The Future of Molecular Imaging, Sam Gambhir, M.D., Ph.D. sponsored by VisualSonics, May 23, 2012, webinar broadcasted in the Molecular Imaging Laboratory, Howard University Hospital Cancer

Center.

15. In vivo 3D fluorescence imaging. Brad Rice, Ph.D. sponsored by PerkinElmer, May 31, 2012, webinar broadcasted in the Molecular Imaging Laboratory, Howard University Hospital Cancer Center.
16. Assessment of MRI And FT-IR Studies of Cartilage Degradation Through Multivariate Analysis. Ping-Chang Lin, Ph.D., June 1, 2012, Howard University Hospital Cancer Center.
17. Optical Sectioning using Light Sheet Microscopy: In Vivo Imaging with Astounding Resolution. Ernst H. K. Stelzer, Ph.D., Pavel Tomancak, Ph.D. & Lars Hufnagel, Ph.D. sponsored by Science/AAAS, June 14t, 2012, webinar broadcasted in the Molecular Imaging Laboratory, Howard University Hospital Cancer Center.
18. Nanoliposomes: Preparation and Analysis. Alexandru Korotcov, Ph.D., August 1, 2012, Molecular Imaging Laboratory, Howard University Hospital Cancer Center.
19. Quantification of In Vivo Imaging Pre-Clinical Models Using the ICON™ Compact, High-Performance MRI System. Mat Brevard, Ph.D & Tonya Coulthard, Ph.D. sponsored Bruker Biospin and Aspect Imaging, August 22, 2012, webinar broadcasted in the Molecular Imaging Laboratory, Howard University Hospital Cancer Center.

Seminars and workshops at John Hopkins University and other institutes

1. Imaging Metabolic Signatures of Cancer-Induced Cachexia. Marie-France Penet, Ph.D., October 5, 2011, Dept. of Radiology, John Hopkins University, Baltimore, MD.
2. Diffusion Weighted MRI - Where Are We in the Clinic? Nandita deSouza, M.D., Ph.D., October 14, 2011, Dept. of Radiology, John Hopkins University, Baltimore, MD.
3. Lipid-based Nanoparticles and Triggered Chemotherapy. Robert Blumenthal, Ph.D., November 8, 2011, National Institutes of Health, Bethesda, MD.
4. Molecular Cancer Imaging: New Optical Diagnostic Technologies and Beyond. Hisataka Kobayashi, M.D. Ph.D., February 15, 2012, Dept. of Radiology, John Hopkins University, Baltimore, MD.
5. Trials on Systemic Delivery of Cancer Therapeutics via Targeted Nanoparticles. Esther H. Chang, Ph.D., February 21, 2012, National Institutes of Health, Bethesda, MD.
6. Quantification of Tumor Vasculature Heterogeneity by DCE-MRI. Wenlian Zhu, Ph.D., February 29, 2012, Dept. of Radiology, John Hopkins University, Baltimore, MD.
7. Quantum Dots and Single Molecule Detection Enable Highly Sensitive Screening of Genetic Cancer Biomarkers. Jeff T.H. Wang, Ph.D., April 17, 2012, National Institutes of Health, Bethesda, MD.
8. Two-component Nanodelivery for Enhanced Internalization of Theranostics; Click Therapy on Her2/neu Overexpressing Breast Cancer. Sudath Hapuarachchige, Ph.D., May 2, 2012, Dept. of Radiology, John Hopkins University, Baltimore, MD.
9. Controllable Self-Assembly of Inorganic Nanocrystals for Biological Applications. Zhihong Nie, Ph.D., May 15, 2012, National Institutes of Health, Bethesda, MD.
10. Cutting-Edge Imaging Technologies and Strategies in Preclinical Small Animal Research. Carestream Molecular Imaging workshop. May 30, 2012, Hyatt Regency Bethesda, MD.

II.3. Nanomedicine Core

It is essential for Howard University to establish a basic infrastructure that is capable of supporting a sustainable long-term research program in the field of molecular imaging of breast cancer and nanomedicine. This infrastructure is necessary in order to provide the researchers with tools to

perform the proposed researched projects, as well as to provide a broader research training experience. In the second year of the proposed training program, we continued the expansion of the Nanomedicine Core and the collaboration with Howard University Nanoscience Facility. There are 11 research projects that have been supported by the Nanomedicine Core, including projects in the initial phase of research. There are 11 faculty members from 6 departments and 5 scientists from the neighboring institutions, including NIST, NIH and Georgetown University, who use the core facility to conduct these research projects. There are 6 undergraduate students, 4 graduate students and 7 postdoctoral fellows working with principle investigators on various research projects. This year, we added an additional project titled "Tumor-Targeted pH-Sensitive Nanoparticulate MRI Agent with Enhanced Contrast and Reduced Side Effect". This multidisciplinary collaborative project explore the possibility of developing a new 'smart' pH-sensitive Gd-nanoparticle, synthesized by a novel spray drying technology currently developed at Howard University. The preliminary results demonstrate that pH-sensitive Gd-nanoparticle has potential to be used in clinic as a positive contrast agent with higher proton relaxivities and signal intensities compared to non-specific Gd chelated contrast agents. The Nanomedicine Core not only has provided state-of-the-art instruments, but also has provided technical expertise and has become a synergy center in nanomedicine research at Howard University.

In 2011, Howard University Health Sciences developed a Research Strategy Plan that outlines the direction of the Enterprise for the future, and envisions the development of biomedical research at Howard University to its full potential, with emphasis on health disparities research. This future plan embraces new research disciplines such as proteomics, computational biology, nanomedicine and genomics. To execute the University Research Strategy Plan and its commitment to the nanomedicine research, the University will start construction of a new Interdisciplinary Research Building in 2013 in which there will be a designated space for Nano Bioimaging research. There will be lab space for nanomaterial fabrication with ultrastructure imaging and analytical instrument for physicochemical characterization of nanoparticles, molecular biology labs with incubators and hoods for cell culture and flow cytometry, and imaging suites for confocal microscope and future PET/CT machine.

II.4. Statement of Work Summary

The accomplishments aligned with the Statement-of-Work occurred in this reporting period is listed as following:

Research Component

Task 1.   To conduct Research Project 1 "Study the physicochemical characteristics of nanoparticles as MR contrast agent delivery system with the dynamic contrast enhancement pattern for clinical applications" (months 1-48).

  a.   Purchase supplies for cell culture and materials for nanoparticles (months 1-2) (completed).
  b.   Construct liposome (Lip) nanoparticles with transferrin (Tf) as the ligand and encapsulated Gd-based MRI contrast agent (CA) inside as payload (months 3-9) (completed).
  c.   Characterize the physicochemical properties of nanoparticles, including size distribution, surface charge, encapsulation efficiency, and Tf linkage on the surface. Some of the measurements will be done at NCL, NCI-Frederick (months 6-12) (completed).

d. Study targeting efficiency of the liposome nanoparticle using MDA-MB-231 cells. Study the interactions of nanoparticles with breast cancer cells (months 13-24) (in progress).

e. Study the correlation of the dynamic contrast enhancement (DCE) pattern with the distribution of Tf-liposome nanoparticles in tumor xenografts. Both MR and optical imaging will be used (30 mice) (months 25-36).

f. Evaluate the potential clinical applications of the DCE pattern, focusing on the relationship between the DCE pattern and the tumor features of TfR expression level, permeability of neovasculatures, vascular density, tumor growth and necrosis (months 25-40).

g. Data analysis and preparation of manuscripts for publication (months 40-48)

Task 2. To conduct Research Project 2 "Develop multifunctional nanoparticles for breast cancer diagnosis and treatment – using anti-VEGFR-2 immunotoxin as dual purpose ligand and chemotherapeutics as encapsulated payload" (months 1-48).

a. Purchase supplies and prepare for the study (months 1-2) (completed).

b. Define the efficacy of the anti-murine anti-VEGFR-2 immunotoxin in endothelial cell killing and vascular permeability increase in animal models (months 3-18) (in progress).

c. Construct and characterize the targeted anti-VEGFR-2 immunotoxin multifunctional nanoparticles. Some of the work will be done at NCL (months 13-18) (in progress).

d. Determine the biodistribution, pharmacokinetics and toxicity of the nanoparticles in healthy mice (8) and mice bearing with tumor xenografts (22). Optical imaging will be used. Measurements of biodistribution will be done at NCL and HNF (months 19-40) (in progress).

e. Define the synergistic effects of the targeted delivery, anti-angiogenics and chemotherapeutics in breast cancer animal models. Histological staining will be used to study the tumor vasculature (months 25-40).

f. Data analysis and preparation of manuscripts for publication (months 40-48).

Task 3. Research concept development and submission of competitive grants in breast cancer targeted imaging and therapy (months 37-48).

Broad Training Component

Task 4. Provide opportunities to the faculty trainees in Howard University to update knowledge of nanomedicine (months 1-48) (in progress for all tasks).

a. Biweekly group meetings at the Molecular Imaging Lab (months 1-48)

b. Monthly Seminar series at Howard University Cancer Center to be presented by the mentors and invited speakers (months 1-48).

c. Johns Hopkins University ICMIC Seminar Series organized by Dr. Bhujwalla (months 1-48).

d. To attend the biweekly Nanobiology Program Seminar Series at NCI-Frederick organized by Dr. Blumenthal (months 1-48).

e. Annual scientific meetings with mentors and trainees.

Task 4. Train Howard faculty in advanced nanomedicine lab techniques (in progress for all tasks).

a. Laboratory internships at the Johns Hopkins University and NCL, topics include molecular imaging and nano characterization techniques, 2-4 days each (months 1-36).
b. Workshop series. Topics include MR and optical imaging, SEM/TEM/AFM, optical instrumentation, drug design and liposome (months 1-48).

Task 6. Administrative and communication affairs (coordinated by Drs. Wang and Bhujwalla) (Months 1-48) (in progress for all tasks).

a. Status reports (quarterly and annual reports)
b. Research progress review (quarterly)
c. Administrative meetings (biannually meetings)
d. Coordination of seminars, workshops, and laboratory internships

III. KEY RESEARCH ACCOMPLISHEMENTS

- Established a new, improved method of making well-controlled liposomes using a temperature controlled sonication followed by Tf covalent conjugation.
- The MDA-MB-231-luc cellular uptake of Tf-conjugated probe in vitro is more efficient compare with the uptake of dye or non-targeted liposomes. The uptake of Tf, Lip-CA, and Tf-Lip-CA was 1.8, 7.0 and 16 folds higher compared with untreated controls
- Studied the toxicity of nanoparticles using a NMR spectroscopy method to monitor the nanoparticles' stability. TOPO was shown to be cleaved from nanoparticles in the presence of a nucleophilic agent such as thiol, which is widely distributed in tissue and physiological fluids, degrading the nanoparticles in physiological systems and increasing risks of nanotoxicity.
- Investigated the delivery efficiency of tumor-seeking fluorescent nanoparticles by attaching more than one targeting moiety. Both cyp-GlcN and cyp-2GlcN NIRF probes exhibited good tumor-targeting properties in cancer cell cultures and live mice, but the cyp-2GlcN probe, with two targeting moieties, showed the highest uptake (almost double uptake) with good retention characteristics in vivo.
- Improved the efficacy of tumor-targeted delivery of liposomal nanoparticles with a pH-sensitive peptide. The pH-sensitive nanoprobe demonstrated good tumor-targeting properties in breast cancer xenografts in vivo and can be used for targeted drug delivery, detecting small tumors, performing diagnostic imaging, and treating acidic disease tissue.
- Optical imaging and MRI with the Alexa Fluor 680 labeled bivalent immunotoxin with a truncated diphtheria toxin [A-dmDT390-scfbDb(PSMA)] showed the specific targeting and therapeutic efficacy of this immunotoxin towards solid tumor xenografts in athymic nude mice.
- Gadolinium metallofullerene nanoparticle has shown an antimetastatic effect in tumor bearing mouse model. The gadolinium metallofullerene nanoparticles inhibited the production of matrix metalloproteinase enzymes and further interfered with the invasiveness of cancer cells, thus showing an antimetastatc activity.

IV. REPORTABLE OUTCOMES

Publications

1. Korotcov AV, Ye YP, Chen Y, Zhang FY, Huang S, Lin S, Sridhar R, Achilefu S, Wang PC. Glucosamine Linked Near-infrared Fluorescent Probes for Imaging of Solid Tumor Xenografts. Mol. Imaging and Biology. 14(4):443-51, 2012. PMID21971932, PMC3288187.
2. Meng H, Xing GM, Blanco E, Song Y, Zhao L, Sun BY, Li XD, Wang PC, Korotcov A, Li W, Liang XJ, Chen CY, Yuan H, Zhao F, Chen Z, Sun T, Chai ZF, Farrari M, Zhao YL. Gadolinium Metallofullerenol Nanoparticle Inhibits Cancer Metastasis through Matrix Metalloproteinase Inhibition: Imprisoning Instead of Poisoning Cancer Cells. Nanomedicine: Nanotechnology, Biology and Medicine 8(2):136-146, 2012. PMID 21930111.
3. Zhang FY, Shan L, Liu YY, NevilleD, Woo JH, Chen Y, Korotcov AV, Lin S, Huang S, Sridhar R, Liang W, Wang PC. An Anti-PSMA Bivalent Immunotoxin Exhibits Specificity and Efficacy for Prostate Cancer Imaging and Therapy. *(Submitted to Advanced Health Materials, 09/2012)*
4. Wang TX, Korotcov AV, Sridhar R, Chen Y, Mitchell JW, and Wang PC. A 31P NMR Study of TOPO Release from TOPO-coated Quantum Dots. *(To be submitted to the Journal of Colloid and Interface Science 10/2012)*

Presentations

1. Wang PC. Nanoparticles as Targeted Drug Delivery Vehicles for Molecular Imaging and Chemotherapy Applications. Hebei People's Hospital, Shijiazhuang, Hebei, China, Sep 13, 2011.
2. Wang PC. Nanoparticles as Targeted Drug Delivery Vehicles for Molecular Imaging and Chemotherapy Applications. Peking Union Medical College, Beijing, China, Sep 15, 2011.
3. Wang PC. Applications of Nanoparticles for In Vivo Imaging. Institute of Biophysics, Chinese Academy of Sciences, Beijing, China, Sep 16, 2011.
4. Wang PC. Nanoparticles as Targeted Drug Delivery Vehicles for Molecular Imaging and Chemotherapy Applications. Chinese National Center for Nanoscience and Nanotechnology, Beijing, China, Sep 16, 2011.
5. Wang PC. Nanoparticles as Targeted Drug Delivery Vehicles for Molecular Imaging and Chemotherapy Applications. University of Rhode Island, Kingston, RI, November 18, 2011.
6. Wu CS, Huang S, Korotcov AV, Lin S, Andreev OA, Reshetnyak YK, Wang PC. pH Sensitive Nanoprobe for Tumor Targeting. Howard University Health Sciences Research Day 2012, Howard University, Washington, DC, April 13 2012, p. 21.
7. Lin S, Korotcov A, Wu CS, Oh L, Wang PC. In vivo and ex vivo brain and spine magnetic resonance imaging in multiple sclerosis mouse model. Howard University College of Medicine, Research Day Symposium, April 13, 2012
8. Wang PC, Wang TX, Korotcov AV, Sridhar R, Chen Y, Mitchell J. Study of TOPO-Quantum Dot Degradation by 31P NM, The 6th International Conference on Nanotoxicology, Beijing, September 4-7, 2012.

Grants

1. NIH/NCI R21 07/12-06/14
   Enhance mTOR-Targeting for Cancer Imaging and Therapy

Yunpeng Ye (PI), Paul Wang (co-PI) (not funded)
2. NIH/NCI R03 07/12-06/14
   Simultaneous inhibition of integrin $\alpha_v\beta_3$ and mTOR for pancreatic cancer therapy
   Yunpeng Ye (PI), Paul Wang (co-PI) (not funded)
3. US Army Prostate Cancer Idea Development Award 09/12-08/14
   Dual targeting of integrin $\alpha v\beta 3$ and mTOR for optical imaging and therapy of prostate cancer
   Yunpeng Ye (PI), Paul Wang (co-PI) (not funded)
4. NSF/Biomaterials Program 07/01/2012 – 06/30/2015
   Tumor-Targeted pH-Sensitive Nanoparticulate MRI Agent with Enhanced Contrast and Reduced Side Effect
   Tongxin Wang (PI), Alexandru Korotcov (co-PI), Ayele Gugssa (co-PI), and Laurence Chow (co-PI) (not funded)
5. NCRR/NIH/CTSA (part) GHUCCTS TTR 07/01/2012 – 06/30/2013
   Dynamic contrast enhanced MRI of tumor using targeted nanoparticles
   Alexandru Korotcov (PI), Leroy Williams (PI) (not funded)
6. NIH 1UL1RR031975 (Verbalis & Mellman) 07/01/2012-06/30/2013
   Georgetown-Howard Universities Center for Clinical and Translational Science (GHUCCTS)
   Pilot Project
   A collaborative study using primary prostate cells and their reprogramming for the study of progression to castrate resistant prostate cancer
   Chris Albanese (PI), Alexandru Korotcov (co-PI) (not funded)

V. CONCLUSIONS

In the second year of this program, the two research projects progressed well. We have modified the liposome preparation method, achieving better control on liposomal formation. The Tf in the new construct is attached by covalent bonding, improving the stability of liposomal nanoparticles. The Tf conjugated liposomal nanoparticles exhibited a significant increase in the in vitro cellular uptake compared to the uptake of dye or non-targeted liposomes. A toxicity study using NMR spectroscopy method showed that TOPO, a commonly used protective layer over quantum dots, can be cleaved from nanoparticles in the presence of physiological fluids, degrading the nanoparticles in physiological systems and increasing risks of nanotoxicity. In addition, we tested two different approaches of improving nanoparticle delivery efficacy. Doubling the number of targeting moieties increases the uptake of the probe in cells and in animal solid tumor model. Moreover, we showed that a pH sensitive peptide can be used as an effective ligand targeting acidic tumor environment, facilitating insertion of nanoparticle to the cancer cell membrane. We have completed a proof-of-principle study confirming the tumor targeting and therapeutic potentials of a bivalent immunotoxin generated by fusing a fold-back single-chain diabody derived from the Fv fragments of an anti-PSMA monoclonal antibody with a truncated diphtheria toxin containing the activity and translocation domains [A-dmDT390-scfbDb(PSMA)]. We have been working on anti-murine (VR16) and an anti-human (1121) anti-VEGFR-2 bivalent scFv (biscFv) fold-back immunotoxin synthesis. We have also shown anti-metastatic effect of gadolinium metallofullerene nanoparticles.

For the broad training component, the faculty members, and graduate and undergraduate students from different departments at Howard University have been trained in the use of nanoparticles as targeted drug delivery vehicles for cancer diagnosis and therapy. A total of 29 seminars and webinars, workshops and symposia in cancer, molecular imaging and nanomedicine have been offered. The

training activities have been coordinated by partnership leaders from Howard and John Hopkins Universities. This training program helps the participants gain useful interdisciplinary knowledge and skills to conduct breast cancer research using nanotechnology.

This year, the Nanomedicine Core supported 11 research projects including projects in the initial phase of research. There are 11 faculty members from 6 departments and 5 scientists from the neighboring institutions, including NIST, NIH and Georgetown University, who use the core facility to conduct these research projects. There are 6 undergraduate students, 4 graduate students and 7 postdoctoral fellows working with principle investigators in these projects. The Nanomedicine Core has provided training and research opportunities for the faculty and students at Howard University to conduct breast cancer research using state-of-the-art nanotechnology.

VI. References

1. Artemov D, Mori N, Okollie B, Bhujwalla ZM. MR molecular imaging of the Her-2/neu receptor in breast cancer cells using targeted iron oxide nanoparticles. Magnetic Resonance in Medicine 49 (3): 403-408, 2003.
2. Artemov D, Bhujwalla ZM, Bulte JW. Magnetic Resonance Imaging of Cell Surface Receptors Using Targeted Contrast Agents Current Pharmaceutical Biotechnology 5 (6): 485-494, 2004.
3. Cohen B, Dafni H, Meir G, Harmelin A, Neeman M. Ferritin as an Endogenous MRI Reporter for Noninvasive Imaging of Gene Expression in C6 Glioma Tumors. Neoplasia 7 (2): 109-117, 2005.
4. Cohen B, Ziv K, Plaks V, Israely T, Kalchenko V, Harmelin A, Benjamin LE, Neeman M. MRI detection of transcriptional regulation of gene expression in transgenic mice. Nat Med 13 (4): 498-503, 2007.
5. Gillies RJ, Raghunand N, Karczmar GS, Bhujwalla ZM. MRI of the tumor microenvironment. Journal of Magnetic Resonance Imaging 16 (4): 430-450, 2002.
6. Ferrari M. Cancer nanotechnology: opportunities and challenges. Nat Rev Cancer 5 (3): 161-171, 2005.
7. Riehemann K, Schneider SW, Luger TA, Godin B, Ferrari M, Fuchs H. Nanomedicine - Challenge and Perspectives. Angewandte Chemie International Edition 48 (5): 872-897, 2009.
8. Sahoo SK, Parveen S, Panda JJ. The present and future of nanotechnology in human health care. Nanomedicine: Nanotechnology, Biology and Medicine 3 (1): 20-31, 2007.
9. Torchilin V. Targeted pharmaceutical nanocarriers for cancer therapy and imaging. The AAPS Journal 9 (2): E128-E147, 2007.
10. Faraji AH, Wipf P. Nanoparticles in cellular drug delivery. Bioorganic & Medicinal Chemistry In Press, Corrected Proof.
11. Gil PR, Parak WJ. Composite Nanoparticles Take Aim at Cancer. ACS Nano 2 (11): 2200-2205, 2008.
12. Xia Y, Yang P, Sun Y, Wu Y, Mayers B, Gates B, Yin Y, Kim F, Yan H. One-Dimensional Nanostructures: Synthesis, Characterization, and Applications. Advanced Materials 15 (5): 353-389, 2003.
13. Alivisatos AP. Semiconductor Clusters, Nanocrystals, and Quantum Dots. Science 271 (5251): 933-937, 1996.
14. Elghanian R, Storhoff JJ, Mucic RC, Letsinger RL, Mirkin CA. Selective Colorimetric Detection of Polynucleotides Based on the Distance-Dependent Optical Properties of Gold Nanoparticles. Science 277 (5329): 1078-1081, 1997.
15. Cao YC, Jin R, Mirkin CA. Nanoparticles with Raman Spectroscopic Fingerprints for DNA and RNA Detection. Science 297 (5586): 1536-1540, 2002.
16. Klostranec J M, Chan WCW. Quantum Dots in Biological and Biomedical Research: Recent Progress and Present Challenges. Advanced Materials 18 (15): 1953-1964, 2006.
17. Hirsch LR, Stafford RJ, Bankson JA, Sershen SR, Rivera B, Price RE, Hazle JD, Halas NJ, West JL. Nanoshell-mediated near-infrared thermal therapy of tumors under magnetic resonance guidance. Proceedings of the National Academy of Sciences of the United States of America 100 (23): 13549-13554, 2003.
18. Stefanini M, Wu F, Mac Gabhann F, Popel A. A compartment model of VEGF distribution in blood, healthy and diseased tissues. BMC Systems Biology 2 (1): 77, 2008.
19. Schenone S, Bondavalli F, Botta M. Antiangiogenic Agents: an Update on Small Molecule VEGFR Inhibitors. Current Medicinal Chemistry 14 (23): 2495-2516, 2007.
20. Kiselyov A, Balakin KV, Tkachenko SE. VEGF/VEGFR signalling as a target for inhibiting angiogenesis. Expert Opinion on Investigational Drugs 16 (1): 83-107, 2007.

21. Veeravagu A, Hsu AR, Cai W, Hou LC, Tse VCK, Chen X. Vascular Endothelial Growth Factor and Vascular Endothelial Growth Factor Receptor Inhibitors as Anti-Angiogenic Agents in Cancer Therapy. Recent Patents on Anti-Cancer Drug Discovery 2 (1): 59-71, 2007.

22. Lu D, Jimenez X, Zhang H, Wu Y, Bohlen P, Witte L, Zhu Z. Complete Inhibition of Vascular Endothelial Growth Factor (VEGF) Activities with a Bifunctional Diabody Directed against Both VEGF Kinase Receptors, fms-like Tyrosine Kinase Receptor and Kinase Insert Domain-containing Receptor. Cancer Res 61 (19): 7002-7008, 2001.

VII. APPENDICES

1. Research Projects Supported by the Nanomedicine Core
2. Personnel received pay for the research
3. Students Participated in Nanomedicine Core Supported Research Projects
4. Reprints of Publication
   4.1. Wang TX, Korotcov AV, Sridhar R, Chen Y, Mitchell JW, and Wang PC. A 31P NMR Study of TOPO Release from TOPO-coated Quantum Dots. (To be submitted to the Journal of Colloid and Interface Science)
   4.2. Korotcov AV, Ye YP, Chen Y, Zhang FY, Huang S, Lin S, Sridhar R, Achilefu S, Wang PC. Glucosamine Linked Near-infrared Fluorescent Probes for Imaging of Solid Tumor Xenografts. Mol. Imaging and Biology. 14(4):443-51, 2012. PMID21971932, PMC3288187.
   4.3. Wu CS, Huang S, Korotcov AV, Lin S, Andreev OA, Reshetnyak YK, Wang PC. pH Sensitive Nanoprobe for Tumor Targeting. Howard University Health Sciences Research Day 2012, Howard University, Washington, DC, April 13 2012, p. 21
   4.4. Zhang FY, Shan L, Liu YY, NevilleD, Woo JH, Chen Y, Korotcov AV, Lin S, Huang S, Sridhar R, Liang W, Wang PC. An Anti-PSMA Bivalent Immunotoxin Exhibits Specificity and Efficacy for Prostate Cancer Imaging and Therapy. (Submitted to Advanced Health Materials, 09/2012)
   4.5. Meng H, Xing GM, Blanco E, Song Y, Zhao L, Sun BY, Li XD, Wang PC, Korotcov A, Li W, Liang XJ, Chen CY, Yuan H, Zhao F, Chen Z, Sun T, Chai ZF, Farrari M, Zhao YL. Gadolinium Metallofullerenol Nanoparticle Inhibits Cancer Metastasis through Matrix Metalloproteinase Inhibition: Imprisoning Instead of Poisoning Cancer Cells. Nanomedicine: Nanotechnology, Biology and Medicine 8(2):136-146, 2012. PMID 21930111.
5. Abstracts

Appendix 1   Research Projects Supported by the Nanomedicine Core

1. Physicochemical Characteristics of Nanoparticles as MR Contrast Agent Delivery System with the Dynamic Contrast Enhancement Pattern for Clinical Applications (Wang PC, Korotcov A/ Radiology; Sridhar R/ Radiation Oncology; Bhujwalla Z/Radiology/Johns Hopkins).
2. Develop multifunctional nanoparticles for breast cancer diagnosis and treatment – using anti-VEGFR-2 immunotoxin as dual purpose ligand and chemotherapeutics as encapsulated payload (Shan L, Zang FY/Radiology; Liu YY, Naville D/ NIH and Angimmune LLC).
3. Monitoring Thiol Mediated Degradation of TOPO-Quantum Dots by 31P NMR Spectroscopy (Wang TX/Chemical Engineering, Korotcov A/Radiology; Sridhar R/Radiation Oncology/Howard University).
4. Tumor Optical Imaging of Glucosamine Linked Fluorescent Probes in Mice (Korotcov A, Ye Y, Wang PC/Radiology; Achilefu S/Radiology/Washington University at St. Louis)
5. Integrin αvβ3-targeted Prostate Cancer Imaging by Near-Infrared Fluorescent Mono- and Divalent RGD Compounds (Ye Y, Korotcov A/ Radiology/ Howard University).
6. Evaluation of Novel Disulfide-containing Cyclic RGD Compounds for Prostate Cancer Optical Imaging (Yunpeng Ye, Wang PC/Radiology/Howard University)
7. Protein Nanospheres: Synergistic Nanoplatform-Based Probes for Multimodality Imaging (McDonald MA/ Material Measurement Laboratory/NIST, Wang PC/Radiology/Howard, Siegel EL/Radiology/University of Maryland)
8. Circumvention of Cisplatin-Resistance in Prostate Cancer (Canada R/Physiology and Biophysics)
9. Immunoliposome Based Nanotherapy of Brain Tumor (Chang E /Oncology/ Georgetown U)
10. Design of Multifunctional Polymeric Nanoparticles for Breast Cancer Diagnosis and Treatment (Akala E/Pharmacy)
11. Tumor-Targeted pH-Sensitive Nanoparticulate MRI Agent with Enhanced Contrast and Reduced Side Effect (Wang TX/Chemical Engineering, Korotcov A/Radiology)

Appendix 2   Personnel Received Pay in This Research Effort

- Paul C. Wang, Ph.D (PI)
- Alexandru V. Korotcov, PhD.
- Yunpeng Ye, Ph.D.
- Rajgopalan Sridhar, Ph.D.
- Yue Chen, B.S.
- Sophia Huang, B.S.

Appendix 3   Students Participated in Nanomedicine Core Supported Research Projects

<u>Postdoctoral Fellows:</u>
- Chung-Shieh Wu (Chemistry/Radiology)
- Bin Zhi (Anatomy)
- Hong Wang (Anatomy)
- Progya Saha (Anatomy)
- Yukti Sharma (Physiology & Biophysics)
- Mingfe Wu (Anatomy)
- David Wu (Cancer Center)

<u>Predoctoral M.D./Ph.D./Dental Students:</u>
- Belinda Hauser (Genetics)
- Oluseyi Awodele (Medicine)
- Chunxiao Cai (Dental School)
- Yuan Zhao (Dental School)

<u>Undergraduate students:</u>
- Akeem Moore (Biology)
- Sophia Huang (Pre-med)
- Kacey Davis (Anatomy)
- Sulman Rahmat (Anatomy)
- Kristopher Beckwith (Biology)
- Subhas Mukherjee (Biology)

Appendix 4   Reprints of Publication

A ^{31}P NMR Study of TOPO Cleavage from TOPO-Quantum Dots

Tongxin Wang[1,2,3,*,†], Alexandru V. Korotcov[1,†], Rajagopalan Sridhar[4], Yue Chen[1], James W. Mitchell[2], and Paul C. Wang[1,*]

Authors affiliations and addresses:

[1]   Molecular Imaging Laboratory, Department of Radiology, Howard University Washington, DC 20060, USA

[2]   CREST Center for Nanomaterials, College of Engineering, Howard University Washington, DC 20059, USA

[3]   College of Dentistry, Howard University, Washington, DC 20059, USA

[4]   Department of Radiation Oncology, Howard University Washington, DC 20060, USA

[†] These authors contributed equally to this work

* These are corresponding authors:

Paul C. Wang, Ph.D., Professor, Tel: (202)865-3711, Fax: (202)865-3722,
e-mail: pwang@howard.edu
or
Tongxin Wang, Ph.D., Assistant Professor, Tel: (202) 806-4791,
e-mail: twang@howard.edu

Shortened title:

Study of TOPO-QD degradation by 31P NMR

Manuscript category:

ARTICLE

Abstract: The commonly used trioctylphosphine oxide (TOPO) coated semiconductor quantum dot nanocrystals (QDs) for biomedical imaging, may not be sufficiently stable under physiological conditions because of the potential exchange reaction between QDs and reactive nucleophilic biomolecules. Mercaptoethanol was selected as the model to study the potential interaction between TOPO-QDs and thiol group, which is biologically abundant in proteins. ^{31}P NMR spectroscopy was used to study the interaction of TOPO-QDs with different concentrations of mercaptoethanol and monitor the gradual detachment of TOPO from the surface of TOPO-QDs. The ^{31}P NMR spectra of TOPO-QDs (56 mg/mL) do not display any obvious peak related to phosphorus containing species when the concentration of thiol was less than 10 mM. The signal intensities of ^{31}P NMR related to free TOPO increased as the concentration of mercaptoethanol was increased, suggesting cleavage of TOPO from the surface of QDs by nucleophilic action of thiol. This cleavage was further confirmed by the dependence of chemical shift on the concentration of mercaptoethanol. This study demonstrates that TOPO-QDs are relatively unstable and that TOPO can be cleaved from QDs in the presence of a nucleophilic agent such as thiol, which is widely distributed in tissue and physiological fluids. This research provides preliminary information about the potential risk presented by the degradation of TOPO-QDs in physiological systems.

Introduction

Semiconductor quantum dot nanocrystals (QDs) are useful as optical probes for biomedical imaging [1-15]. The potential for release of toxic Cd^{2+} ions from Cd contaning QDs may preclude safe use of this type of QDs in the clinical setting [16-19]. Recent studies suggest that QDs could be cytotoxic [12, 13, 20-24]. The mechanisms of toxicity may be due to the release of toxic Cd^{2+} from oxidation or photolysis [13, 22]. The interaction of QDs with biomolecules or Cd^{2+} binding with intracellular proteins (e.g. through mercapto group) can lead to loss of biological function [25, 26].

Surface coating of QDs plays a key role in determining the potential for release of Cd^{2+} ions and interaction with biomolecules [7, 13, 19, 21, 27]. Water-soluble QDs used in recent biomedical research are usually prepared from TOPO and TOPO dissolved in an organic solvent, and transferred into aqueous phase through 1) thiolate ligands [2, 27]; 2) amphiphilic polymers [6, 7, 12] or 3) cross-linked silica [28, 29]. Recent studies indicate that QDs with amphilphilic polymer coating are biologically inert in both living cells and living animals [6-8, 12]. However, their actual stability under physiological conditions as well as their interaction with biological molecules or specific bio-rich functional groups require further investigation.

In this research, ^{31}P NMR spectroscopy was used to study the interaction between TOPO-QDs and biologically abundant mercapto (-SH) group. Mercaptoethanol was selected as the model of the biologically encountered nucleophilic functional group to study the interaction with QDs. The ^{31}P NMR signal due to TOPO in solution is a sharp peak. Intact TOPO coated QDs contain TOPO in a rigid form with no rotational freedom, such that the ^{31}P NMR signal is almost undetectable. However, as TOPO detaches from QDs, the molecule gains freedom of motion and the ^{31}P NMR signal starts to sharpen gradually. Broad signal indicates rigidly bound TOPO and sharp signal indicates free unbound TOPO in solution. Thus, this study demonstrates that TOPO-QDs are relatively unstable and that TOPO can be cleaved from QDs in the presence of a nucleophilic agent such as thiol, which is widely distributed in tissue and physiological fluids.

Materials and Methods

Materials: All reagents, including 2-mercaptoethanol (Sigma), cadmium oxide (99.998%, Alfa Aesar), stearic acid (99%, Alfa Aesar), tri-*n*-octylphosphine oxide (TOPO, ReagentPlus, 99%, Sigma-Aldrich), 1-hexadecylamine (90%, Alfa Aesar), tri-*n*-octylphosphine (TOP, tech., 90%, Aldrich), dimethylzinc (1.2 mol/L solution in toluene, Acros), hexamethyldisilathiane (Fluka) and chloroform-d (CDCl$_3$, 99.8 atom % D, contains 1% (v/v) TMS, Aldrich) were used without further purification.

Synthesis of TOPO stabilized quantum dot nanocrystals (TOPO-QDs): TOPO-QDs in this paper represent CdSe-ZnS core-shell nanocrystals stabilized with TOPO. TOPO-QDs were synthesized according to the method described in the literature [7]. Cadmium oxide (256 mg, 2 mmol), stearic acid (5 g) and TOPO (20 g) were mixed and flushed with argon flow. Then, the mixture was heated to 250 °C until a clear solution resulted. Twenty grams of hexadecylamine were added to the clear solution after it had cooled down to room temperature. The mixture was heated back to 250 °C for 10 min and then raised to 300 °C. Selenium (158 mg, 2 mmol) dissolved in 20 mL of trioctyl phosphine was quickly injected into the hot solution. The mixture immediately changed color to orange red, indicating formation of quantum dots. The reaction mixture was refluxed for 60 min, and then cooled down to 220 °C. Dimethylzinc (0.83 mL of 1.2 mol/L in toluene, 1 mmol) and hexamethyldisilathiane (178 mg, 1 mmol) in 25 mL of trioctyl phosphine were slowly added drop wise to the reaction mixture at 220 °C. The mixture was refluxed for 30 min and then cooled to room temperature. The TOPO/QDs were extracted with toluene and re-precipitated with methanol for 10 times to thoroughly remove the unbound TOPO. After centrifugation, the product was re-dispersed in 5×750 μL CDCl$_3$ (56 mg QDs each) for ^{31}P NMR, transmission electron microscope (TEM), dynamic light scattering (DLS), UV-vis and fluorescent spectra.

Measurements: Transmission electron micrographs (TEM) were taken using a JEOL 3010 HREM operating at 100 kV. Sample for TEM was prepared by depositing a drop of suspension of QDs onto carbon-coated Cu grids followed by drying at room temperature. Dynamic light scattering (DLS) was conducted on a nano-ZS zeta-sizer (Malvern). UV-Vis spectra were recorded on a Cary 5000 spectrometer using a 1.0 cm quartz cuvette. Emission spectra were measured on a Hitachi F-7000 fluorescent spectrometer using a 1.0 cm quartz cuvette.

^{31}P NMR spectra were recorded in CDCl$_3$ on a 400 MHz Bruker instrument at 4 °C. Chemical shift values, δ (ppm), were referenced to H$_3$PO$_4$ (0 ppm) as an external standard. The ^{31}P NMR scanning parameters were set up as sample temperature 4 ºC, SW = 90 ppm, repetition time 0.2 sec, number of scans 3332, thus the total scanning time for each measurement was around 11 minutes. In a typical surface ligand displacement experiment, 56 mg of purified QDs nanoparticles was dissolved in 750 µL of CDCl$_3$. At first, the spectrum was taken on the QDs before addition of thiol. Then, in order to monitor the concentration dependent ligand exchange reaction, aliquest of thiol was added and the spectra were taken immediately after addition of thiol followed by shaking for 30 seconds.

Results and Discussion

The QDs used for ^{31}P NMR study were prepared using cadmium oxide and selenium as reactants and dimethyl zinc and hexamethyldisilathiane as ZnS coating precursors. Fractionation by centrifugation was followed by size selective precipitation from toluene by addition of methanol. TEM shows that the QDs possess a diameter of 6.2 nm. The optical properties of QDs were confirmed by fluorescent emission and UV-vis absorption spectra. UV-vis spectrum shows the broad absorption around 500 nm. Fluorescent spectrum shows an emission peak at 617 nm. These QDs are soluble in an organic solvent such as toluene or chloroform because TOPO is a QD coating layer.

Mercaptoethanol was selected to mimic nucleophilicity of biologically abundant protein and non protein thiols. In order to monitor the ligand exchange reaction between QDs and thiol, mercaptoethanol (1 mM - 90 mM) was added to the suspension of QDs (56 mg/mL). Prior to

addition of mercaptoethanol, ^{31}P NMR signal was not observed because the TOPO was firmly bound to the QDs. However, ^{31}P NMR signal was seen to develop when QDs were incubated with graded concentrations of mercaptoethanol. The signal intensity increased as the concentration of thiol was increased. Literature reports indicated that the NMR spectra of CdSe nanoparticles stabilized with TOPO displayed broad signals, which were attributed to the surface-bound phosphorus ligands in non homogeneous nuclear environments [30-33]. At least three types of surface-bound phosphorus ligands were observed at the positions prominently centered at 30, 15 and −5 ppm, which were assigned to TOPO, TOPSe, and TOP, respectively.

Figure 1 shows ^{31}P NMR spectra of QDs in the absence and presence of mercaptoetahnol (thiol) as well as the spectrum of pure TOPO in CDCl$_3$. In the absence of thiol, no obvious peak was observed from QDs. This observation is unlike the results from an earlier report, in which a group of strong broad peaks were observed [25, 26]. In our case, only the broad peak around 28 ppm can be observed but the signal is rather weak. The possible reasons for the weak signal of the broad peaks in this experiment could be: 1) the concentration of our QDs (56 mg/mL) is lower than that used in the literature (130 mg/mL); and 2) the TOPO-QDs used in this study were washed thoroughly to remove unbound TOPO. These results indicate that no free phosphorus containing species could be detected before addition of thiol and most of the TOPO and/or TOPSe in our QDs are strongly bound to the surface of QDs.

Similar to the spectrum of QDs in the absence of thiol, addition of low amounts of thiol did not yield evidence of release of phosphorus compound from QDs. The spectra did not display any obvious peak related to phosphorus containing species when the concentration of thiol was low (less than 10 mM). This observation indicates that there were almost no free phosphorus containing species in solution or their concentration was too low to be detected at the instrument settings used in this study.

With increasing concentration of thiol, obvious sharp peaks related to free phosphorus containing species were observed. When the concentration of thiol was 15 mmol/L, a sharp peak around 45.5 ppm could be detected using the same experimental condition as before (Figure 1). This result indicated that a low amount of phosphorus containing species was cleaved from QDs by the action of thiol.

When the thiol concentration was increased from 15 mmol/L to 24 mmol/L, the sharp peak of cleaved phosphorus containing species became more prominent with increased intensity (Figure 1). This is in agreement with the hypothesis that more phosphorus containing species were detached from the surface of QD by incubation with higher concentration of thiol.

Based on the phosphorus containing species used in this experiment, the cleaved species could be TOPO, TOPSe or even TOP. Since there is scant information or experimental data on the chemical shifts of phosphorus-based ligands bound to CdSe surfaces, an exact assignment of the detached or cleaved species is still unclear. Kopping and Patten have attempted to assign the ^{31}P NMR chemical shifts of the phosphorus containing species involved in the TOPO-QDs system, including the impurities [31]. A variety of peaks were assigned as TOPO (52 ppm), di-n-octylphosphinic acid (44 ppm), octylphosphonic acid (25 ppm) and P,P'-(di-n-octyl) dihydrogenpyrophosphonic acid (18 ppm). Different environment leads to different chemical shift of TOPO (49.5 ppm [33] or 50 ppm [30]). Our experiments showed that the chemical shift of free TOPO is 48.4 ppm. Therefore, the peak at 45.5 ppm was tentatively assigned to the TOPO, which might be partially detached from the surface of QDs.

Signal strength should provide a relatively quantitative result with respect to the amount of the cleaved TOPO from QDs by thiol, as all of the measurements for comparison were conducted under the same instrumental setting. Figure 2A shows the signal strength of the cleaved TOPO as a function of thiol concentration in the suspension of QDs. In order to quantitatively estimate the

cleaved TOPO from QDs, the signal strength was normalized to the external H_3PO_4 reference, which was the same for all the measurements.

When the thiol concentration was lower than 8.8 mmol/L, it was difficult to detect the cleaved TOPO in suspension. However, the signal strength of 1.3 upon addition of 8.8 mmol/L thiol confirms that TOPO was cleaved from the surface of QDs. The signal strength increased sharply from 1.3 to 10.3, when the concentration of thiol changed from 8.8 mmol/L to 12.1 mmol/L. The control experiment with pure TOPO showed that the signal strength of ^{31}P NMR increased linearly with the concentration of TOPO in the range of 1 mM to 90 mM (figure not shown). Therefore, the sharp increase of the signal strength with increasing thiol concentration in our experiments confirms that more TOPO was released from QDs upon addition of more thiol. However, if the concentration of thiol was above 12.1 mmol/L, the signal strength of cleaved TOPO did not significantly increase further upon addition of more thiol. Even though the concentration of thiol was up to about 8 fold higher (from 12.1 mmol/L to 90.5 mmol/L), the signal strength increased only 50% (the value of signal strength changed from 12.1 to 18). This result indicates that TOPO was continuously cleaved from QD surface. Although the mechanism of cleavage is not understood, a two different kinetics of cleavage were observed with a faster cleavage rate at lower thiol concentration range.

Figure 2B is the curve of the chemical shift of TOPO cleaved from the surface of QDs as well as the pure TOPO in $CDCl_3$ with gradual increase of thiol concentration. The important point is that with the gradual increase of the signal intensity of cleaved TOPO was accompanied by a changed chemical shift of the signal with the concentration of thiol. It is shown that the chemical shift gradually changes from high field (around 45 ppm) to low field (around 49.5 ppm). Moreover, the curve shows two distinct slopes, indicating different interaction between QDs and thiol at lower or higher concentration. In the range of lower concentration of thiol (< 40 mmol/L, indicated by point A in Figure 2B), the curve shows a greater slope, indicating more significant effect of thiol on chemical shift change. When the thiol concentration was around 39 mmol/L, the chemical shift (48.5 ppm) of

TOPO cleaved from QDs was equal to that of free TOPO in CDCl$_3$ (48.4 ppm). This chemical shift confirms that the cleaved TOPO is free and has no detectable interaction with QDs. However, when the concentration of thiol was greater than 39 mmol/L, the curve has a shallower slope. This fact implies that the chemical shift of TOPO changed slowly upon addition of the same amount of thiol. Control experiment of pure TOPO also showed chemical shift change upon addition of thiol (Figure 2B). Moreover, the slope of TOPO cleaved from QDs above point A is close to that for the interaction mercaptoethanol with pure TOPO, thus confirming that all of the cleaved TOPO is 'free' from QDs.

In addition to the sharp peak related to the cleaved TOPO from QDs, the broad peak centered at 28 ppm becomes more significant, although it was still very weak (Figure 1). This implies that the species related to 28 ppm is slightly influenced by addition of thiol, which might interact with this species and makes it less firmly bound and detach from the strongly-binding surface of QDs.

The increase of signal strength and the change of chemical shift discussed above confirm the interaction between TOPO stabilized QDs and thiol (mercaptoethanol). Before addition of thiol, there is no sharp peak related to free phosphorus containing species. In the literature, the only peaks observed from suspensions of QDs are the broad peaks, which were attributed to the species strongly binding to QDs surface [30-33]. When thiol was added to QDs, TOPO on the surfaces of QDs were replaced by thiol. More added thiol led to more cleaved TOPO, which was detected by ^{31}P NMR. Increase of the signal strength indicated that more TOPO was cleaved from QDs. Eventually, when the thiol concentration was sufficiently high, e.g. 40 mmol/L, no more TOPO could be cleaved, and the signal strength remained relatively constant.

Moreover, change of chemical shift provides additional evidence of the interaction between thiol and TOPO-QDs. Our results indicate that the chemical shift of the cleaved TOPO changes from around 45 to 49.5 ppm. The chemical shift change can be understood on the basis of the shielding/de-shielding effect of QDs to TOPO. The ^{31}P NMR signal for free TOPO in CDCl$_3$ was

found at 48.4 ppm. When the TOPO is bound to QDs, the chemical shift should be located in high field due to the shielding effect of QDs. After thiol was added, TOPO was cleaved from the surface of QDs, leading to less shielding effect. Therefore addition of more thiol results in cleavage of more TOPO. Another possibility is that the nucleophilic agent, thiol might attack to the P=O double bond in TOPO through a nucleophilic addition reaction to form a complex between TOPO and mercaptoethanol, or protonation of the oxygen within TOPO (Figure 3). The interaction between thiol and TOPO will additionally decrease the electron density of ^{31}P atom, which is further confirmed by the increase of chemical shift of free TOPO upon addition of thiol (Figure 2B). Thus, the chemical shift will change from 45 ppm to the position of pure TOPO (48.4 ppm).

Additional thiol caused a change in the chemical shift of TOPO (49.6 ppm at 90 mmol/L of thiol) beyond that of pure TOPO (48.4 ppm). The possible reason could be the electron-withdrawing effect of thiol or even the nucleophilic addition of thiol to the P=O double bond. Due to the charge distribution of thiol and P=O bond, thiol has the tendency for nucleophilic attack on the P=O bond. This can decrease electron density around phosphorus atom, resulting in a change of chemical shift of TOPO to the low field. At low concentration thiol, TOPO interacts with both thiol and QDs. Due to the electron-withdrawing effect of thiol and the shielding effect of QDs, the chemical shift of TOPO changed dramatically upon addition of thiol, indicated by a greater slope (Figure 2B before point A). However, at high thiol concentration, because TOPO is cleaved, the chemical shift is only influenced by the thiol. Thus the observed slope is shallower than that from lower thiol concentration (Point A of Figure 2B) and become similar to that seen for interaction of thiol with pure TOPO.

3. Conclusion

^{31}P NMR was used to detect the ligand exchange reaction between thiol and TOPO stabilized QDs. The results indicate that TOPO-QDs are relatively unstable and TOPO can be cleaved from QDs upon addition of nucleophilic agent, e.g. -SH. Signal strength of ^{31}P NMR spectra indicates that

the amount of TOPO cleaved from the surface of QDs is dependent on the amount of added -SH. Moreover, the cleavage of TOPO from QDs by thiol and the nature of interaction with thiols were confirmed by the dependence of chemical shift of cleaved TOPO on the concentration of thiol. This research provides preliminary information about the potential risk presented by the degradation of TOPO-QDs in physiological systems rich in thiols. TOPO-QDs may not be biocompatible for biomedical imaging. In view of their unique fluorescent properties, it will be necessary to improve QDs coating technology for achieving better biocompatibility. Further, ^{31}P NMR spectroscopy may be employed to monitor the cleavage of TOPO from TOPO-QDs and assess their stability *in vivo* in living system.

References

[1]   M.J. Bruchez, M. Moronne, P. Gin, S. Weiss, A.P. Alivisatos, Science 281 (1998) 2013.

[2]   W.C. Chan, S. Nie, Science 281 (1998) 2016.

[3]   B.O. Dabbousi, J. Rodriguez-Viejo, F.V. Mikulec, J.R. Heine, H. Mattoussi, R. Ober, K.F. Jensen, M.G. Bawendi, J. Phys. Chem. B 101 (1997) 9463.

[4]   J.K. Jaiswal, H. Mattoussi, J.M. Mauro, S.M. Simon, Nat. Biotechnol. 21 (2003) 47.

[5]   P. Alivisatos, Nat. Biotechnol. 22 (2004) 47.

[6]   X. Wu, H. Liu, J. Liu, K.N. Haley, J.A. Treadway, J.P. Larson, N. Ge, F. Peale, M.P. Bruchez, Nat. Biotechnol. 21 (2003) 41.

[7]   X. Gao, Y. Cui, R.M. Levenson, L.W.K. Chung, S. Nie, Nat. Biotechnol. 22 (2004) 969.

[8]   D.R. Larson, W.R. Zipfel, R.M. Williams, S.W. Clark, M.P. Bruchez, F.W. Wise, W.W. Webb, Science 300 (2003) 1434.

[9]   Z. Liu, W. Cai, L. He, N. Nakayama, K. Chen, X. Sun, X. Chen, H. Dai, Nat. Nanotechnol. 2 (2007) 47.

[10]   S. Kim, Y.T. Lim, E.G. Soltesz, A.M. De Grand, J. Lee, A. Nakayama, J.A. Parker, T. Mihaljevic, R.G. Laurence, D.M. Dor, L.H. Cohn, M.G. Bawendi, J.V. Frangioni, Nat. Biotechnol. 22 (2004) 93.

[11]   M.E. Åkerman, W.C.W. Chan, P. Laakkonen, S.N. Bhatia, E. Ruoslahti, Proc. Natl. Acad. Sci. U. S. A. 99 (2002) 12617.

[12]   B. Dubertret, P. Skourides, D.J. Norris, V. Noireaux, A.H. Brivanlou, A. Libchaber, Science 298 (2002) 1759.

[13]   A.M. Derfus, W.C.W. Chan, S.N. Bhatia, Nano Lett. 4 (2003) 11.

[14]   Y. Wang, L. Chen, Nanomedicine 7 (2011) 385.

[15]   P. Zrazhevskiy, M. Sena, X. Gao, Chem. Soc. Rev. 39 (2010) 4326.

[16]   M.C. Henson, P.J. Chedrese, Exp. Biol. Med. 229 (2004) 383.

[17]   M. Kondoh, S. Araragi, K. Sato, M. Higashimoto, M. Takiguchi, M. Sato, Toxicology 170 (2002) 111.

[18]   S. Satarug, M.R. Moore, Environ. Health Perspect. 112 (2004) 1099.

[19]   A. Hoshino, S. Hanada, K. Yamamoto, Arch. Toxicol. 85 (2011) 707.

[20]   A. Shiohara, A. Hoshino, K. Hanaki, K. Suzuki, K. Yamamoto, Microbiol. Immunol. 48 (2004) 669.

[21]   A. Hoshino, K. Fujioka, T. Oku, M. Suga, Y.F. Sasaki, T. Ohta, M. Yasuhara, K. Suzuki, K. Yamamoto, Nano Lett. 4 (2004) 2163.

[22]   J. Lovrić, H.S. Bazzi, Y. Cuie, G.R.A. Fortin, F.M. Winnik, D. Maysinger, J. Mol. Med. 83 (2005) 377.

[23]   N. Chen, Y. He, Y. Su, X. Li, Q. Huang, H. Wang, X. Zhang, R. Tai, C. Fan, Biomaterials 33 (2012) 1238.

[24]   W. Liu, S. Zhang, L. Wang, C. Qu, C. Zhang, L. Hong, L. Yuan, Z. Huang, Z. Wang, S. Liu, G. Jiang, PLoS ONE 6 (2011) e24406.

[25]   C. Kirchner, T. Liedl, S. Kudera, T. Pellegrino, A. Muñoz Javier, H.E. Gaub, S. Stölzle, N. Fertig, W.J. Parak, Nano Lett. 5 (2004) 331.

[26]   A. Hoshino, K.-i. Hanaki, K. Suzuki, K. Yamamoto, Biochem. Biophys. Res. Commun. 314 (2004) 46.

[27]   J. Aldana, Y.A. Wang, X. Peng, J. Am. Chem. Soc. 123 (2001) 8844.

[28]   A.L. Rogach, D. Nagesha, J.W. Ostrander, M. Giersig, N.A. Kotov, Chem. Mater. 12 (2000) 2676.

[29]   D. Gerion, F. Pinaud, S.C. Williams, W.J. Parak, D. Zanchet, S. Weiss, A.P. Alivisatos, J. Phys. Chem. B 105 (2001) 8861.

[30]   M. Kuno, J.K. Lee, B.O. Dabbousi, F.V. Mikulec, M.G. Bawendi, J. Chem. Phys. 106 (1997) 9869.

[31]   J.T. Kopping, T.E. Patten, J. Am. Chem. Soc. 130 (2008) 5689.

[32]   W.H. Binder, R. Sachsenhofer, C.J. Straif, R. Zirbs, J. Mater. Chem. 17 (2007) 2125.

[33]   N. Al-Salim, A.G. Young, R.D. Tilley, A.J. McQuillan, J. Xia, Chem. Mater. 19 (2007) 5185.
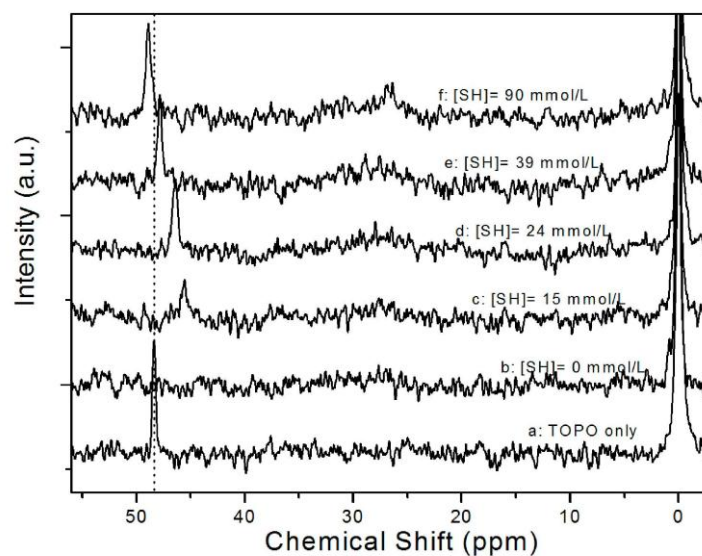
Figure 1. ^{31}P NMR spectra of QDs in the absence and presence of different concentration of thiol along with spectrum of pure TOPO in CDCl$_3$.
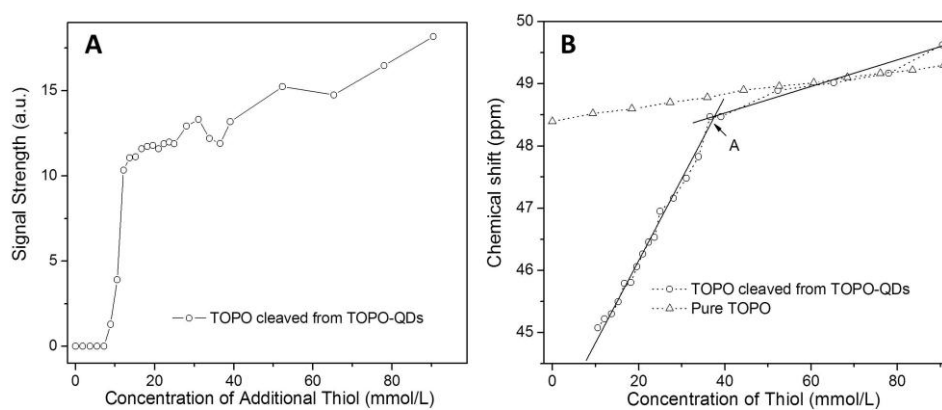
Figure 2. A) Signal strength of ^{31}P NMR of the cleaved TOPO from the surface of QDs with different concentrations of SH at 4 $^{\circ}$C. Signals were normalized to an external H$_3$PO$_4$ reference. **B)** Change of chemical shift of cleaved TOPO with addition of SH at 4 $^{\circ}$C.
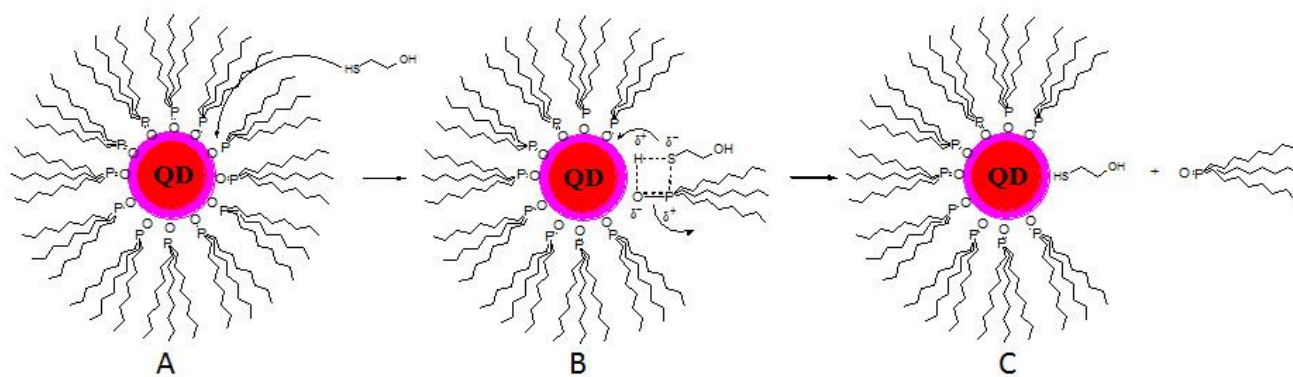
Figure 3. Proposed mechanism of nucleophilic attack of thiol to TOPO-QD which leads to cleavage of TOPO from the surface of QD. A) origianl TOPO-QD attacked by mercaptoethanol (ME); B) possible TOPO-ME complex; C) free TOPO cleaved from TOPO-QD and mercaptoethanol partially coated QD.

MOLECULAR IMAGING AND BIOLOGY

RESEARCH ARTICLE

Glucosamine-Linked Near-Infrared Fluorescent Probes for Imaging of Solid Tumor Xenografts

Alexandru V. Korotcov,[1] Yunpeng Ye,[1,2] Yue Chen,[1] Fayun Zhang,[1] Sophia Huang,[1] Stephen Lin,[1] Rajagopalan Sridhar,[3] Samuel Achilefu,[2] Paul C. Wang[1]

[1]*Molecular Imaging Laboratory, Department of Radiology, Howard University, Washington, DC, USA*
[2]*Optical Radiology Laboratory, Department of Radiology, Washington University School of Medicine, St. Louis, MO, USA*
[3]*Department of Radiation Oncology, Howard University, Washington, DC, USA*

Abstract

Purpose: Near-infrared fluorescence (NIRF) imaging is an attractive technique for studying diseases at the molecular level *in vivo*. Glucose transporters are often used as targets for *in vivo* imaging of tumors. The efficiency of a tumor-seeking fluorescent probe can be enhanced by attaching one or more glucosamine (GlcN) moieties. This study was designed to evaluate the use of previously developed GlcN-linked NIRF probes for *in vitro* and *in vivo* optical imaging of cancer.

Procedures: Cellular uptake of the probes (1 μM) was investigated in monolayer cultures of luciferase-expressing PC3 (PC3-luc) cells. The prostate tumors were established as subcutaneous xenografts using PC3-luc cells in nude mice. The biodistributions and tumor-targeting specificities of cypate (cyp), cypate-D-(+)-glucosamine (cyp-GlcN), and D-(+)-gluosamine-cypate-D-(+)-gluosamine (cyp-2GlcN) were studied. The tumor, muscle, and major organs were collected for *ex vivo* optical imaging.

Results: The tumor cell uptake of the probe containing two glucosamine residues, cyp-2GlcN, was significantly higher than the uptake of both the probe with one glucosamine residue, cyp-GlcN, and the probe without glucosamine, cyp only. Similarly, in *in vivo* experiments, cyp-2GlcN demonstrated higher maximum fluorescence intensity and longer residence lifetime in tumors than cyp-GlcN or cyp. The *ex vivo* biodistribution analysis revealed that tumor uptake of cyp-2GlcN and cyp-GlcN was four- and twofold higher than that of cyp at 24 h post-injection, respectively.

Conclusion: Both cyp-GlcN and cyp-2GlcN NIRF probes exhibited good tumor-targeting properties in prostate cancer cell cultures and live mice. The cyp-2GlcN probe showed the highest uptake with good retention characteristics *in vivo*. The uptake of cyp-2GlcN and cyp-GlcN is likely mediated by glucosamine-recognizing transporters. The uptake mechanism is being explored further for developing cypate-glucosamine-based probes for *in vivo* imaging.

Key words: Optical imaging, Near-infrared fluorescence, Tumor, Prostate cancer, Glucosamine, Cypate

Introduction

Near-infrared fluorescence (NIRF) imaging is an inexpensive technique for studying diseases at the molec-ular level, detecting small tumors, monitoring targeted drug delivery, and evaluating therapeutic response [1–3]. The low absorption and increased photon penetration depth in the near-infrared (NIR) tissue transparency window (650–900 nm) are some of the major benefits of using NIR light for *in vivo* imaging [4–6]. NIRF rapid imaging technique provides high-throughput imaging with relatively high

sensitivity. Moreover, this technique poses no risks associated with techniques involving ionizing radiation. Image contrast and diagnostic accuracy can be improved significantly by using tumor-targeted NIRF imaging probes, which would serve as an active agent to enhance the optical signal from disease-specific molecular markers. Targeted probes usually link a signaling unit (organic or inorganic dye, quantum dots, *etc*.) to a targeting arm provided by a specific ligand, peptide, antibody, sugar, or other small molecule [7–9]. A targeted diagnostic approach with a high signal to noise ratio can provide increased sensitivity and additional tumor specificity with potential extension to a targeted theragnostics (or theranostics), which is a treatment strategy that combines therapeutics with diagnostics [10].

Malignant cells have altered metabolism and increased requirements for glucose and glutamine. Enhanced tumor uptake of glucose is facilitated by the overexpression of glucose transporter proteins (GLUTs), which is widely observed in tumor tissue [11–13]. The most commonly used positron-emitting radiopharmaceutical, 2-deoxy-2-[^{18}F]fluoro-D-glucose (FDG), is a glucose analog used extensively in cancer detection and therapeutic monitoring utilizing positron emission tomography (PET) [14]. Increased uptake of FDG and increased activity of hexokinase in tumors result in the accumulation of FDG in cancer cells independent of glucose uptake [15, 16].

GLUT1 was the first facilitative sugar transporter discovered; it primarily transports glucose, although it can also recognize and transport galactose, mannose, and glucosamine (GlcN). GLUT1 is responsible for basal glucose uptake required to maintain glycolysis and respiration in cells. GLUT2 is a glucose transporter with high affinity for glucosamine. GLUT4 is an insulin-regulated glucose transporter able to move glucosamine and dehydroascorbic acid [13]. GLUT1 and GLUT4 are transcriptionally repressed by p53, a tumor suppressor protein that is important in cell cycle control and in promoting apoptosis [17]. Since PC3 human prostate cancer cells do not express p53 protein [18], repression of GLUT1 and GLUT4 is not expected. The common feature of these GLUTs is their ability to transport glucosamine. Whereas GLUT1 and GLUT4 have similar apparent affinities for glucose and glucosamine, GLUT2 has a ~20-fold higher affinity for GlcN than for glucose, but is mostly expressed in the liver, basolateral surface of kidney absorptive cells, and in pancreatic β cells [13, 19]. Elevated GLUT1 expression has been reported in many cancers including PC3 cell line [20, 21]. Therefore, increased accumulation of glucosamine-based probes can be expected in tumors which overexpress GLUT1. It is well known that FDG-PET has high sensitivity and demonstrated clinical applicability for tumor detection and imaging [22]. However, PET imaging has several limitations, such as exposure to ionizing radiation, difficulty of synthesizing compounds labeled with positron-emitting isotopes, short half-life of positron-emitting nuclide, and relatively low spatial resolution. To overcome some limitations of PET, researchers have been developing optical probes for metabolic imaging [23–25]. Cyanine fluorophores are suitable for *in vitro* and *in vivo* imaging because of their high molar extinction coefficient, biocompatibility, desirable NIR spectral properties between 650 and 900 nm, and relatively high fluorescence efficiency. The main advantages of choosing cypate (cyp) for this study were minimal tissue autofluorescence, decreased absorption and decreased scattering in the excitation and emission regions of cyp, all of which contributed to a photon penetration of several centimeters through tissue [4].

The use of GlcN-linked targeted NIRF probes has potential for enhanced tumor specificity and increased sensitivity. The goal of this study was to investigate some previously designed GlcN-linked targeted NIRF probes [25] for optical imaging of human prostate cancer tumor cells and solid tumor xenografts in mice. A preliminary screen suggested the superiority of multivalent probes over monovalent probes for efficient targeted imaging of tumors [25].

In this investigation, the *in vitro* and *in vivo* uptake of intravenously (i.v.) injected cypate (cyp), cypate conjugated to a single GlcN molecule, cypate-D-(+)-gluosamine (cyp-GlcN), and cypate conjugated to two GlcN molecules, D-(+)-gluosamine-cypate-D-(+)-glucosamine (cyp-2GlcN) was monitored in a mouse xenograft model of human prostate cancer. The biodistribution and tumor-targeting specificity of cyp, cyp-GlcN, and cyp-2GlcN in luciferase-expressing PC3 (PC3-luc) tumors were studied. In addition, competitive uptake of the optical probes in the presence of different sugar derivatives was also evaluated. Overall, GlcN-linked probes appear to label tumors *in vivo* with fairly high specificity and long retention times. The cyp-2GlcN probe showed the highest uptake with good retention characteristics *in vivo*. Slow degradation/clearance provides a longer fluorescence-enhanced window, which can be attractive for the future application in areas such as tumor detection, fluorescence-guided surgical procedures, and theranostics. The uptake mechanism is being explored further for developing cypate-glucosamine-based probes for *in vivo* applications.

Materials and Methods

Cell Culture and Animal Model

The human prostate cancer cell line transfected with luciferase gene, PC-3M-luc (Caliper Life Sciences, Inc., Hopkinton, MA), was used to test the efficiency of the probe *in vitro* and *in vivo*. Cells were maintained as exponentially growing monolayer cultures in Dulbecco's modified Eagle's medium/F12 medium supplemented with 10% heat-inactivated fetal bovine serum and 50 µg/ml each of penicillin, streptomycin, and neomycin (Invitrogen Corporation, Carlsbad, CA). Subcutaneous xenograft tumors of PC-3M-luc were induced subcutaneously into the flank of 6–8-week-old athymic nude mice (Harlan, Indianapolis, IN) by injecting 1×10^7 subconfluent cells in 100 µl Dulbecco's phosphate-buffered saline. All studies were performed in

accordance with institutional guidelines for animal use after obtaining approval for the experimental protocols from Howard University IACUC.

Synthesis of Glucosamine-Cypate Probes

Cyp, cyp-GlcN, and cyp-2GlcN were synthesized as previously described by Ye *et al.* [25]. In short, the carboxylate-terminating multivalent near-infrared carbocyanine probes from a dicarboxylic acid precursor dye (cypate) were prepared via its iminodiacetic acid derivatives. Conjugation of the probes with D-(+)-glucosamine afforded dendritic arrays of the carbohydrates on an inner NIR chromophore core (Fig. 1). The cypate labeling efficiencies have been determined previously [25]. Absorption spectra were used to determine probe concentration. The fluorescence of the diluted probes was measured before all experiments. All the multicarboxylate probes and their glucosamine conjugates had similar UV–vis–NIR absorption and fluorescence characteristics. The absorption and emission spectra maxima were centered on 780 and 810 nm, respectively.

In Vitro Cell Fluorescence Study

The fluorescence microscopy was performed using a Zeiss Axio Observer (Carl Zeiss MicroImaging, LLC, Thornwood, NY) fluorescence microscope equipped with 769/832 nm band-pass (40 nm) excitation/emission filters. A Xenogen IVIS Spectrum imaging system (Caliper Life Sciences, Inc., Hopkinton, MA) was used for quantitative analysis of fluorescent probe uptake (excitation/emission=710/820 nm, 30/20 nm band-pass filters). PC-3M-luc cells were plated at 5,000 cells per well in an 8-well chamber slide (for fluorescence microscopy) and 96-well plates (for quantitative optical imaging). After 24 h, competitive uptake of the probes was imaged in the presence of competing substrates for cellular uptake. Briefly described, cells were incubated for 1 h with 1 μM of cyp, cyp-GlcN, or cyp-2GlcN and one of the following competitive substrates: 1 mM D-glucosamine (D-GlcN), 5 mM D-glucosamine, 5 mM L-glucose (L-Glc), 25 mM L-Glc, 5 mM D-glucose (D-Glc), 25 mM D-Glc, 25 mM *N*-acetyl-D-glucosamine (GlcNAc), or medium (control). The cells were washed three times with PBS and fixed for fluorescence microscopy or subjected directly to optical imaging. All experiments were carried out at 37°C. Each experiment was repeated at least three times, and the results were averaged for further analysis. MTT assays were used to normalize fluorescence intensities in 96-well plate experiments. No cytotoxic effects were observed in cells treated with probes for 3 h in order to determine cellular uptake of the probes.

In Vivo and Ex Vivo Optical Imaging

NIR-based fluorescent imaging was performed with a Xenogen IVIS Spectrum imaging system. Imaging and quantification of signals were controlled by the acquisition and analysis software Living Image (Caliper Life Sciences, Inc., Hopkinton, MA). Mice were subjected to imaging when the tumor size reached 6–7 mm in diameter. Mice were placed onto the warmed stage inside the light-tight camera box and anesthetized by continuous exposure to 1.5% isoflurane. Animals were given 100 μl (10 nmol) of the cypate-based NIRF probe for each tail vein injection. The whole animal was imaged dynamically every 10–30 min during the first 6 h, and then twice a day for 20–30 days. Imaging parameters were: excitation/emission=710/820 nm (30 and 20 nm band-pass filters, respectively); field of view=6.6×6.6 cm^2; f/stop=4; bin=8; and exposure time, 5 s. The signal intensity was expressed as the average radiance (photons per second per centimeter squared per steradian). The contralateral leg muscle served as normal control in these experiments. At the end of the *in vivo* imaging experiments, the mouse was sacrificed by cervical dislocation under isoflurane anesthesia. The tumor, muscle, and the major organs were collected for *ex vivo* optical imaging studies. The normalized signal was calculated by comparing the average fluorescence intensities in the tumor and the thigh muscle from the same animal.

Competitive *in vivo* uptake experiments were done in the manner described above with one more additional step(s) before intravenous injection of the probes. First, the mice were given an intraperitoneal injection of D-Glc (2 g/kg), or D-GlcN (0.5 g/kg), or GlcNAc (2 g/kg) in a total volume of 0.1 ml. After 30 min, cyp-2GlcN (10 nmol) was injected via i.v. Mice were imaged continuously for 24 h and sacrificed, and major organs were collected for *ex vivo* imaging of the biodistribution of the fluorescent probe. Mice were divided into six groups (six mice per group) for the 24-h study of probe uptake as well as biodistribution (Cyp, cyp-GlcN, cyp-2GlcN, cyp-2GlcN+D-Glc, cyp-2GlcN+D-GlcN, and cyp-2GlcN+GlcNAc). Three more groups (three mice per group) were used for a 30-day study of probe clearance and biodistribution of the probes, Cyp, cyp-GlcN, and cyp-2GlcN.

Statistical Analysis

All the data are presented as the mean of at least three experiments (three runs for *in vitro* or three to six animals from the same group for *in vivo* studies). The results were evaluated using statistical software OriginPro V.7 (OriginLab Corporation, Northampton, MA, http://www.originlab.com). Student's *t* test (two tailed) was
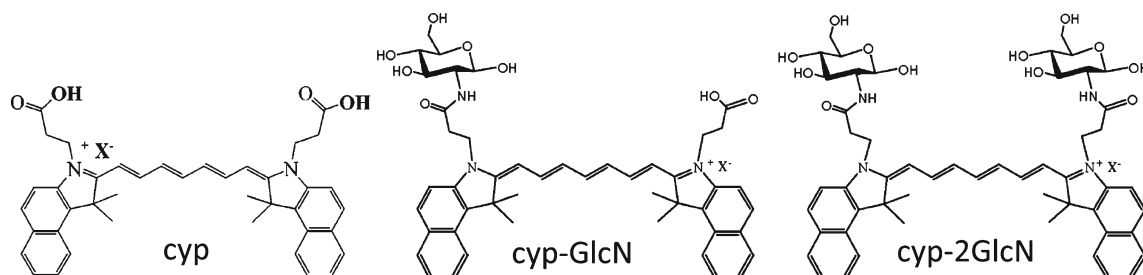

Fig. 1. Structures of near-infrared fluorescence probes: cypate (*cyp*), cypate-D-(+)-gluosamine (*cyp-GlcN*), and D-(+)-gluosamine-cypate-D-(+)-gluosamine (*cyp-2GlcN*).

applied for analysis of statistical differences. A P value <0.05 was considered as a significant difference between any two sets of data.

Results and Discussion

In Vitro Uptake Studies

Cellular uptake of cyp, cyp-GlcN, and cyp-2ClcN was investigated in human prostate cancer cell cultures by fluorescence microscopy. Figure 2 shows fluorescence images of PC3-luc cells after incubation with 1 μM of cyp, or cyp-GlcN, or cyp-2GlcN for 1 h at 37°C. NIRF probes were spread over the entire cytoplasm and exhibited a granular pattern of distribution. The probes did not accumulate in the nucleus or periphery of PC3-luc cells. cyp-GlcN and cyp-2GlcN showed a higher degree of cellular uptake compared to cyp alone, and the highest uptake was observed in cells treated with cyp-2GlcN. The results indicate that the uptake of GlcN-linked probes is an active process involving a transporter that recognizes GlcN, and the cyp-2GlcN probe which has two GlcN residues is taken up more actively than the other two probes examined in this study. Similar granular patterns in micrographs were observed by Li et al. [24] in various cancer cell lines for mono GlcN NIFR

probes. The authors showed that the probes have good tumor-targeting specificity with a tendency to localize in lysosomes.

To explain whether cellular uptake of the probes is related to GLUTs and to quantify the cellular uptake, PC3-luc cells were incubated in 96-well plates with 1 μM of each NIRF probe alone, and in combination with a competing sugar derivative such as D-GlcN (1 and 5 mM), L-Glc (5 and 25 mM), D-Glc (5 and 25 mM), or GlcNAc (25 mM) for 1 h at 37°C. The GlcN-linked probes incubated without sugars showed the ability to accumulate in PC3-luc prostate cancer cells (Fig. 3, control). The uptake of cyp-2GlcN was significantly higher than the uptake of the cyp-GlcN or cyp. The uptake of cyp-GlcN was about 40% more than that of cyp alone. It is interesting to note that the cellular uptake of cyp-2GlcN was nearly double that of cyp-GlcN.

The uptake of cyp, which lacks a targeting carbohydrate moiety, was not inhibited by any of the tested sugars ($p>0.05$). Moreover, the uptake of cyp-2GlcN and cyp-GlcN was not significantly inhibited ($p>0.05$) by D-Glc, L-Glc, and GlcNAc (data not shown). These results may suggest that actively transported dyes such as cyp-2GlcN and cyp-GlcN are not taken up into prostate cells through glucose transporters, or that the GLUT-mediated transport was not completely blocked by co-incubation with the sugar
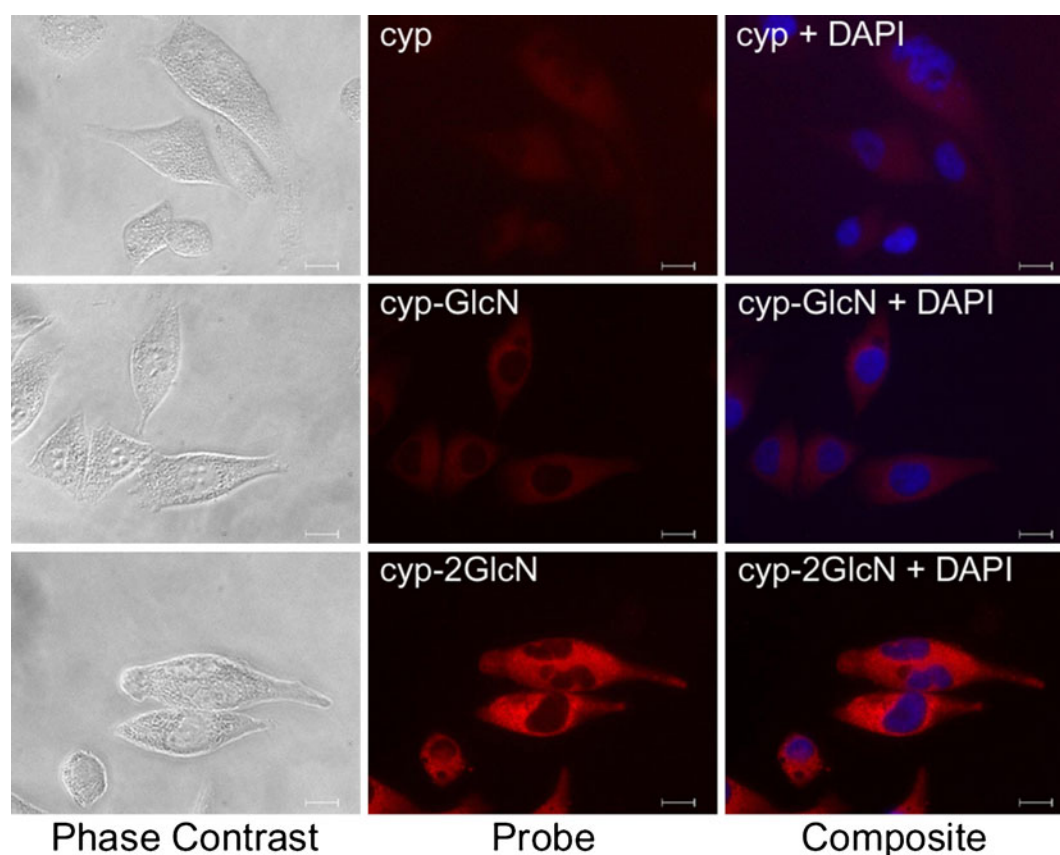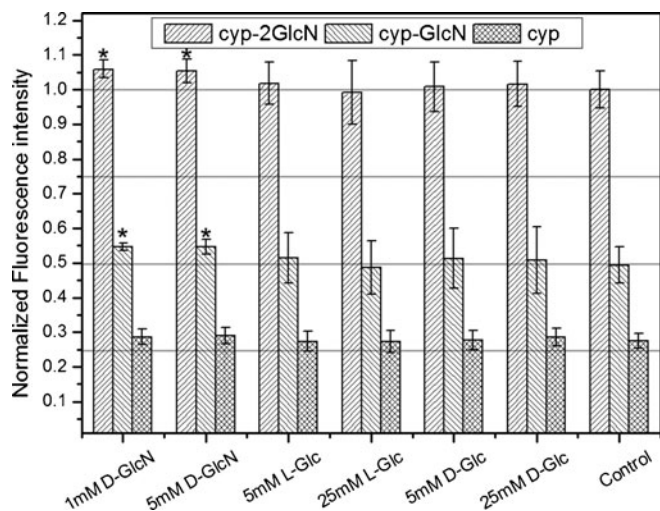

Fig. 2. Cellular uptake and localization of glucosamine NIRF probes. The cells were incubated with the different GlcN-linked probes for 1 h at 37°C to examine the tendency of the NIRF probes to accumulate in the cytoplasm of PC3-luc prostate cancer cells. (The *horizontal bar* in the photomicrographs represents 20 μm).

Fig. 3. Quantitative analysis of cellular uptake of the different NIRF probes in medium (*control*) and in presence of different sugars (1 mM D-GlcN, 5 mM D-GlcN, 5 mM L-Glc, 25 mM L-Glc, 5 mM D-Glc, 25 mM D-Glc, 25 mM Glc). The uptake of the cyp-2GlcN was significantly higher than the uptake of the cyp-GlcN and cyp. The uptake of the cyp-2GlcN and cyp-GlcN was not inhibited by D-Glc, L-Glc. D-GlcN caused a statistically significant increase in the uptake of the cyp-2GlcN and cyp-GlcN; *$p < 0.05$.

derivatives listed above. It is worth noting that similar results were reported by Cheng *et al*. [23] and Li *et al*. [24] experimenting with GlcN and NIRF dyes with molecular weight (MW) above 500. In contrast, the uptake of 2-deoxy-D-Glc with MW=342.26 can be inhibited by D-Glc but not L-Glc, thus suggesting the probe delivery and trapping in cells by GLUT/hexokinase pathway [26–28].

The co-incubation with D-GlcN exhibits an enhancement effect on the cellular uptake of the cyp-2GlcN and cyp-GlcN probes compared to uptake of free cyp ($p < 0.05$; see Fig. 3). This indicates that the GlcN transport system was activated by the excess amount of D-GlcN, thus facilitating the uptake of the GlcN-linked probes by PC3-luc cells. Different GLUTs might be involved in the uptake process. From this competitive study, we can pinpoint that transport of cyp-GlcN and cyp-2GlcN NIRF probes were active processes that were enhanced by D-GlcN, and could not be blocked by D-Glc. The results indicate that the uptake of cyp-2GlcN and cyp-GlcN is likely mediated by increased GlcN affinity of GLUTs or other transporters in the presence of GlcN. Due to complexity of sugar derivative metabolism in cancer cell, we cannot draw a final conclusion about the uptake mechanism and pathways involved in this process. More studies are needed in order to clarify the exact uptake and retention mechanism of these probes *in vitro*.

In Vivo and Ex Vivo Optical Imaging

Whole-body dynamic optical imaging of mice bearing PC3-luc human prostate tumor xenografts was performed after systemic administration of cyp and GlcN-linked NIRF probes, cyp-GlcN and cyp-2GlcN. cyp-2GlcN demonstrated the highest tumor-specific uptake and overall retention time in tumor as compared to the uptake and accumulation in surrounding tissues. The typical *in vivo* uptake of cyp-2GlcN is shown in Fig. 4. For cyp-2GlcN, the fluorescence in the tumor area was clearly observed up to 30 days after
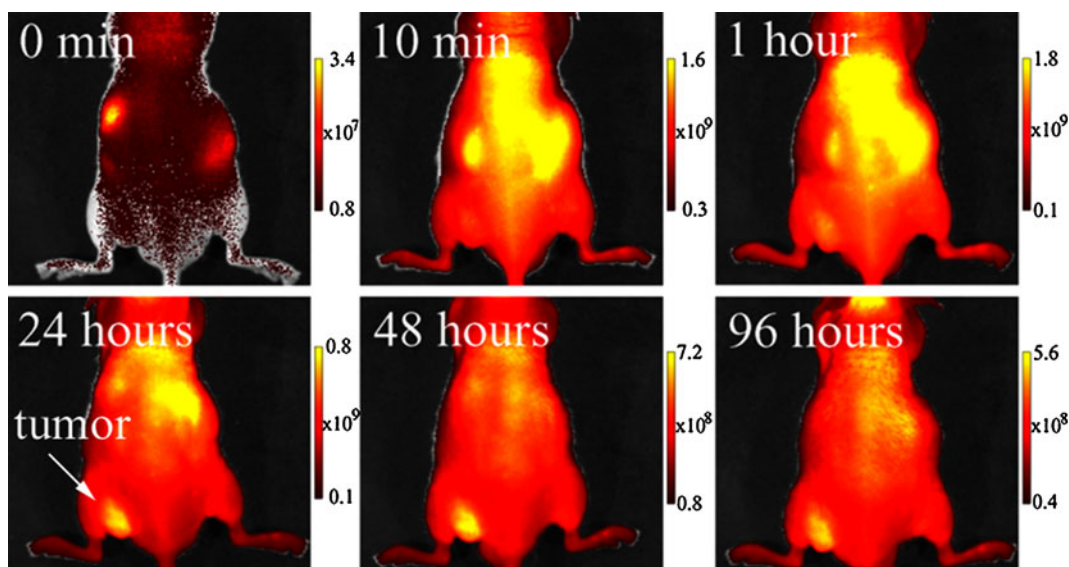
Fig. 4. *In vivo* dynamic imaging study of targeting specificity of cyp-2GlcN to PC3-luc prostate tumor xenografts. Representative superimposed photography and color-coded fluorescence *in vivo* images of human PC3-luc prostate tumor-bearing mice are shown at selected time points before and after intravenous administration of cyp-2GlcN (10 nmol). In order to show the tissue contrast at different time points, the window/level was adjusted for each picture individually. The absolute image intensity for the later time point is lower than that of the earlier time.

injection, while the maximum fluorescence intensity was evident 1 h after i.v. injection of the probe. However, remarkable fluorescence was observed for up to 6 h in the regions of the major excretion organs, such as the liver and kidneys. At 24 h after injection, a significant contrast in the tumor region was seen.

A quantitative analysis of whole-body dynamic optical imaging has been performed. Fluorescence intensities (average radiance, photons per second per centimeter squared per steradian) in PC3-luc prostate tumor xenografts and surrounding normal tissues as a function of time are shown in Fig. 5. It was found that cyp-GlcN and cyp-2GlcN exhibit specific uptake by tumors. The cyp-2GlcN demonstrated higher maximum fluorescence intensity and longer residence lifetime than cyp-GlcN and cypate molecule. The fluorescence of cyp-2GlcN, cyp-GlcN, and cyp reached its maximum intensity in the tumor region at 60, 30, and 1 min after i.v. injection, respectively. Maximum average radiance of cyp-2GlcN, cyp-GlcN, and cyp in the tumors was 9.6×10^9, 1.35×10^8, and 4.7×10^7 p/s/cm^2/sr, respectively, thus showing nearly one order higher uptake of probes with each addition of GlcN to the cyp core. The half-life of the NIRF probe was defined at the 50% of maximum of average radiance. The cyp-2GlcN possesses a higher half-life of 15 h compared to cyp-GlcN (1.7 h) and cyp (15 min). These results suggest that the addition of the second GlcN to a cyp imaging core can significantly improve tumor-targeting ability and retention time of the GlcN-linked NIRF probes *in vivo*.

The *ex vivo* biodistribution of cyp, cyp-GlcN, and cyp-2GlcN at 24 h after injection was investigated in tumor-bearing mice, and the results are shown in Fig. 6. Tumor uptakes of cyp-2GlcN and cyp-GlcN were four and twofold higher than that of cyp at 24 h after probe injection, respectively. The tumor muscle ratios at 24 h after i.v. administratiion of cyp-2GlcN, cyp-GlcN, and cyp were 7.8:1, 3.8:1, and 2.0:1, respectively. The fluorescence signal of cyp-2GlcN after 20 days of i.v. injection was nearly one order less but still quite high (2.8×10^7 p/s/cm^2/sr), and the

tumor to muscle signal ratio was around 3.7:1. The *ex vivo* biodistibution results are consistent with results of *in vivo* study except that the tumor to muscle signal ratios are higher in *ex vivo* studies. This may reflect the lack of skin emission and absence of light penetration depth effects on the fluorescence intensities from different organs and tumors in *ex vivo* experiments. It is noticeable that cyp-2GlcN was also retained in the liver and kidneys for prolonged duration with relatively high uptake in the liver. There could be two reasons for probe accumulation in these organs. This may be explained partly on the basis of probe entrapment in the rich reticuloendothelial system characteristic of the liver and kidneys and escape from engulfment by macrophages. The high levels of GLUT2, which is a high-affinity glucosamine transporter [19], in the liver and kidneys [13] could also account for the high levels of the probe in these organs. The washout of the probe from other organs and tissues could be mediated through renal and biliary routes and cause additional amounts of the probe to be in transit through the liver and kidneys. *Ex vivo* biodistribution studies show that the probe with two GlcN moieties (cyp-2GlcN) exhibits the highest uptake in the liver and kidneys compared to probe linked to one GlcN unit (cyp-GlcN) and the unconjugated dye (cyp). On the other hand, the *in vivo* biodistribution study clearly showed high levels of accumulation and retention of cyp-2GlcN in PC3-luc prostate tumor xenografts in mice.

The *in vivo* uptake specificity of cyp-2GlcN was tested by competitive uptake study at 24 h post-injection. Thirty minutes prior to i.v. probe injection, the mice were pre-injected with D-Glc, or D-ClcN, or GlcNAc intraperitoneally. At 24 h after injecting the probe, the mice were sacrificed, and the major organs were excised and collected for *ex vivo* biodistribution analysis (Fig. 7). The results of this study showed that the *in vivo* uptake of the probe was not inhibited by D-Glc. These results are similar to those described earlier for the effects of D-Glc on probe uptake by PC3-luc cells in culture. This indicates that the probe transport was facilitated not only by glucose metabolism, but by some other complex
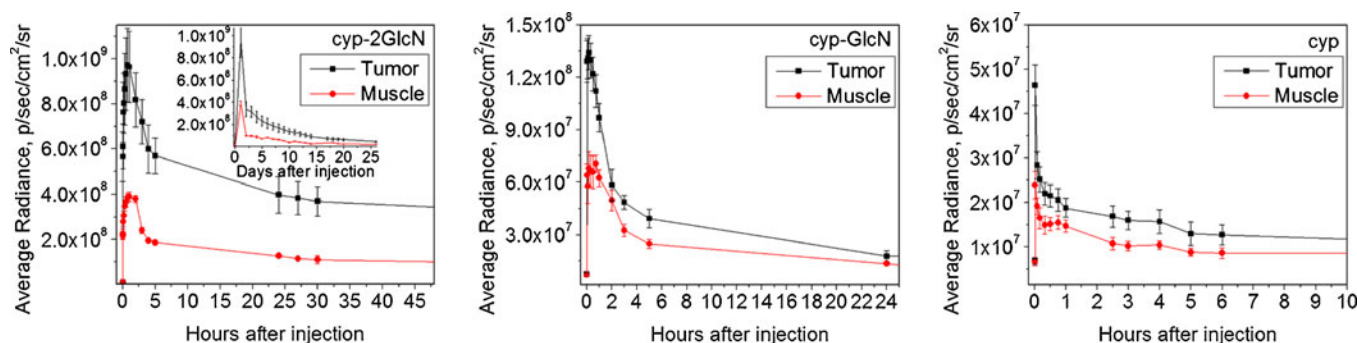

Fig. 5. Kinetics of *in vivo* targeting characteristics of cypate and glucosamine-based probes in PC3-luc prostate tumor xenografts. Typical time course of *in vivo* fluorescence intensities (average radiance) after i.v. administration of 10 nmol of cyp, cyp-GlcN, and cyp-2GlcN is shown for the first 50, 24, and 10 h of the *in vivo* imaging, respectively. The autofluorescence signal was measured just before injection (*zero time point in the time axis*). Cyp-2GlcN demonstrated higher maximum fluorescence intensity and longer residence lifetime (see *insert on the first panel*) than cyp-GlcN and cyp. The *insert* represents the maximum *in vivo* fluorescence intensities per day over 26 days.
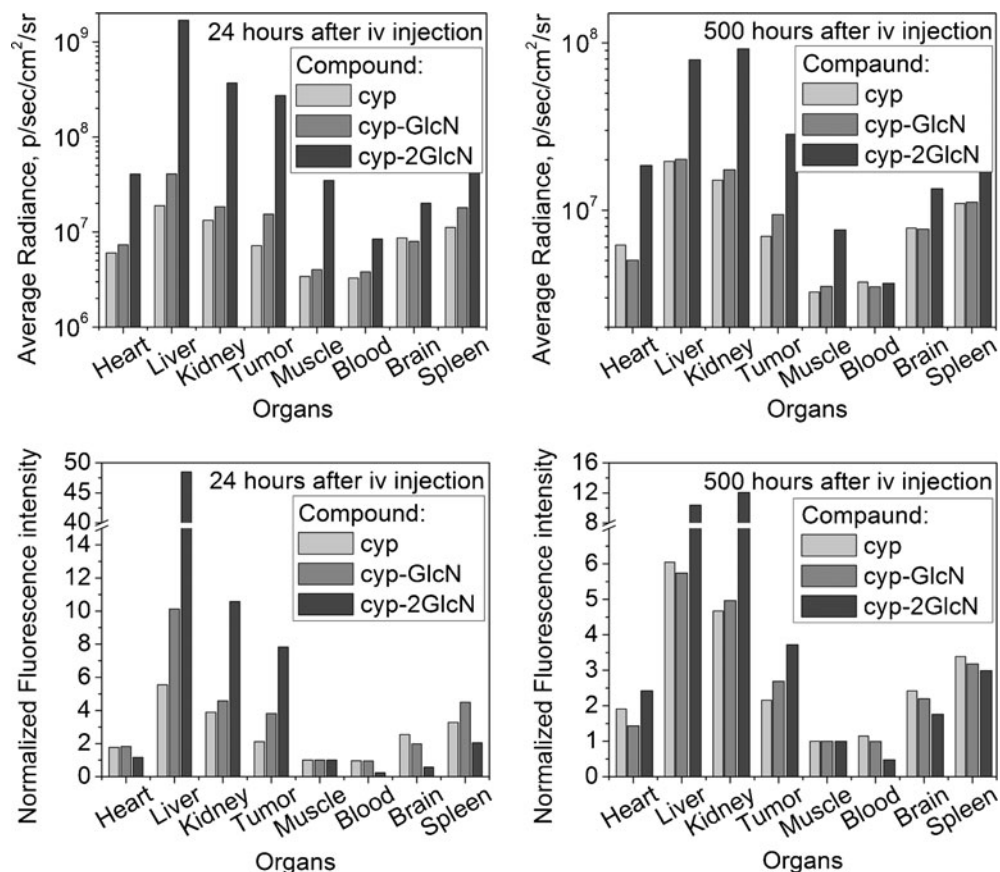
Fig. 6. *Ex vivo* study of biodistribution of molecular probes in PC3-luc prostate tumor-bearing mice. The *top two panels* represent the fluorescence intensities (average radiance) at 24 h (*left panel*) and 500 h (*right panel*) after systemic intravenous injection of the cyp-2GlcN, cyp-GlcN, and cyp. The *bottom row* of the histograms show the corresponding fluorescence intensities normalized to the muscle signal. Cyp-2GlcN had the best tumor-targeting ability and retention characteristics. Tumor uptakes of cyp-2GlcN and cyp-GlcN were four and twofold higher than that of cyp at 24 h post-injection.

metabolic processes in the tumor. Interestingly, the *in vivo* uptake of cyp-2GlcN was inhibited by GlcNAc, while in *in vitro* experiments, GlcNAc had no effect on cyp-2GlcN uptake. The inhibition of cyp-2GlcN uptake *in vitro* was negligibly small, probably due to the low GlcNAc to cyp

ratio, compared to the much higher GlcNAc to cyp ratio used for *in vivo* experiments. GlcNAc is generated during lysosomal degradation of certain glycoproteins and glycosaminoglycans by lysosomal enzymes and recycled by the cell [29]. It was reported that lysosomes possess a highly
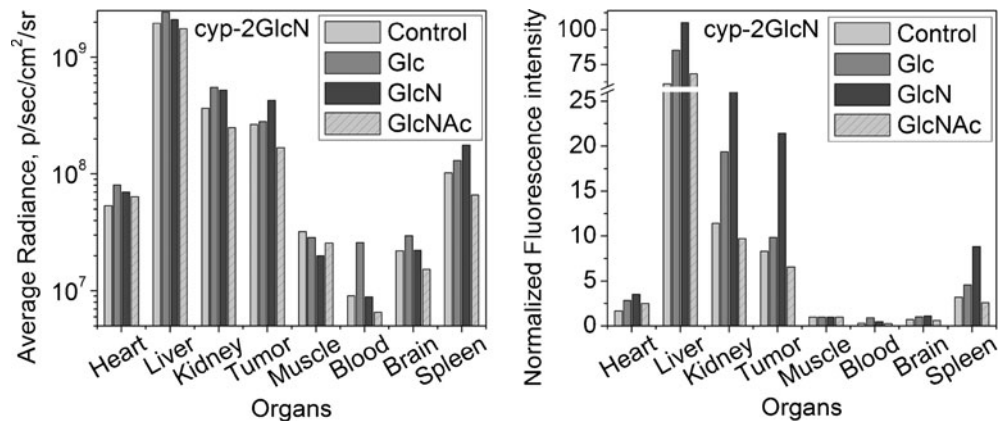
Fig. 7. Competitive uptake study of cyp-2GlcN. *Left panel* represents the biodistribution at 24 h after i.v. injection of cyp-2GlcN in mice pre-injected with D-Glc, D-GlcN, and GlcNAc. *Right panel* represents the corresponding fluorescence intensities normalized to the fluorescent signal from the muscle. The uptake of the cyp-2GlcN was not inhibited by D-Glc. The uptake of cyp-2GlcN was inhibited by GlcNAc and enhanced by D-GlcN.

specific transport system for *N*-acetyl-D-glucosamine and *N*-acetyl-D-galactosamine [30]. We assume that the lysosomal transport and trafficking were partially blocked by pre-injection of *N*-acetyl-D-glucosamine *in vivo*. As a result, the cypate-glucosamine NIRF probe accumulation in the cells was reduced not only in the tumor but also in organs with a rich reticuloendothelial system. The uptake of the probe in prostate tumors was significantly enhanced by pre-injection of GlcN. As we proposed earlier, *in vivo* results suggest that cyp-2GlcN uptake is through the GlcN-sensing transporters that could be activated by GlcN IP pre-injection. It is well known from the literature that infusion of D-GlcN can decrease insulin-stimulated Glc uptake and stimulate the hexosamine biosynthesis pathway [31, 32]. As a result of these changes, the cell might signal increased uptake of GlcN and glucosamine-linked probes.

The findings in this study support the initial hypothesis that two GlcN conjugated to NIRF dye will improve targeting properties of the NIRF probe and have potential for metabolic imaging. GLUT1 and GLUT4 have similar affinities for glucose and GlcN, and extracellular concentration of glucose is higher than GlcN, even during glucosamine infusions [19, 33]. At least two mechanisms have been reported for the cellular utilization of GlcN [19, 34, 35]. GlcN is carried into cells by GLUTs and phosphorylated to glucosamine-6-phosphate by hexokinase activity of glycolytic pathway. The second pathway is transcriptional in which the regulatory products derived from glucosamine-6-phosphate are involved in translocation, transcription, and insulin action cascade. Overexpression of different GLUT types may lead to higher or lower specificity of GlcN-based NIRF probes in different types of cancers. GlcN-containing NIRF probes seem to be good candidates for metabolic imaging of tumors. Unfortunately, the transport mechanism of GlcN-conjugated NIRF probes is still unclear. GlcN and Glc may share some of the same carriers and enzymes for transport and metabolic processing in tumor tissue. *In vivo* cellular uptake studies of technetium-labeled Glc analogs [36, 37] have shown similarities with uptake characteristics of GlcN-linked NIRF probes, especially with respect to insensitivity to Glc. *In vivo* cellular uptake of FDG on the other hand is quite sensitive to Glc concentration. This suggests that the transport of GlcN-linked NIRF probes and technetium-labeled Glc may involve a common mechanism (s). Furthermore, D- GlcN has been reported to inhibit growth of many types of cancer cells *in vivo* and *in vitro* [38–40], and thus has potential to expand the usage of GlcN-based NIRF probes from cancer diagnosis and monitoring of cancer treatment to theranostics of cancer.

Conclusion

In summary, both cyp-GlcN and cyp-2GlcN NIRF probes have demonstrated good tumor-targeting properties in prostate cancer cells *in vitro* and in live mice. The probe constructed with two GlcN, cyp-2GlcN, showed the highest uptake with prolonged half-life *in vivo*. The uptake of cyp-2GlcN and cyp-GlcN was tumor specific, active, and likely mediated by GlcN-recognizing transporters. The uptake mechanism is being explored further for developing cypate-GlcN-based probes for *in vivo* applications. This study showed that the addition of a second GlcN can significantly change NIRF probe characteristics, resulting in better and prolonged tumor contrast and improved pharmacokinetics. This general idea of probe design can be applied to future NIRF probe development in cancer theranostics.

Conflicts of Interest. The authors declare that they have no conflict of interest.

References

1. Semmler W, Schwaiger M, Schulz RB (2008) Fundamentals of optical imaging. In: Hofmann FB (ed) Molecular imaging I (handbook of experimental pharmacology), vol. 185/1. Springer, Heidelberg, pp 3–22
2. Ntziachristos V, Bremer C, Weissleder R (2003) Fluorescence imaging with near-infrared light: new technological advances that enable *in vivo* molecular imaging. Eur Radiol 13:195–208
3. Massoud TF, Gambhir SS (2003) Molecular imaging in living subjects: seeing fundamental biological processes in a new light. Genes Dev 17:545–580
4. Weissleder R (2001) A clearer vision for *in vivo* imaging. Nat Biotechnol 19:316–317
5. Ghoroghchian PP, Therien MJ, Hammer DA (2009) *In vivo* fluorescence imaging: a personal perspective. Wiley Interdiscip Rev Nanomed Nanobiotechnol 1:156–167
6. Shah K, Weissleder R (2005) Molecular optical imaging: applications leading to the development of present day therapeutics. NeuroRX 2:215–225
7. Hilderbrand SA, Weissleder R (2010) Near-infrared fluorescence: application to *in vivo* molecular imaging. Curr Opin Chem Biol 14:71–79
8. Eisenblätter M, Höltke C, Persigehl T et al (2010) Optical techniques for the molecular imaging of angiogenesis. Eur J Nucl Med Mol Imaging 37:127–137
9. El-Deiry WS, Sigman CC, Kelloff GJ (2006) Imaging and oncologic drug development. J Clin Oncol 24:3261–3273
10. Pene F, Courtine E, Cariou A et al (2009) Toward theragnostics. Crit Care Med 37:S50–S58. doi:10.1097/CCM.0b013e3181921349
11. Macheda ML, Rogers S, Best JD (2005) Molecular and cellular regulation of glucose transporter (GLUT) proteins in cancer. J Cell Physiol 202:654–662
12. Shaw RJ (2006) Glucose metabolism and cancer. Curr Opin Cell Biol 18:598–608
13. Calvo M, Figueroa A, Pulido E et al (2010) Potential role of sugar transporters in cancer and their relationship with anticancer therapy. Int J Endocrinol 2010:14
14. Gambhir SS (2002) Molecular imaging of cancer with positron emission tomography. Nat Rev Cancer 2:683–693
15. Gatenby RA, Gillies RJ (2007) Glycolysis in cancer: a potential target for therapy. Int J Biochem Cell Biol 39:1358–1366
16. Kaarstad K, Bender D, Bentzen L et al (2002) Metabolic fate of 18F-FDG in mice bearing either SCCVII squamous cell carcinoma or C3H mammary carcinoma. J Nucl Med 43:940–947
17. Schwartzenberg-Bar-Yoseph F, Armoni M, Karnieli E (2004) The tumor suppressor p53 down-regulates glucose transporters GLUT1 and GLUT4 gene expression. Cancer Res 64:2627–2633
18. Rubin SJ, Hallahan DE, Ashman CR et al (1991) Two prostate carcinoma cell lines demonstrate abnormalities in tumor suppressor genes. J Surg Oncol 46:31–36
19. Uldry M, Ibberson M, Hosokawa M et al (2002) GLUT2 is a high affinity glucosamine transporter. FEBS Lett 524:199–203

20. Effert P, Beniers AJ, Tamimi Y et al (2004) Expression of glucose transporter 1 (Glut-1) in cell lines and clinical specimens from human prostate adenocarcinoma. Anticancer Res 24:3057–3064
21. Chandler JD, Williams ED, Slavin JL et al (2003) Expression and localization of GLUT1 and GLUT12 in prostate carcinoma. Cancer 97:2035–2042
22. Pysz M, Gambhir S, Willmann J (2010) Molecular imaging: current status and emerging strategies. Clin Radiol 65:500–516
23. Cheng Z, Levi J, Xiong Z et al (2006) Near-infrared fluorescent deoxyglucose analogue for tumor optical imaging in cell culture and living mice. Bioconjug Chem 17:662–669
24. Li C, Greenwood T, Glunde K (2008) Glucosamine-bound near-infrared fluorescent probes with lysosomal specificity for breast tumor imaging. Neoplasia 10:389–398
25. Ye Y, Bloch S, Kao J et al (2005) Multivalent carbocyanine molecular probes: synthesis and applications. Bioconjug Chem 16:51–61
26. Yoshioka K, Takahashi H, Homma T et al (1996) A novel fluorescent derivative of glucose applicable to the assessment of glucose uptake activity of *Escherichia coli*. Biochim Biophys Acta 1289:5–9
27. O'Neil R, Wu L, Mullani N (2005) Uptake of a fluorescent deoxyglucose analog (2-NBDG) in tumor cells. Mol Imaging Biol 7:388–392
28. Millon S, Ostrander J, Brown J et al (2011) Uptake of 2-NBDG as a method to monitor therapy response in breast cancer cell lines. Breast Cancer Res Treat 126:55–62
29. Rome L, Hill D (1986) Lysosomal degradation of glycoproteins and glycosaminoglycans. Efflux and recycling of sulphate and *N*-acetylhexosamines. Biochem J 235:707–713
30. Jonas AJ, Speller RJ, Conrad PB et al (1989) Transport of *N*-acetyl-D-glucosamine and *N*-acetyl-D-galactosamine by rat liver lysosomes. J Biol Chem 264:4953–4956
31. Virkamäki A, Daniels MC, Hämäläinen S et al (1997) Activation of the hexosamine pathway by glucosamine *in vivo* induces insulin resistance in multiple insulin sensitive tissues. Endocrinology 138:2501–2507
32. Patti ME, Virkamäki A, Landaker EJ et al (1999) Activation of the hexosamine pathway by glucosamine *in vivo* induces insulin resistance of early postreceptor insulin signaling events in skeletal muscle. Diabetes 48:1562–1571
33. Virkamäki A, Yki-Järvinen H (1999) Allosteric regulation of glycogen synthase and hexokinase by glucosamine-6-phosphate during glucos-amine-induced insulin resistance in skeletal muscle and heart. Diabetes 48:1101–1107
34. Marshall S, Bacote V, Traxinger R (1991) Discovery of a metabolic pathway mediating glucose-induced desensitization of the glucose transport system. Role of hexosamine biosynthesis in the induction of insulin resistance. J Biol Chem 266:4706–4712
35. Wells L, Vosseller K, Hart G (2001) Glycosylation of nucleocytoplasmic proteins: signal transduction and O-GlcNAc. Science 291:2376–2378
36. Yang DJ, Kim C-G, Schechter NR et al (2003) Imaging with 99mTc ECDG targeted at the multifunctional glucose transport system: feasibility study with Rodents1. Radiology 226:465–473
37. Chen Y, Xiong Q, Yang X et al (2007) Noninvasive scintigraphic detection of tumor with 99mTc-DTPA-deoxyglucose: an experimental study. Cancer Biother Radiopharm 22:403–405
38. Oh H-J, Lee JS, Song D-K et al (2007) d-Glucosamine inhibits proliferation of human cancer cells through inhibition of p70S6K. Biochem Biophys Res Commun 360:840–845
39. Park J-Y, Park J-W, Suh S-I et al (2009) d-Glucosamine down-regulates HIF-1[alpha] through inhibition of protein translation in DU145 prostate cancer cells. Biochem Biophys Res Commun 382:96–101
40. Matheson D, Green B, Friedman S (1984) Effect of D-glucosamine on human natural killer activity *in vitro*. J Biol Response Mod 3:445–453

pH Sensitive Nanoprobe for Tumor Targeting

CS Wu[1], S. Huang[1], A Korotcov[1], Y Chen[1], S Lin[1], OA Andreev[2], YK Reshetnyak[2] and PC Wang[1, *]

[1] Molecular Imaging Laboratory, Department of Radiology, Howard University, Washington DC
[2] Physics Department, University of Rhode Island, Rhode Island RI

Background

pHLIP is a low pH-sensitive peptide that transforms into an α-helix and inserts across a cell membrane at a low pH (<7.0) environment (Fig. 1). In almost all solid tumors, the increased glucose catabolism results in significant production of lactate and H^+ ions, which are pumped out from the intracellular space, producing an acidic extracellular tumor environment. In this study, *in vivo* tumor uptake and the targeting capability of fluorescently-labeled pHLIP probe in a breast cancer model was investigated.
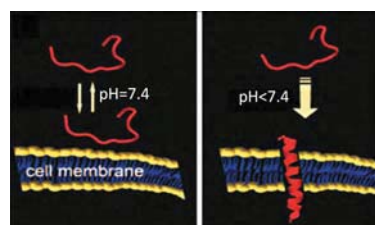
Fig. 1 The schematic diagram[1] of pHLIP insertion into the cell membrane. The mechanism has three steps: soluble in water, attached to the surface of membrane, and inserted across the lipid bilayers.

Methods

pHLIP sequence. pHLIP was prepared by solid-phase peptide synthesis. Near-infrared (NIR) fluorescent dye, Alexa 750, was conjugated with Cys residues placed on the pHLIP N terminus using the crosslinker benzophenone-4-iodoacetamide.

ACEQNPIYWARYADWLFTTPLLLLDLALLVDADEGT

Fluorescence Imaging of tumor. The breast cancer tumor model was established by subcutaneous injection of 1×10^6 MDA-MB-231-luc cells in female athymic nude mice. Caliper Spectrum Imaging machine was used for bioluminescence and fluorescence imaging. Bioluminescence images were used to monitor tumor growth. The fluorescence experiment was run when tumors reached 8-10 mm in diameter. Mice were intravenously injected with 40 µM of pHLIP probe in 100 µl of phosphate buffered saline (PBS). Fluorescence imaging was acquired every 15 minutes during the first hour, and then was acquired hourly for 24 hours, and then daily for another 5 days after injection of pHLIP.

***In vivo* NMR spectroscopy for pH measurement.** In order to measure the intracellular and extracellular tumor pH values, ^{31}P NMR spectra were obtained with a Bruker Advance I 400 MHz spectrometer. Extracellular pH (pH_e) was calculated using the chemical shift of 3-aminopropylphosphonate (3-APP) based on the equation:

$$pH_e = 6.91 - \log\left(\frac{\delta_{3-APP} - 21.11}{24.3 - \delta_{3-APP}}\right) \text{ [2]}$$

Similarly, intracellular pH (pH_i) was calculated based on the chemical shift of P_i using the equation:

$$pH_i = 6.97 + \log\left(\frac{\delta P_i - 0.77}{3.16 - \delta P_i}\right) \text{ [2]}$$

Before spectroscopy, mice were anesthetized with isoflurane. Once anesthetized, they were immobilized on a cradle containing a ^{31}P surface coil (Fig 2).
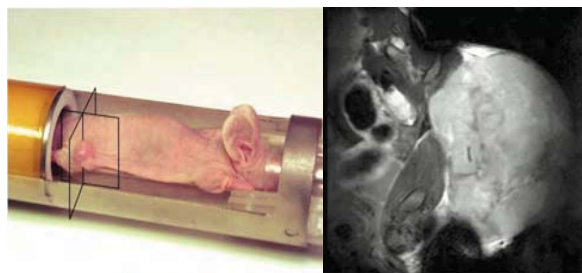

Fig. 2 The imaging set up with mouse inside the RF coil (left), and the MRI image of tumor.

Results

High fluorescent signal was observed in the subcutaneous tumors, which reflects elevated pHLIP probe uptake in the tumor region. The maximum fluorescence intensity was observed 1 hour post-injection. Significant fluorescence signal was observed for up to 4 hours in regions of the brain, spine, and kidneys (Fig 3A and 3B). At 24 hours, fluorescence intensity in tumor region was high, and the signal from kidneys was still detectable. The highest tumor to muscle tissue ratio was 7 hours post-injection. 95% of the fluorescent signal in the body was washed out 4 days post-injection. The NMR spectra (Fig. 4) show chemical shifts of P_i and 3-APP and pH values are shown in Table 1.
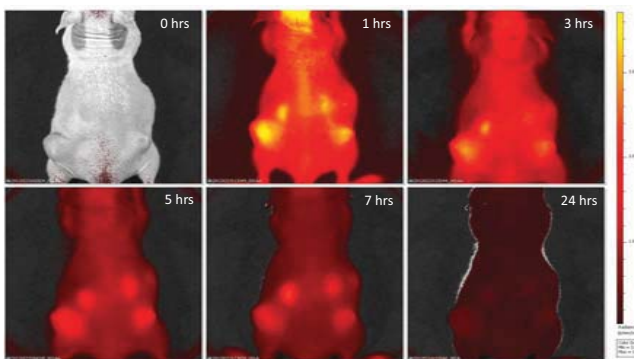
Fig 3A Optical detection of tumor after i.v. administration of pHLIP
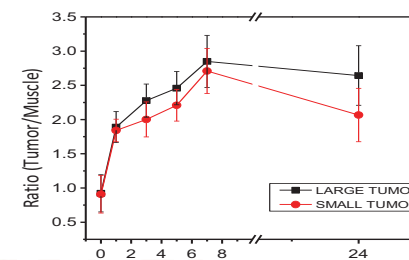
Fig. 3B The change in the ratio of tumor to muscle fluorescence signal in small and large tumors over time
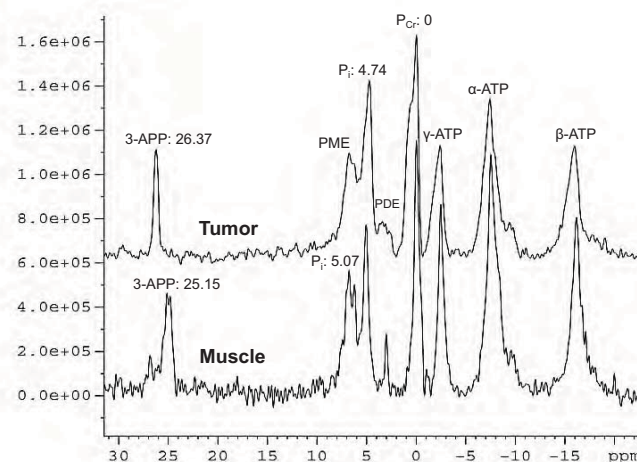
Fig. 4 ^{31}P NMR spectra of tumor and normal muscle in presence of 3-APP. P_{Cr} peak is the reference at 0 ppm.

	pH_i	pH_e	pH meter
Tumor	7.14	6.24	6.85
Muscle	7.42	6.96	7.12

Table 1 The pH values of tumor and normal muscle using *in vivo* NMR spectroscopy and pH meter

Conclusions

pHLIP presents a useful tool to target acidic tissue environments. The pH-sensitive nanoprobe demonstrated good tumor-targeting properties in breast cancer xenografts *in vivo*. pHLIP is non-toxic to cells and could be used as a cancer drug carrier to reduce the side-effects associated with chemotherapy. This novel pH-sensitive peptide has potential use in targeted drug delivery, treating acidic disease tissue, detection of small tumors, and diagnostic imaging.

References

1. Andreev, O.A., et al., Proc Natl Acad Sci ,2007.104(19):p.7893-7898
2. Bhujwalla, Z.M., et al., British Jounal of Cancer,1998.78(5):p.606-611

Article type: Full Paper

An Anti-PSMA Bivalent Immunotoxin Exhibits Specificity and Efficacy for Prostate Cancer Imaging and Therapy

Fayun Zhang, Liang Shan, Yuanyi Liu, David Neville, Jung-Hee Woo, Yue Chen, Alexandru Korotcov, Stephen Lin, Sophia Huang, Rajagopalan Sridhar, Wei Liang, Paul C. Wang*

[*]   P. C. Wang, F. Zhang, L. Shan, Y. Chen, A. Korotcov, S. Lin, S. Huang, R. Sridhar
Molecular Imaging Laboratory
Department of Radiology
Howard University
Washington, DC, 20060 (USA)
E-mail: pwang@howard.edu

        F. Zhang, W. Liang
Protein & Peptide Pharmaceutical Laboratory
National Laboratory of Biomacromolecules
Institute of Biophysics
Chinese Academy of Sciences
Beijing, 100101 (China)

        L. Shan
National Center for Biotechnology Information
National Institutes of Health
Bethesda, MD, 20892 (USA)

        Y. Liu, D. Neville
Angimmune LLC
Bethesda, MD, 20852 (USA)

        J-H. Woo
Cancer Research Institute of Scott and White Healthcare
Texas A&M Health Science Center
Temple, TX 76502 (USA)

Supporting Information is available on the WWW under http://www.small-journal.com

Abstract: Prostate specific membrane antigen (PSMA) is overexpressed on prostate tumor cells and the neovascular endothelia various solid tumors. A bivalent immunotoxin generated by fusing a fold-back single-chain diabody derived from the Fv fragments of an anti-PSMA monoclonal antibody with a truncated diphtheria toxin (DT) containing the activity and translocation domains [A-dmDT390-scfbDb(PSMA)] might be suitable for targeted therapy of tumors that overexpress PSMA. In this study, a PSMA-positive and a PSMA-negative prostate cancer cell lines were treated with immunotoxin A-dmDT390-scfbDb(PSMA) in order to study the tumor targeting specificity and therapeutic potential of the immunotoxin. The cellular uptake and selective toxicity of the immunotoxin were evident in monolayer cultures of PSMA-positive LNCaP prostate cancer cells but not in cultures of PSMA-negative PC-3 prostate cancer cells. Cellular accumulation of A-dmDT390-scfbDb(PSMA) increased with increasing incubation times and concentrations in LNCaP cells. The proportion of apoptotic LNCaP cells increased upon incubation with increasing doses of the fold-back immunotoxin. Optical imaging and MRI with the Alexa Fluor 680-labeled A-dmDT390-scfbDb(PSMA) confirmed the specific targeting and therapeutic efficacy of this immunotoxin towards PSMA-positive LNCaP solid tumor xenografts in athymic nude mice.

1. Introduction

Prostate cancer is the most common solid tumor and one of the leading causes of cancer-related death among American men.[1] Radiotherapy and/or surgery with or without androgen deprivation are used for management of early stage, organ-confined prostate cancer. A subset of early stage cancer may progress to an aggressive metastatic disease, which does not respond to androgen deprivation. Chemotherapeutic approaches are used for treating metastatic prostate cancer. The development of androgen resistance and systemic off-target toxicities of conventional chemotherapeutic drugs such as docetaxel and mitoxantrone are major clinical challenges.[2-3] There is a need for safe and effective therapies that are based on specific targeting of immunotoxins to tumors. Tumor cells often express high levels of surface receptors or other molecules that distinguish them from other cells. Ligands designed to bind to tumor-specific receptors can be conjugated to cytotoxic drugs or toxins and the resulting conjugates provide a tumor targeted drug delivery system for safe and effective therapy.[4] Further research along these lines may lead to molecularly targeted individualized therapy.

Prostate-specific membrane antigen (PSMA) is over-expressed on the surface of certain prostate cancer cells. It is noteworthy that PSMA expression is particularly pronounced when prostate cancer progresses to late stage and becomes androgen-independent and metastatic.[5] PSMA expression in certain prostate cancer cells is 1000-fold higher than in normal prostate tissue.[6] PSMA is also expressed on the neovascular endothelium of a wide variety of human solid tumors, but is not expressed in the blood vessels of normal tissue.[7] These findings have prompted the use of monoclonal antibody (mAb) of PSMA for sensitive and specific tumor imaging [8] as well as targeted drug delivery for treating prostate cancer and other solid tumors.[9]

PSMA antibody or its fragments, such as single-chain antibody fragments (scFv), can deliver cytotoxic agents into PSMA-expressing cells.[10] scFv consists of the variable heavy chain (V_H) and the variable light chain (V_L) of an antibody connected by a flexible peptide

linker and, due to its small size, exhibits better tumor penetration, improved tumor distribution, and faster blood clearance than a full antibody when it is used as a ligand for targeted drug delivery.[11]

The truncated form of diphtheria toxin (DT390) constructs incorporated in the immunotoxin exhibits targeted cytotoxicity [12-13] and bioactivity *in vivo*. [14-15] The DT-based anti-CD3 bivalent immunotoxin, A-dmDT390-bisFv (UCHT1), has been shown to bind to its target and depletes T cells effectively. [16] This immunotoxin has undergone preclinical studies [17-18] and is currently in clinical trials for treating cutaneous T-cell lymphoma (clinical trial identifier NCT00611208). In general, bivalent immunotoxins containing two scFv units have higher affinity and efficacy towards the targeted cells than those containing one scFv. [13,19] It has also been shown that the format of scFv bivalency strongly affects binding affinity and immunotoxin cytotoxicity, depending on the antibody Fv sequences. The ant-monkey CD3 bivalent immunotoxin with a fold-back single-chain diabody, A-dmDT390-scfbDb(207), showed a 5- to 7-fold enhanced bioactivity over that containing two tandem unites of scFv (biscFv).[19] To effectively deliver DT390 and enhance the specificity of its targeting to PSMA-expressing cells, we constructed an anti-PSMA fold-back single-chain diabody (scfbDb, **Figure 1A**) based on the Fv sequences of the murine anti-PSMA antibody J591 and fused it to the C-terminus of DT390 using the approach similar to that for constructing anti-CD3 immunotoxin A-dmDT390-scfbDb(207) [19]. As shown in Figure 1B and C, the bivalent anti-PMSA immunotoxin, A-dmDT390-scfbDb(PSMA), has a sequence of DT390-L1-V_L-L1-V_H-L2-V_L-L1-V_H where L1 is a five-residue linker and L2 is the longer $(G_4S)_3$ linker, permitting interactions between the distal and proximal V_L/V_H domains. Preliminary studies showed that the scfbDb bound to the extracellular domain of PSMA with a higher affinity than biscFv and single scFv formats at a ratio of 7:2.5:1 (scfbDb:biscFv:scFv). This finding indicates that the scfbDb (PSMA) may be more sensitive and specific for targeted imaging

and therapy. Previous *in vitro* studies have further demonstrated that the anti-PSMA fold-back diabody efficiently mediates the entry of the truncated toxin across the cell membrane into the cytosol and the fold-back format immunotoxin is 18- to 30-fold more potent than the biscFv format against monolayer LNCaP cancer cells[20].

For targeted immunotoxin therapy, it is important to determine the response of tumor cells to therapy. It would be useful if the target molecules expressed on the tumor cells could be identified before treatment, and the therapeutic dynamics and mechanisms could be imaged noninvasively during the targeted immunotoxin therapy. In this report, we laid the groundwork for evaluating the targeting specificity and therapeutic potential of the immunotoxin construct A-dmDT390-scfbDb(PSMA) with noninvasive optical imaging.

In this study, A-dmDT390-scfbDb(PSMA) was conjugated to Alexa Fluor 680 dye and used to investigate its utility for tumor-specific imaging and treatment. For this purpose, prostate cancer cells were grown *in vitro* as monolayer cultures and *in vivo* as solid tumor xenografts in athymic nude mice. The results confirmed that A-dmDT390-scfbDb(PSMA) immunotoxin had specific tumor targeting property in addition to a distinct and potent anticancer activity against PSMA-positive prostate cancer but not against PSMA-negative prostate cancer.

2. Results and Discussion

PSMA is known to be highly expressed and rapidly internalized in malignant prostate cancer cells. However, it is minimally expressed in benign tumors and normal tissues. The PSMA antibody fragment scFv has been used to bind specifically to prostate cancer cells for prostate cancer therapy [21-22] and some PSMA-targeted therapeutics have been investigated in clinical trials.[23-24] In this study, we demonstrated that the conjugate of a fold-back single-chain diabody of anti-PSMA monoclonal antibody fused to the translocation domains of diphtheria toxin (A-dmDT390-scfbDb(PSMA)) inhibited the growth of PSMA-positive LNCaP cancer cells both *in vitro* and *in vivo* but not the growth of PSMA-negative PC-3 cells.

The specific toxicity towards LNCaP cells indicated that scfbDb(PSMA) bound specifically to the PSMA antigen on the cell membrane and effectively delivered DT390 into the PSMA-expressing cells to induce cytotoxicity.

2.1. PSMA is overexpressed in LNCaP but not in PC-3 cells

The expression of PSMA in LNCaP and PC-3 cells was determined with immunofluorescence staining and Western blotting. The results showed high levels of PSMA expression in LNCaP cells, but not in PC-3 cells **(Figure 2)**.

2.2. A-dmDT390-scfbDb(PSMA) inhibits proliferation of LNCaP cells.

The inhibitory effects of A-dmDT390-scfbDb(PSMA) on the proliferation and viability of LNCaP cells and PC-3 cells were investigated with a methylthiazolyl tetrazolium (MTT) assay. Cells were treated with various concentrations of A-dmDT390-scfbDb(PSMA) immunotoxin for 48 hours. LNCaP cells were found to be highly sensitive to A-dmDT390-scfbDb(PSMA) immunotoxin, showing an IC_{50} of 0.57 nM **(Figure 3)**. MTT assay showed 75% killing of the LNCaP cells after 48 hours of treatment. The viability of PC-3 cells was not affected by the immunotoxin even at a relatively high concentration of 100 nM.

2.3. Cellular uptake and accumulation are high in LNCaP cells but not in PC3 cells

A-dmDT390-scfbDb(PSMA) was labeled with Alexa Fluor 680. The cellular uptakes and accumulations of the Alexa Fluor 680-labeled immunotoxin were detected with fluorescence microscopy and flow cytometry. As shown in **Figure 4**, the intensity of Alexa Fluor 680 fluorescence increased under microscopy with increasing concentrations of A-dmDT390-scfbDb(PSMA) from 0.01 µM to 0.1 µM. Similarly, increased red fluorescence was observed in LNCaP cells treated with 0.1 µM of the labeled A-dmDT390-scfbDb(PSMA) when incubated for longer periods **(Figure 5)**. In contrast, no Alexa Fluor 680 fluorescence signal could be detected in PC-3 cells even after 4 hours of incubation with Alexa Fluor 680-labeled A-dmDT390-scfbDb(PSMA) and at a relatively high concentration (0.2 µM) **(Figure S1)**. The flow cytometry showed that an increase in the concentration and incubation time

resulted in more accumulation of labeled A-dmDT390-scfbDb(PSMA) in LNCaP cells (**Figure 6**). Incubation with 0.1 µM of labeled A-dmDT390-scfbDb(PSMA) for 6 hours caused significant accumulation of the labeled immunotoxin in the LNCaP cells but not in the PC-3 cells (**Figure S2**). The heterogeneous distribution of the signal observed under microscopy is largely due to the different stages of cell proliferation and various expression levels of PSMA of the cells.

2.4. A-dmDT390-scfbDb(PSMA) induces cell arrest and apoptosis of LNCaP prostate cancer cells.

LNCaP cells were incubated with graded concentrations (0 to 5 nM) of A-dmDT390-scfbDb(PSMA) for 24 hours and stained with propidium iodide (PI), whichbinds with DNA. The fraction of cells with sub-diploid DNA content was measured with flow cytometry. As shown in **Figure 7A**, treatment with increasing doses of unlabeled immunotoxin resulted in dose-dependent increases in the S phase population with concomitant decreases in the G2 phase population of LNCaP cells. However, this effect of the immunotoxin was not evident in PC-3 cells. Similarly, trypan blue dye staining showed significantly increased staining of nonviable cells in LNCaP cultures, but not in PC-3 cell cultures treated with the immunotoxin. The 48 hours DNA content frequency histogram was similar to 24 h histogram and shown in **FigureS3**. Light microscopy also showed higher rates of apoptosis in LNCaP cells after incubation with increasing amounts of A-dmDT390-scfbDb(PSMA) (**Figure 7B**). Fluorescence microscopy showed an increase of green fluorescence signal on the cell membrane due to apoptosis (FITC-labeled annexin V antibody bound with apoptotic cells) when the concentration of the immunotoxin was increased from 0.1 nM to 1 nM. The red fluorescence signal increased (due to DNA binding to PI in necrotic cells) when cells were treated with increased dose of immunotoxin, *i.e.*, from 5 nM and 10 nM immunotoxin (**Figure 7B**).

Diphtheria toxin exerts its toxicity towards eukaryotic organisms through inactivation of the polypeptide chain EF-2 (Elongation Factor 2). The inactivation results in inhibition of protein synthesis and induction of apoptosis [25]. As a truncated form of diphtheria toxin, DT390, is widely known for inducing cellular toxicity through targeted delivery *via* a ligand component. The immunotoxins constructed with DT390 are reported to have high toxicity to activated T cells.[14,26] However, little is known about the process of targeted cell apoptosis induced by DT390 in tumor cells. In this study, the immunotoxin of A-dmDT390-scfbDb(PSMA) efficiently induced apoptosis in PSMA-positive LNCaP cells. Flow cytometry analysis of the cell cycle parameters showed that the immunotoxin caused an increase in S phase population and a decrease in G2 phase population in LNCaP cell cultures. These may have some implications for the cytotoxicity of the immunotoxin *in vitro*.

2.5. A-dmDT390-scfbDb(PSMA) targets LNCaP but not PC-3 solid tumor xenografts in live mice.

LNCaP cells and PC-3 cells were implanted on the lower left flank of athymic nude mice to test the targeting efficiency of A-dmDT390-scfbDb(PSMA) in prostate tumors. The tumor was allowed to grow to about 5 mm in diameter. One hundred microliters (200 µg/mL) of Alexa Fluor 680 dye labeled A-dmDT390-scfbDb(PSMA) or Alexa Fluor 680 dye alone was administered as a single bolus *via* tail vein injection. The whole animal was then imaged at different time points after injection. In this study, near infrared fluorescent imaging was used to confirm the tumor targeting effectiveness of the immunotoxin in LNCaP tumors. Optical imaging provides a dynamic, noninvasive real-time *in vivo* imaging technique for monitoring the uptake of fluorescent probes in tumor-bearing animals. This optical approach can be used to monitor gene delivery and drug accumulation in tumors.[27-29] As shown in **Figure 8**, accumulation of the fluorescence signal from the labeled immunotoxin was detectable in LNCaP tumors as early as 30 minutes after injection. The fluorescent signal in LNCaP tumors showed an increase during the first 6 hours after injection, followed by a

gradual decrease (**Figure 8A**). The signal from the free Alexa Fluor 680 dye was rapidly detectable throughout the whole body. However, no obvious accumulation of the Alexa Fluor 680 dye was observed in the tumors (**Figure 8B**). In PC-3 tumor models, both Alexa Fluor 680 labeled A-dmDT390-scfbDb(PSMA) and Alexa Fluor 680 dye showed increased fluorescent signals throughout the whole body during the first 8 hours after injection. However, the fluorescent signal showed no obvious targeting to and accumulation in the tumors **(Figure S4)**.

2.6. A-dmDT390-scfbDb(PSMA) inhibits LNCaP tumor growth

The tumor-specific inhibitory effect of A-dmDT390-scfbDb(PSMA) was studied on the PSMA-positive LNCaP tumors and the PSMA-negative PC-3 tumors grown as solid tumor xenografts in athymic nude mice. Each mouse was given 10 μg A-dmDT390-scfbDb(PSMA) *via* intraperitoneal injection for six consecutive days. A-dmDT390-scfbDb(PSMA) significantly inhibited LNCaP tumor growth while not affecting PC-3 tumor growth **(Figure 9A and B, Figure 10)**. At the end of treatment, the tumors were surgically removed and weighed. The average LNCaP tumor weight in the treatment group was 0.27 ± 0.09 g, which was significantly lower than the tumor weight in the untreated control group $(0.67 \pm 0.11$ g) ($P < 0.05$, **Figure 9C**). The average weight of the treated PC-3 tumors was not significantly different from the average weight of untreated PC-3 tumors in the control group ($P > 0.05$, **Figure 9C**). There was no difference for the body weights between the LNCaP tumor-bearing mice and PC-3 tumor-bearing mice, whether or not the animals were treated with the immunotoxin ($P > 0.05$).

Figure 8 shows rapid accumulation of A-dmDT390-scfbDb(PSMA) immunotoxin in LNCaP tumors, whereas no fluorescent signal was detected in PC-3 tumors. High intensity of fluorescent signals from Alexa Fluor 680 labeled A-dmDT390-scfbDb(PSMA) immunotoxin was also observed in the kidneys, suggesting that the immunotoxin or degraded fragments might be excreted through the kidneys. The selective cytotoxicity of A-dmDT390-

scfbDb(PSMA) immunotoxin both *in vitro* (**Figure 3**) and *in vivo* (**Figure 9**) suggests that the immunotoxin can selectively bind to, and be internalized into PSMA-expressing cells. This specific targeting *in vivo* may be responsible for the inhibitory effect of A-dmDT390-scfbDb(PSMA) on the PSMA-positive LNCaP tumor growth, but not on the PSMA-negative PC-3 tumor growth. The findings suggest that this immunotoxin construct has considerable promise and potential for prostate cancer treatment.

Immunotoxins generated by full length of anti-PSMA monoclonal antibody [30,31] or its scFv [32] exhibit specific cytotoxicity and capability to inhibit PSMA-positive prostate tumor growth. However, there are few clinical trials evaluating the clinical potential of immunotoxins linked to PSMA antibody. An important finding of this study was the efficacy of the A-dmDT390-scfbDb(PSMA) immunotoxin against PSMA-positive prostate cancer cells and the lack of binding and cytotoxic effect against PSMA-negative prostate cancer cells. This suggests that inappropriate use of this immunotoxin for treating PSMA-negative tumors may run the risk of unintended systemic toxicity. It is imperative to confirm the presence of PSMA on the tumor cells before initiating therapy with the immunotoxin used in our studies because some prostate cancers do not express PSMA.

3. Conclusion

The A-dmDT90(390)-scfbDb(PSMA) immunotoxin used in this study selectively accumulates in LNCaP cells and tumors, which overexpress PSMA. As a consequence of this uptake, LNCaP cells underwent S phase arrest and apoptosis. Intraperitoneal injection of the immunotoxin caused regression of LNCaP solid tumor xenografts in nude mice. Such accumulation and therapeutic response was not seen in PC3 cells and xenografts. This is due to the fact that PC3 cells and tumors are deficient in PSMA expression. Optical imaging experiments confirmed efficient targeted uptake of NIR labeled immunotoxin by PSMA expressing LNCaP cells and solid tumor xenografts in nude mice.

Our study showed that the use of this immunotoxin might be beneficial to individuals with a PSMA-positive prostate tumor. Optical imaging on the individual patient may be processed to determine the expression of PSMA and monitor the efficacy of immunotoxin therapy using the methods described in this paper. This approach will enable us to identify patients who are likely to benefit from treatment with A-dmDT390-scfbDb(PSMA). The fluorescently labeled immunotoxin is potentially useful for targeted theranostics and personalized medicine.

4. Experimental Section

Cell Lines: Human prostate cancer cell lines LNCaP and PC-3 were purchased from ATCC (American Type Culture Collection, Manassas, VA). LNCaP and PC-3 cells were maintained as exponentially growing monolayer cultures in RPMI 1640 medium and DMEM, respectively. Both media were supplemented with L-glutamine (2 mM), 50 μg/ml each of penicillin and streptomycin, and 10% heat-inactivated fetal bovine serum. The cells were maintained in culture at 37 °C with 5% CO_2 in air and 95% humidity.

Expression and Purification of A-dmDT390-scfbDb(PSMA) Protein: A-dmDT390-scfbDb(PSMA) was expressed in a DT-resistant *Pichia pastoris* strain. The immunotoxin was produced in shake flask culture and purified by three purification steps, Phenyl Sepharose hydrophobic interaction chromatography, Q Sepharose anion exchange chromatography and Superdex 200 gel filtration chromatography [20].

Cellular PSMA Staining: LNCaP and PC-3 cells were plated in 8-well chamber slides with $1×10^4$ cells in 0.5 ml medium in each well. After 24 hours, cells were washed with Dulbecco's phosphate-buffered saline (DPBS) and fixed in 3.7% paraformaldehyde. The cells were permeabilized with 0.2% Triton-X 100 and blocked with 1% bovine serum albumin (BSA) in Hank's buffered salt solution (HBSS) for 1 hour. The cells were then incubated with a rabbit monoclonal anti-PSMA antibody (Abcam, Cambridge, MA) at a dilution of 1:200 to a final concentration of 1 μg/ml. After washing the cells with HBSS, goat anti-rabbit

immunoglobulin G conjugated with Alexa Fluor 680 (Invitrogen, Carlsbad, CA) was added to the blocking solution at a final concentration of 2 μg/ml and incubated at room temperature for 1 hour in the dark. The slides were washed three times with DPBS, and examined with a fluorescence microscope.

Western Blot Analysis: LNCaP and PC3 cells were washed with DPBS and lysed with RIPA lysis and extraction buffer (Pierce Biotech, Rockford, IL). Protein concentrations were determined with the Bio-Rad Protein Assay Dye Reagent Concentrate (Bio-Rad, Hercules, CA). Fifty micrograms of proteins were separated by 8% SDS-PAGE electrophoresis and transferred to PVDF membranes. The membranes were blocked using 5% nonfat milk and probed separately for 2 hours at room temperature with primary antibodies for PSMA (Abcam) and β-Actin (Santa Cruz Biotechnology, Santa Cruz, CA). The membranes were then washed and probed with a 1:2,000 dilution of peroxidase-conjugated secondary antibody, and detected with enhanced chemiluminescence (Amersham Life Sciences, Amersham, UK).

Cell Viability Assays: Cells were seeded in 96-well plates and cultured for 24 hours. The cells were then exposed to a graded range of concentrations (from 0 nM to 5 nM) of A-dmDT390-scfbDb(PSMA) for 48 hours. The viability of cells was measured with MTT assay. One hundred microliters of MTT solution (0.5 mg/ml in PBS) were added to each well. The plates were incubated for 4 hours at 37 °C, and then 100 μl of dimethyl sulfoxide was added to each well and incubated for 10 minutes at room temperature. The absorbance was measured at 570 nm using a plate reader. The half maximal inhibitory concentration (IC_{50}) of the immunotoxin was calculated using the SPSS software for performing statistical analysis.

Endocytosis and Quantification of A-dmDT390-scfbDb(PSMA) in Cells: A-dmDT390-scfbDb(PSMA) was labeled with Alexa Fluor 680 using Invitrogen Protein Labeling Kit A20172. LNCaP and PC-3 prostate cancer cells grown to 60 to 70% confluence on four-chamber glass slides were used for endocytosis analysis. The cells were incubated with 0.1

µM of Alexa Fluor 680-labeled A-dmDT390-scfbDb(PSMA) in complete medium for different durations (from 10 minutes to 3 hours), or incubated with graded concentrations (from 0.01 µM to 0.1 µM) of Alexa Fluor 680–labeled A-dmDT390-scfbDb(PSMA) for 3 hours. After removal of the media, the cells were washed three times using DPBS, fixed with 10% formalin for 10 minutes, stained with 4',6-diamidino-2-phenylindole (DAPI) for 5 minutes, and rinsed three times with DPBS. The cells were then observed under fluorescent microscopy. For quantitative measurement of the Alexa Fluor 680-labeled A-dmDT390-scfbDb(PSMA) internalization, a BD flow cytometer (Becton Dickinson, San Jose, CA) with excitation/emission: 635 nm/679 nm was used.

Assessment of Apoptosis: Annexin V binding was used to estimate apoptosis. Cells were first exposed to a DNA-binding dye (PI) to detect sub-diploid population. The two prostate cancer cell lines (LNCaP and PC-3) were treated with 0.1, 0.5, and 1.0 nM of A-dmDT390-scfbDb(PSMA) immunotoxin for 24 hours, respectively. Then the cells were harvested with trypsinization, collected by centrifugation, and washed with DPBS. The collected cells were fixed with 70% ethanol for 1 hour at 4 °C. The fixed cells were washed twice in DPBS, incubated with a solution containing 100 µg/mL RNase at 37 °C in a water bath for 30 minutes, and then gently re-suspended in 1 mL of PI solution (50 µg/mL with 3.8 mM sodium citrate in DPBS). Lastly, the cells were incubated for 15 minutes in the dark at room temperature and analyzed using flow cytometry. The red fluorescence signal from PI staining of individual cells was collected. Ten thousand cells of each sample were counted. For fluorescence microscopy detection, 10,000 LNCaP cells were plated onto an 8-well chamber slide for 24 hours. After incubation with different concentrations of A-dmDT390-scfbDb(PSMA) for 48 hours, the cells were incubated with 500 µl of Annexin binding buffer. Five microliters of Annexin V-FITC and 5 µl of PI (Abcam) were added onto the cells, and cells were fixed in 2% formaldehyde before visualization. The fixed cells were examined

under a fluorescence microscope using separate filters for FITC and PI. The cells that bound Annexin V-FITC, which had undergone apoptosis, showed green staining on the plasma membrane, whereas the cells that had lost membrane integrity due to necrosis showed red PI staining throughout the nuclei. To further determine the cytotoxicity of A-dmDT390-scfbDb(PSMA), the cells were routinely examined using trypan blue staining and under light microscopy. The cells permeable to trypan blue were considered nonviable.

Animal Tumor Model and Optical Imaging: All animal studies were carried out in accordance with the guidelines of the Howard University Institutional Animal Care and Use Committee. Five-week-old athymic male nude mice were inoculated subcutaneously with 5×10^6 LNCaP cells or 2×10^6 PC-3 cells mixed with 0.2 ml of matrigel (BD Biosciences, Bedford, MA) into the lower left flank. The tumors were allowed to reach 5-7 mm in diameter for imaging study. Six mice with LNCaP tumors and five mice with PC-3 tumors were used to test the detection sensitivity and specificity of imaging and the dynamic uptake of Alexa Fluor 680–labeled A-dmDT390-scfbDb(PSMA) *in vivo*. Three mice with LNCaP tumors and three mice with PC-3 tumors were used to test specific targeting of tumor by Alexa Fluor 680 labeled A-dmDT390-scfbDb(PSMA). Three mice with LNCaP tumors and two mice with PC-3 tumors were given an identical volume of DPBS and served as controls.

  In vivo fluorescence imaging of tumor-bearing mice was performed using the IVIS 200 Imaging System and Living Image software (Caliper Life Sciences, Hopkinton, MA). The mice were placed on a warmed (25 °C) stage inside a light-tight camera box with continuous exposure to 2% isoflurane. The mice were given 100 μL (200 μg/mL; 2.06 μM) of the Alexa Fluor 680 labeled A-dmDT390-scfbDb(PSMA) or 100 μL (4.12 μM; one molecule A-dmDT390-scfbDb(PSMA) labeled with two molecules of Alexa Fluor 680 dye) or Alexa Fluor 680 dye *via* tail vein injection. The mouse was imaged every 10 minutes for the first hour and then imaged every hour for 24 hours. The acquisition time for each image was 2

seconds. Regions of interest around tumor sites from the displayed images were identified and emitted light was measured. The signal intensity was expressed as radiant efficiency in photons/second/cm^2/steradian/$\{\mu W/cm^2\}$ (p/s/cm^2/sr$\{\mu W/cm^2\}$). The contralateral non-tumor-bearing leg muscle was selected as the background.

Evaluation of Therapeutic Efficacy: Tumor xenograft models were developed by subcutaneous inoculation of 5×10^6 LNCaP cells or 2×10^6 PC-3 cells mixed with 0.2 ml of matrigel into the lower left flank of five-week-old male athymic nude mice. LNCaP tumors were allowed to develop for six weeks and PC-3 tumors for three weeks to reach the diameter of about 5 mm. The mice with LNCaP tumors or PC-3 tumors were divided randomly into two groups (*n* = 10). A-dmDT390-scfbDb(PSMA) immunotoxin (200 ug/kg) or BSA diluted in DPBS was administered *via* intraperitoneal injection to twice a day at 6 hour intervals (10 am and 4 pm) for 6 days. Tumor growth was monitored twice a week with MRI. The mice were anesthetized with 2% isoflurane in oxygen, positioned in the MRI probe, and taped with polyurethane foam to avoid involuntary motion. A Bruker 400MHz NMR machine (Bruker-Biospin, Billerica, MA) was used for MRI. A rapid acquisition with refocused echoes (RARE) sequence was used to acquire T2-weighted coronal images. The imaging parameters were: TE 7.8 ms, RARE factor 16, effective TE 39 ms, TR 3600 ms, number of averages 12, field-of-view 27.0 mm × 25.6 mm, matrix size 192 × 256, and slice thickness 0.5 mm. The MIPAV software (CIT/NIH, Bethesda, MD) was used for image analysis. The tumor was manually segmented in each MRI image, the number of voxels within the boundary of tumor was counted and the total tumor volume was calculated.

Statistical Analysis: Statistical analysis was performed with the Student's *t*-test. Survival was assessed with the Kaplan – Meier method. A significant correlation was inferred if a *P* value was < 0.05 by correlation analysis. All statistical tests were two-sided.

References

[1] A. Jemal, R. Siegel, E. Ward, Y. Hao, J. Xu, T. Murray, M. J. Thun, *CA Cancer J. Clin.* **2008**, 58, 71–96.

[2] C. N. Sternberg, *Ann. Oncol.* **2008**, 19 Suppl 7, vii91–95.

[3] L.C. Pronk, P. H. Hilkens, M. J. van den Bent, W. L. van Putten, G. Stoter, J. Verweij, *Anticancer Drugs* **1998**, 9, 759–764.

[4] T. M. Allen, *Nat. Rev. Cancer* **2002**, 2, 750–763.

[5] W. R. Fair, R. S. Israeli, W. D. Heston. *Prostate* **1997,** 32, 140–148.

[6] S. F. Slovin, *Expert. Opin. Ther. Targets* **2005,** 9, 561–570.

[7] S. S. Chang, D. S. O'Keefe, D. J. Bacich, V. E. Reuter, W. D. Heston, P. B. Gaudin, *Clin. Cancer Res.* **1999**, 5, 2674–2681.

[8] C. A. Foss, R. C. Mease, H. Fan, Y. Wang, H. T. Ravert, R. F. Dannals, R. T. Olszewski, W. D. Heston, A. P. Kozikowski, M. G. Pomper, *Clin. Cancer Res.* **2005**, 11, 4022–4028.

[9] G. Fracasso, G. Bellisola, S. Cingarlini, D. Castelletti, T. Prayer-Galetti, F. Pagano, G. Tridente, M. Colombatti, *Prostate* **2002,** 53, 9–23.

[10] N. Schulke, O. A. Varlamova, G. P. Donovan, D. Ma, J. P. Gardner, D. M. Morrissey, R. R. Arrigale, C. Zhan, A. J. Chodera, K. G. Surowitz, P. J. Maddon, W. D. Heston, W. C. Olson, *Proc. Natl. Acad. Sci. USA* **2003**, 100, 12590–12595.

[11] A. M. Wu, P. D. Senter, *Nat. Biotechnol.* **2005,** 23, 1137–1146.

[12] N. Arora, R. Masood, T. Zheng , J. Cai, D. L. Smith, P. S. Gill, *Cancer Res.* **1999**, 59, 183-188.

[13] Y. Y. Liu, I. Gordienko, A. Mathias, S. Ma, J. Thompson, J. H. Woo, D. M. Neville, *Protein Expr. Purif.* **2000**,19, 304–311.

[14] Y. Jia, H. Li, W. Chen, M. Li, M. Lv, P. Feng, H. Hu, L. Zhang, *Gene Therapy.* **2006**,13,1351–1359.

[15] C. H. Chan, B. R. Blazar, L. Greenfield, R. J. Kreitman, D. A. Vallera, *Blood* **1996**, 88, 1445-1456.

[16] Z. Wang, G. B. Kim, J. H. Woo, Y. Y. Liu, A. Mathias, S. Stavrou, D. M. Neville, *Bioconjug Chem.* **2007**, 18, 947-955.

[17] J. H. Woo, S. H. Bour, T. Dang, Y. J. Lee, S. K. Park, E. Andreas, S. H. Kang, J. S. Liu, D. M. Jr. Neville, A. E. Frankel, *Cancer Immunol. Immunother.* **2008**, 57, 1225-1239.

[18] J. H. Woo , Y. J. Lee, D. M. Neville, A. E. Frankel, *Methods Mol. Biol.* **2010**, 651, 157-175.

[19] G. B. Kim, Z. Wang, Y. Y. Liu, S. Stavrou, A. Mathias, K. J. Goodwin, J. M. Thomas, D. M. Neville, *Protein Eng. Des. Sel.* **2007**, 20, 425-432.

[20] D. M. Neville, J. T. Thompson, H. Hu, J. H. Woo, S. Ma, J. M. Hexham, M. E. Digan. **July 2012**, US Patent Number 8217158.

[21] C. Liu, K. Hasegawa, S. J. Russell, M. Sadelain, K. W. Peng, *Prostate.* **2009**, 69, 1128-1141.

[22] K. Fortmüller, K. Alt, D. Gierschner, P. Wolf, V. Baum, N. Freudenberg, U. Wetterauer, U. Elsässer-Beile, P. Bühler, *Prostate.* **2011**, 71, 588-596.

[23] D. M. Nanus, M. I. Milowsky, L. Kostakoglu, P. M. Smith-Jones, S. Vallabahajosula, S.

J. Goldsmith, N. H. Bander, *J. Urol.* **2003**, 170(6 Pt 2), S84–88.

[24] W. C. Olson, W. D. Heston, A. K. Rajasekaran, *Rev. Recent Clin. Trials* **2007**, 2,182–190.

[25] S. K. Kochi, R. J. Collier, *Exp. Cell Res.* **1993**, 208, 296-302.

[26] J. Jia, H. Li, S. Tai, M. Lv, M. Liao, Z. Yang, B. Zhang, B. Zhou, G. Zhang, L. Zhang, *DNA Cell Biol.* **2008**, 27, 279-285.

[27] M. Veiseh, P. Gabikian, S. B. Bahrami, O. Veiseh, M. Zhang, R. C. Hackman, A. C. Ravanpay, M. R. Stroud, Y. Kusuma, S. J. Hansen, D. Kwok, N. M. Munoz, R. W. Sze, W. M. Grady, N. M. Greenberg, R. G. Ellenbogen, J. M. Olson, *Cancer Res.* **2007,** 67, 6882–6888.

[28] E. L. Kaijzel, G. van der Pluijm, C. W. Lowik, *Clin. Cancer Res.* **2007**. 13, 3490–3497.

[29] J. Thompson, S. Stavrou, M. Weetall, J. M. Hexham, M.E. Digan, Z. Wang, J. H. Woo, Y. Yu, A. Mathias, Y. Y. Liu, S. Ma, I. Gordienko, P. Lake, D.M. Neville Jr., *Protein Eng.* **2001**, 14, 1035-1041.

[30] D. Ma, C. E. Hopf, A. D. Malewicz, G. P. Donovan, P. D. Senter, W. F. Goeckeler, P. J. Maddon, W. C. Olson. Clin. Cancer Res. 2006, 12, 2591-2596.

[31] K. Kuroda, H. Liu, S. Kim, M. Guo, V. Navarro, N. H. Bander. Prostate. 2010, 70, 1286-1294.

[32] P. Wolf , K. Alt , D. Wetterauer , P. Bühler, D. Gierschner, A. Katzenwadel, U. Wetterauer , U. Elsässer-Beile. J Immunother. 2010, 33, 262-271.
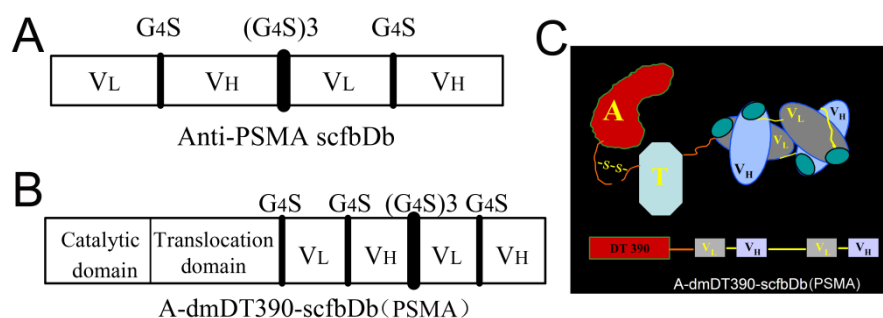
Figure 1. The scheme of A-dmDT390-scfbDb comprising the A-dmDT390 moiety and the anti-PSMA scfbDb. (A): The diabody consists of two scFv fragments separated by optimized lengths of Gly-Ser linkers. (B): The immunotoxin comprises the A-dmDT390 moiety and the anti-PSMA scfbDb. The sequence from left to right is dmDT- VL-L1-VH-L2-VL-L1-VH. G4S are linkers, and VL and VH are the variable domains of light and heavy chains, respectively; A-dmDT390 is the first 390 amino acid residues of diphtheria toxin with an addition of alanine to the N-terminus and two mutations for de-glycosylation. (C): The cartoon structure of A-dmDT390-scfbDb(PSMA) immunotoxin.
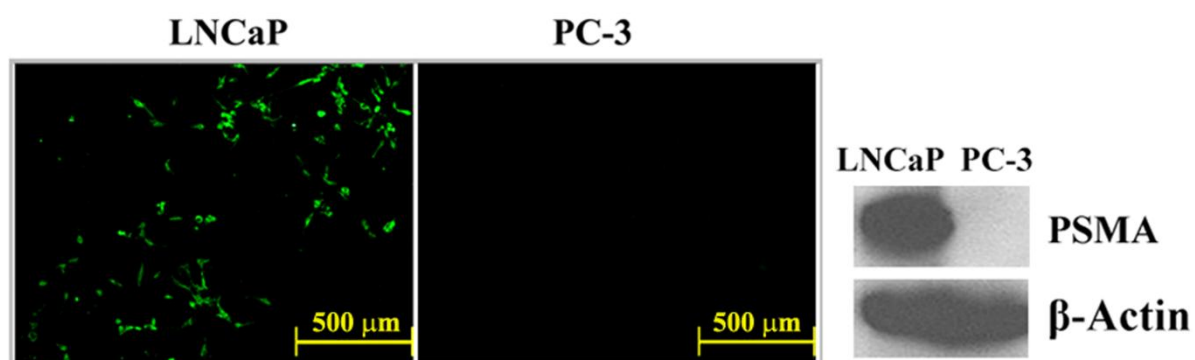
Figure 2. Expression of PSMA in prostate cancer cells. Left: LNCaP and PC-3 cells were fixed on slides, and incubated with anti-PSMA antibody and with FITC-labeled secondary antibody (green) sequentially. Right: Whole cell lysates from LNCaP and PC-3 cells were analyzed with Western blotting.
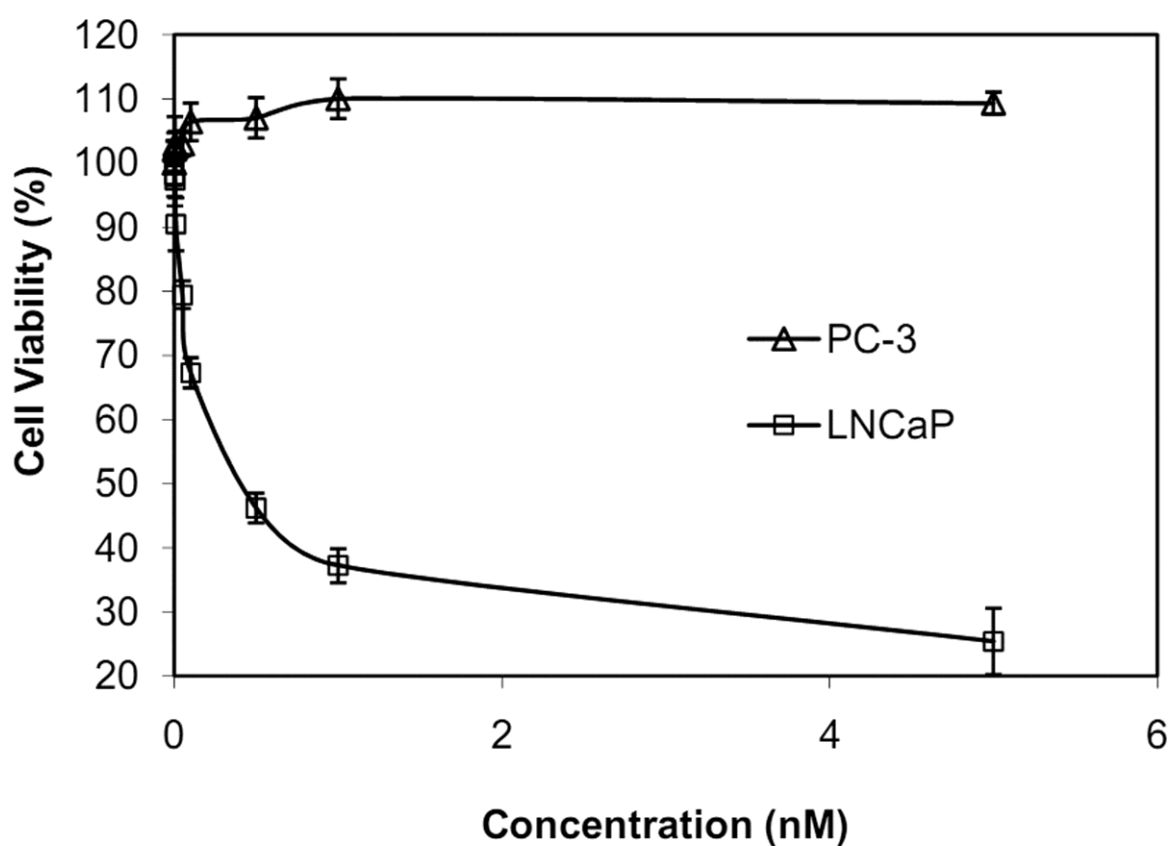
Figure 3. Cytotoxic effect of A-dmDT390-scfbDb(PSMA) on LNCaP cells and PC-3 cells. The viabilities of PSMA-positive (LNCaP) and PSMA-negative (PC-3) cells were determined with MTT assay after 48-hour treatment with A-dmDT390-scfbDb(PSMA). Data represent the mean ± SD of triplicate determinations.
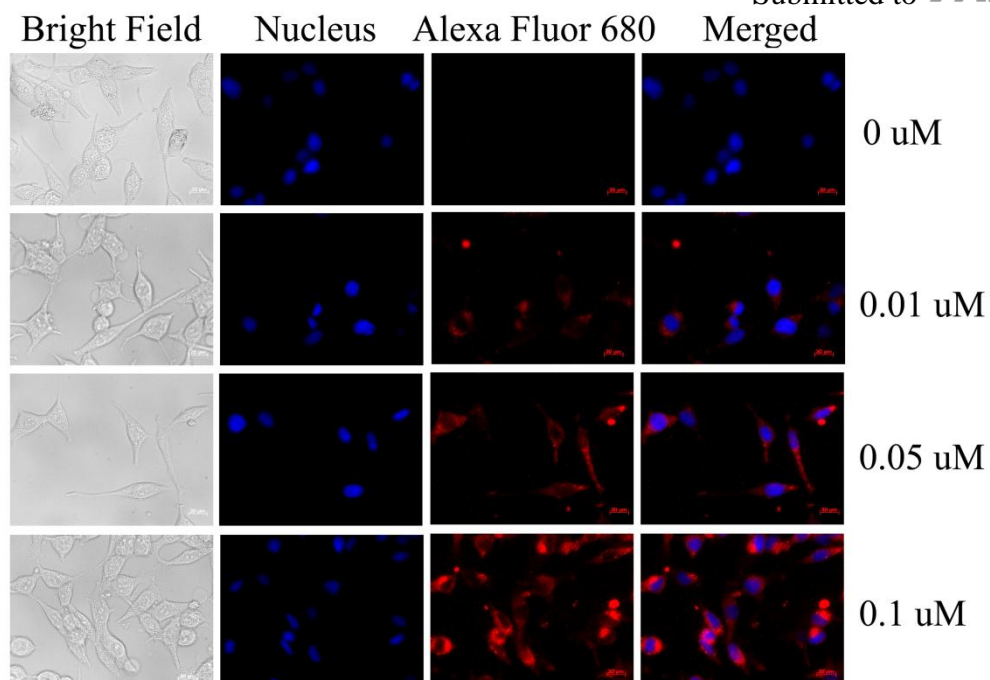
Figure 4. Fluorescence microscopy of A-dmDT390-scfbDb(PSMA) internalization in LNCaP cells. Cells were treated with 0.01, 0.05, or 0.1 µM of Alexa Fluor 680-labeled A-dmDT390-scfbDb(PSMA) for 3 hours. After washing with DPBS, cells were fixed and incubated with DAPI, and observed under a fluorescence microscope (magnification 400×).

Bright Field	Nucleus	Alexa Fluor 680	Merged	
				Control
				10 mins
				30 mins
				1 hr
				3 hrs
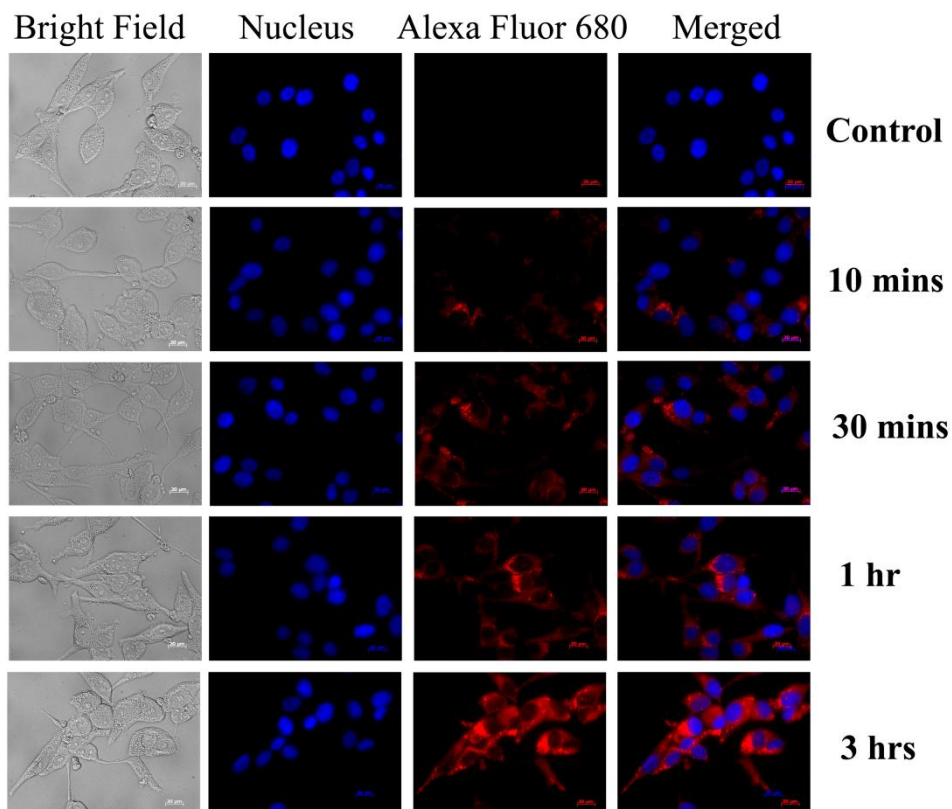
Figure 5. Fluorescence microscopy of the time course of A-dmDT390-scfbDb(PSMA) internalization in LNCaP cells. Cells were treated with 0.1 µM of Alexa Fluor 680-labeled A-dmDT390-scfbDb(PSMA) for different durations, *i.e.,* 10 min, 30 min, 1 h, and 3 h . After washing with DPBS, cells were fixed and incubated with DAPI, and observed under a fluorescence microscope (magnification 400×).
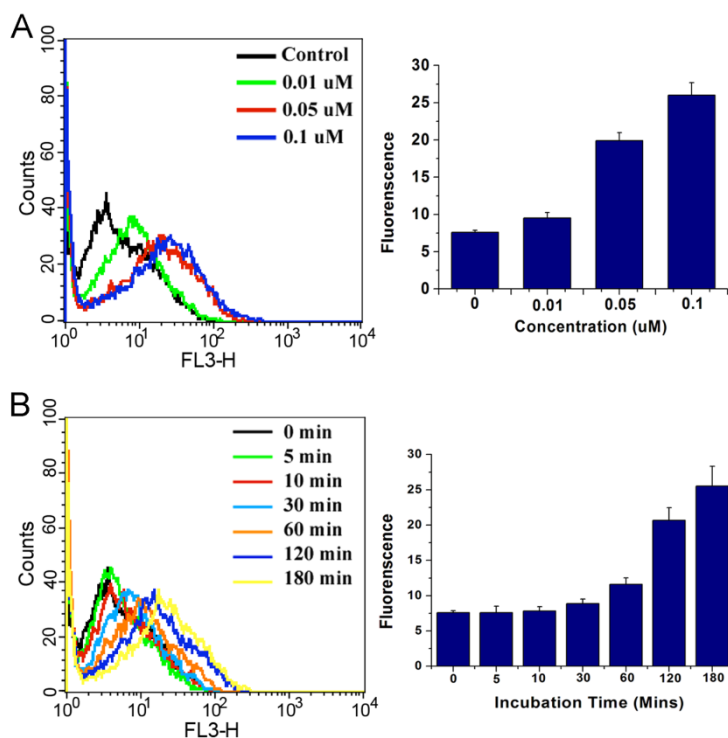
Figure 6. Flow cytometry quantification of A-dmDT390-scfbDb(PSMA) accumulation in LNCaP cells. Cells were treated with 0.01, 0.05, or 0.1 µM of Alexa Fluor 680-labeled A-dmDT390-scfbDb(PSMA) for 3 hours (A) or with 0.1 µM of Alexa Fluor 680-labeled A-dmDT390-scfbDb(PSMA) for different durations, *i.e.,* 5, 10, 30, 60, 120, and 180 min (B). After washing with DPBS, cells were collected and analyzed with flow cytometry.
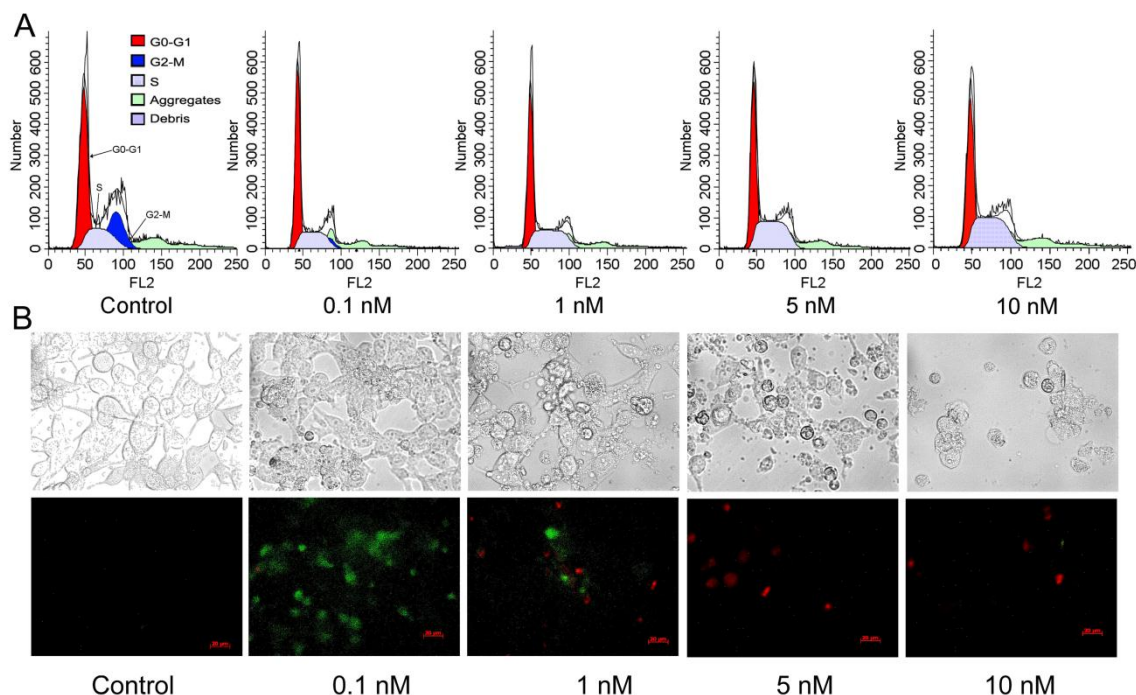
Figure 7. Cell cycle analysis and apoptosis assay of LNCaP cells after A-dmDT390-scfbDb(PSMA) treatment. (A) LNCaP cells were treated for 24 hours with 0.1, 1, 5, and 10 nM of A-dmDT390-scfbDb(PSMA), respectively, and then stained with PI. Cell cycle distribution was analyzed with flow cytometry. (B) LNCaP cells treated with 0 to 10 nM of A-dmDT390-scfbDb(PSMA) for 48 hours were stained with Annexin V-FITC antibody, washed with buffer and observed under a florescent microscope (magnification 400×).
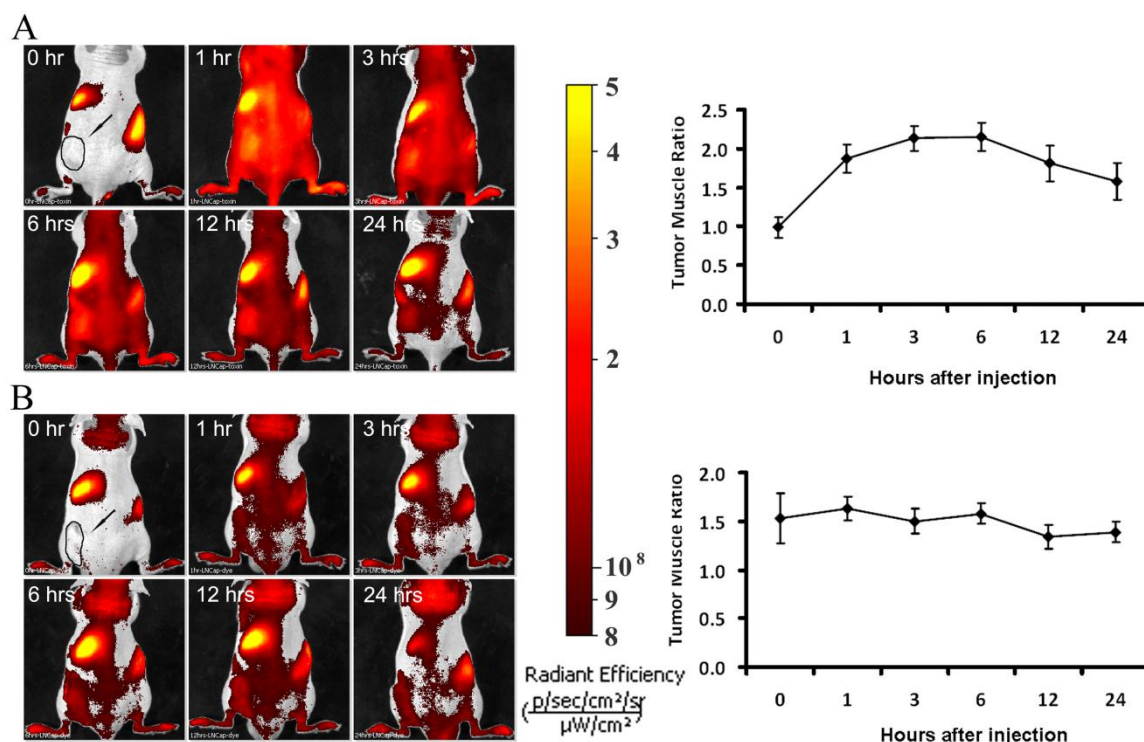
Figure 8. Animal whole body optical imaging after intravenous injection of Alexa Fluor 680-labeled A-dmDT390-scfbDb(PSMA) into LNCaP tumor-bearing mice, showing preferential accumulation of fluorescent signal in tumors. (A) Images obtained after injection of Alexa Fluor 680-labeled A-dmDT390-scfbDb(PSMA) (100 µl) into mice. (B) Images obtained at 0, 1, 3, 6, 12, and 24 hours, respectively, after injection of Alexa Fluor 680 dye alone (100 µl) into mice. The chart on the right shows the changes of the tumor (marked with arrow) to muscle ratio for the fluorescence intensity over time.
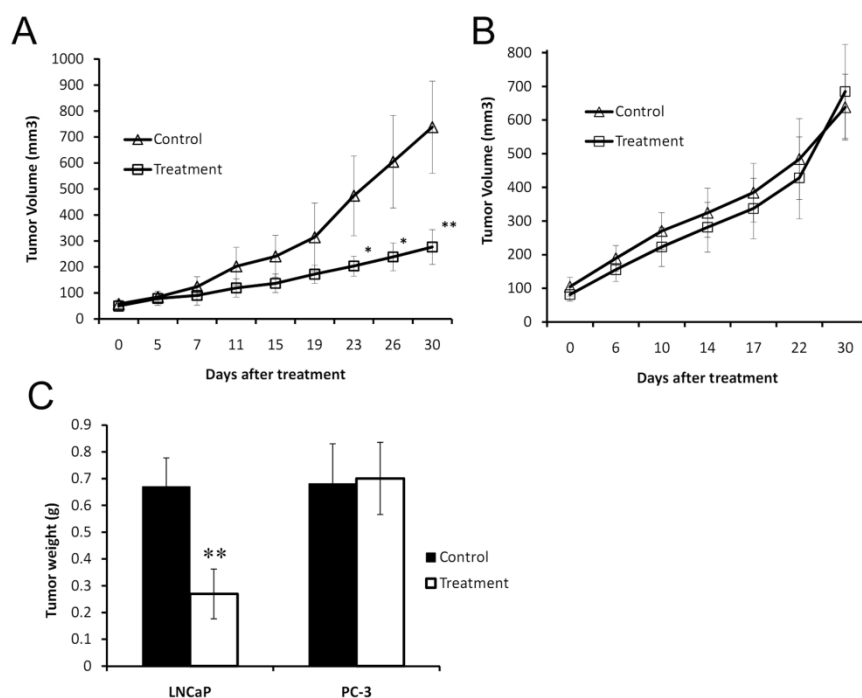
Figure 9. Effect of A-dmDT390-scfbDb(PSMA) immunotoxin on LNCaP and PC-3 prostate carcinomas. 200 µg/kg (5 µg/mice) per dose of A-dmDT390-scfbDb(PSMA) immunotoxin was given *via* intraperitoneal injection, two doses a day with 6 hour interval for 6 days, compared to equivalent dose of BSA diluted in DPBS for control mice ($n = 10$ mice per group, *$P < 0.1$, **$P < 0.01$). (A) LNCaP tumor volume measurement with MRI. (B) PC-3 tumor volume measurement with MRI. (C) Tumor weight after treatment for 30 days.
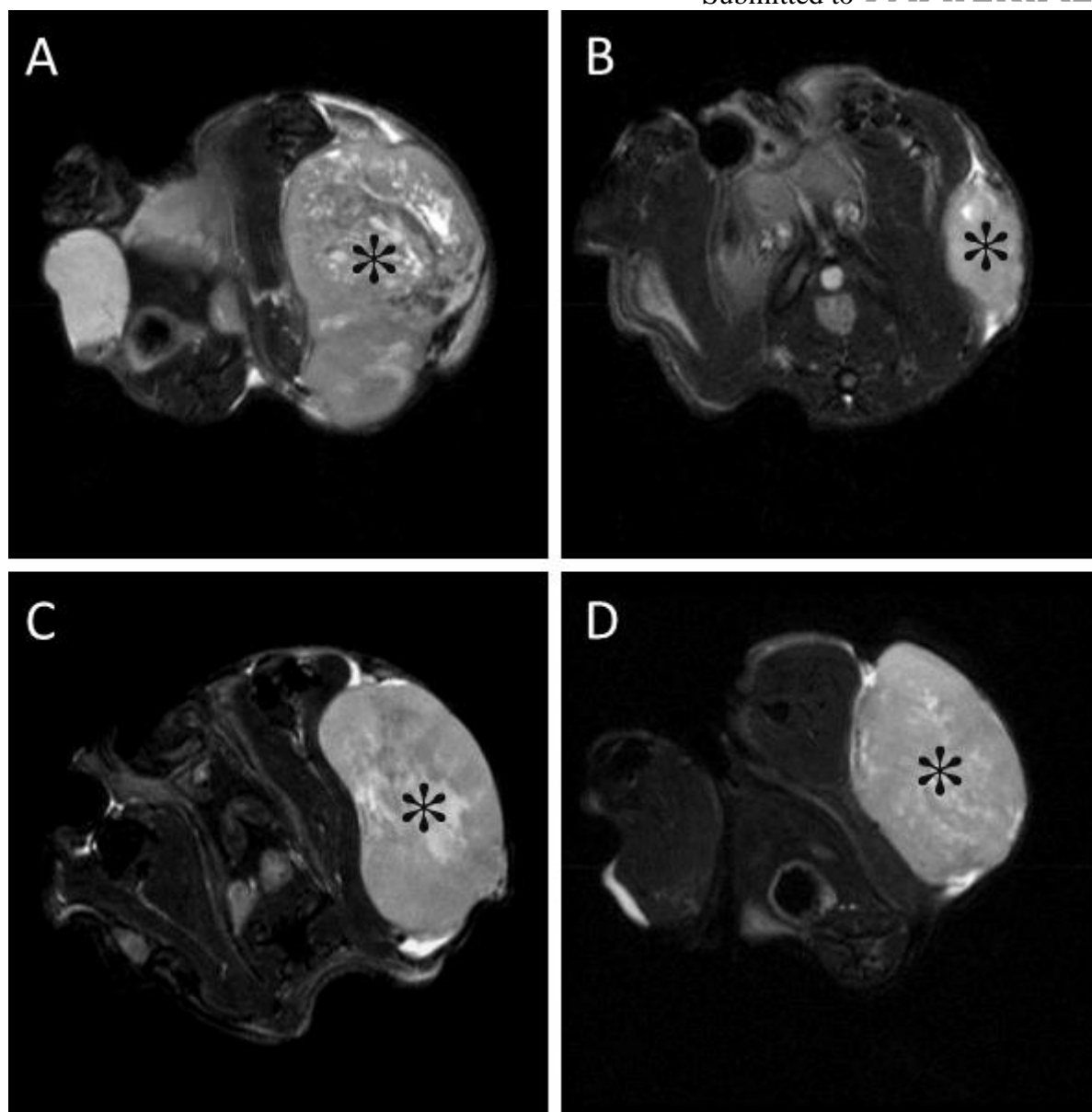
Figure 10. MR images showing the effects of A-dmDT390-scfbDb(PSMA) immunotoxin on LNCaP and PC-3 prostate tumors (marked with *). (A) and (B) are representative MR images through the largest cross section of an untreated control and a treated LNCaP tumor in mice 30 days after treatment. (C) and (D) are MR images of an untreated control and a treated PC-3 tumor.

Table of Contents

An immunotoxin produced is effective for targeted killing and selective imaging of PSMA

expressing prostate cancer cells grown in vitro and in vivo. This immunotoxin is without

effect on prostate cancer cells that are deficient in PSMA expression and may find theranostic

use in the clinic for selectively treating tumors that overexpress PSMA.

TOC Keyword: Diphtheria toxin DT390; Immunotoxin; Prostate-specific membrane antigen; Targeted drug delivery; Tumor imaging

Authors: F. Zhang, L. Shan, Y. Liu, D. Neville, J-H Wu, Y. Chen, A. Korotcov, S. Lin, S. Huang, R. Sridhar, W. Liang, P. C. Wang*

Title: An Anti-PSMA Bivalent Immunotoxin Exhibits Specificity and Efficacy for Prostate Cancer Imaging and Therapy

ToC Figure:
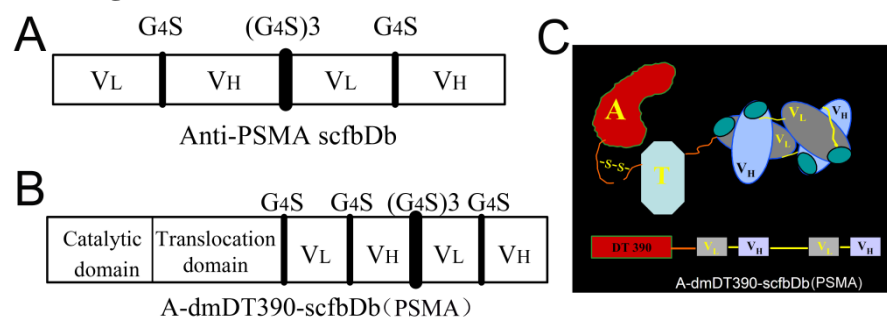
Page Headings
Left page: F Zhang et al.
Right page: Anti-PSMA Immunotoxin for Prostate Cancer Imaging and Therapy

Supporting Information

Title: An Anti-PSMA Bivalent Immunotoxin Exhibits Specificity and Efficacy for Prostate Cancer Imaging and Therapy

Authors: F. Zhang, L. Shan, Y. Liu, D. Neville, J-H Wu, Y. Chen, A. Korotcov, S. Lin, S. Huang, R. Sridhar, W. Liang, P. C. Wang*

Supporting Information
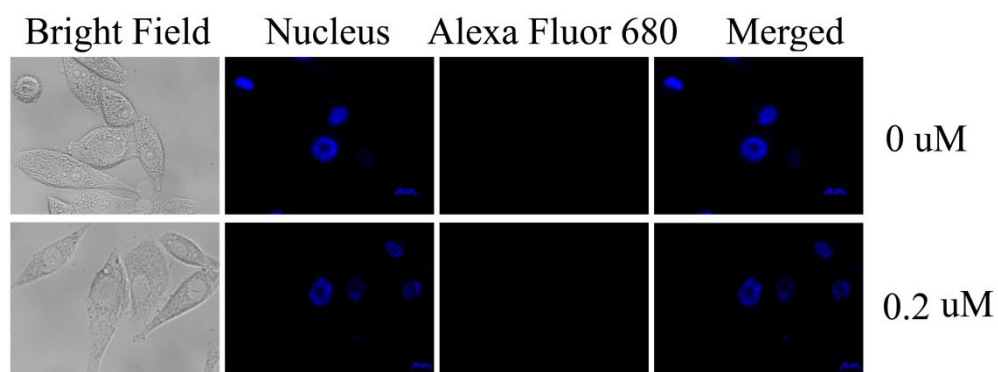
Figure S1. Fluorescence microscopy of A-dmDT390-scfbDb(PSMA) internalization in PC-3 cells. Cells were treated with 0.2 µM of Alexa Fluor 680-labeled A-dmDT390-scfbDb(PSMA) for 4 hours. After washing with DPBS, cells were fixed, incubated with DAPI, and observed under a fluorescence microscope (magnification 1000×).
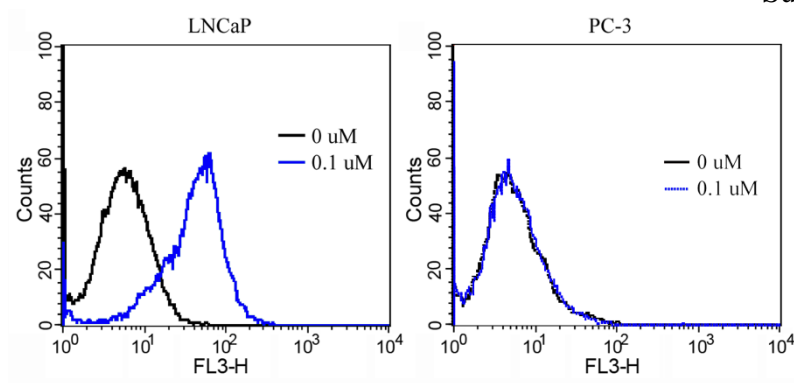
Figure S2. Flow cytometry quantification of A-dmDT390-scfbDb(PSMA) accumulation in PC-3 and LNCaP cells. Cells were treated with 0.1 µM of Alexa Fluor 680-labeled A-dmDT390-scfbDb(PSMA) for 6 hours. After washing with DPBS, cells were collected and analyzed with flow cytometry.
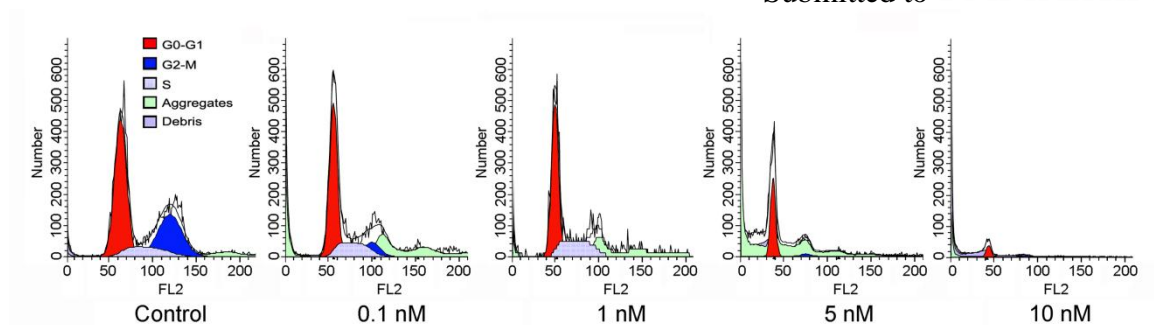
Figure S3. Cell cycle analysis of LNCaP cells after 48 hours treatment with 0.1, 1, 5, and 10 nM of A-dmDT390-scfbDb(PSMA), and then stained with PI. Cell cycle distribution was analyzed with flow cytometry.
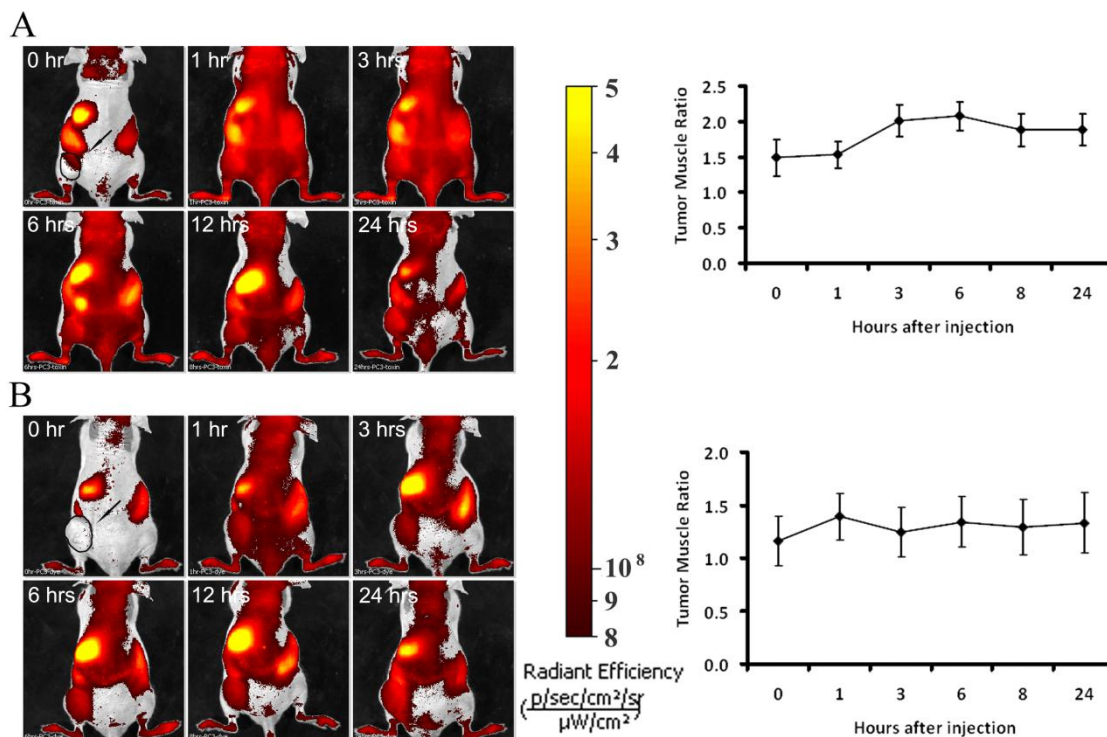
Figure S4. Whole animal imaging after intravenous injection of Alexa Fluor 680–labeled A-dmDT390-scfbDb(PSMA) into PC-3 tumor-bearing mice. (A) Images were acquired after injection of Alexa Fluor 680-labeled A-dmDT390-scfbDb(PSMA) (100 µl) into mice. (B) Images were acquired after injection of Alexa Fluor 680 dye (100 µl) into mice. Images were taken at 0, 1, 3, 6, 8, and 24 hours after injection, respectively. The chart on the right shows the changes in the ratio of tumor (marked with arrow) to muscle fluorescence intensity over time.

Gadolinium metallofullerenol nanoparticles inhibit cancer metastasis through matrix metalloproteinase inhibition: imprisoning instead of poisoning cancer cells

Huan Meng, PhD[a,1], Gengmei Xing, PhD[a,1], Elvin Blanco, PhD[b], Yan Song, BS[a], Lina Zhao, PhD[a], Baoyun Sun, PhD[a], Xiaoda Li, MS[a], Paul C. Wang, PhD[c], Alexandru Korotcov, PhD[c], Wei Li, PhD[a], Xing-Jie Liang, PhD[a], Chunying Chen, PhD[a], Hui Yuan, MS[a], Feng Zhao, MS[a], Zhen Chen, PhD[a], Tong Sun, MS[b], Zhifang Chai, PhD[a], Mauro Ferrari, PhD[b], Yuliang Zhao, PhD[a,d,*]

[a]CAS Key Laboratory for Biomedical Effects of Nanomaterials & Nanosafety, Institute of High Energy Physics, Chinese Academy of Sciences (CAS), Beijing 100049, and National Center for Nanosciences and Technology of China, Beijing China
[b]Department of Nanomedicine, The Methodist Hospital Research Institute, Houston, Texas, USA
[c]Laboratory of Molecular Imaging, Department of Radiology, Howard University, Washington, DC, USA
[d]Research Center for Cancer Nanotechnology, Tianjin Cancer Hospital and Chinese Academy of Sciences, Tianjin, China

Received 10 May 2011; accepted 28 August 2011

Abstract

The purpose of this work is to study the antimetastasis activity of gadolinium metallofullerenol nanoparticles (f-NPs) in malignant and invasive human breast cancer models. We demonstrated that f-NPs inhibited the production of matrix metalloproteinase (MMP) enzymes and further interfered with the invasiveness of cancer cells in tissue culture condition. In the tissue invasion animal model, the invasive primary tumor treated with f-NPs showed significantly less metastasis to the ectopic site along with the decreased MMP expression. In the same animal model, we observed the formation of a fibrous cage that may serve as a physical barrier capable of cancer tissue encapsulation that cuts the communication between cancer- and tumor-associated macrophages, which produce MMP enzymes. In another animal model, the blood transfer model, f-NPs potently suppressed the establishment of tumor foci in lung. Based on these data, we conclude that f-NPs have antimetastasis effects and speculate that utilization of f-NPs may provide a new strategy for the treatment of tumor metastasis.

From the Clinical Editor: In this study utilizing metallofullerenol nanoparticles, the authors demonstrate antimetastasis effects and speculate that utilization of these nanoparticles may provide a new strategy in metastatic tumor therapy.
© 2012 Elsevier Inc. All rights reserved.

Key words: Nanomedicine; Metallofullerenol nanoparticles; Cancer metastasis; Matrix metalloproteinase; Fibrous cage

Cancer nanotechnology has become an innovative trend with immense potential for the safe and efficacious clinical translation of chemotherapeutics to the clinic.[1-4] Engineered nanoparticles (NPs), often themselves pharmaceutically active,[5] provide for a robust platform that shows numerous advantages for cancer therapy compared to the conventional chemotherapeutics.[1] An exciting field within nanotechnology involves the investigation of carbon nanomaterials for biomedical applications in cancer treatment, including carbon nanotubes,[6,7] fullerenes, and their derivatives.[5,8] $Gd@C_{82}(OH)_x$ $(x = 20–24)$ endohedral metallofullerenol nanoparticles (f-NPs) were recently developed for biomedical applications involving imaging[9-11] and cancer therapy.[5,12] Our laboratory has reported that several mechanisms including regulatory effects on immune response[5,13] may

become involved in the anticancer outcome of this highly biocompatible nanoparticle.[12,14,15] In our previous study we utilized high-throughput gene array analysis to identify and distinguish the targeted genes that are responsive to f-NPs treatment.[12] This technique revealed that the matrix metalloproteinase (MMP) family showed strong inhibitory responsiveness to the f-NPs treatment.[12] We therefore asked if f-NPs can be utilized in a disease scenario in which MMPs have an important role, and therefore if the suppressed MMP could lead to a therapeutic outcome. One example is tumor metastasis in which MMP enzymes degrade all kinds of extracellular matrix (ECM) proteins and facilitate tumor invasiveness.[16] Tumor metastasis, which remains a tremendous hurdle and a major contributor to more than 90% of cancer deaths,[17,18] comprises a multitude of steps, with the initiating stage consisting of degradation of the ECM.[16] For a tumor to invade and intravasate into blood vessels, it must first break free from its own immediate confines, which consist of a fibrin-[19] and collagen-dense matrix.[20] To accomplish this, the tumor relies on tumor-associated macrophages (TAMs) capable of secretion of proteases, mainly MMPs, that break down the ECM in the peripheral space of tumors, allowing for the escape.[21] The objective of this study was to study the interactions between metallofullerenols and components of the tumor microenvironment specifically through regulation of secreted cytokines (e.g., MMP) that facilitate cancer invasion, and to examine the antimetastasis effects arising from here.

Methods

Preparation of f-NPs

Gadolinium metallofullerene (Gd@C_{82}) was synthesized by an arc-discharge method using composite rods consisting of Gd_2O_3 (purity >99.99%; Sigma-Aldrich, St Louis, Missouri) and graphite (purity >99.99%, Beijing Chemical Co., Beijing, China) in a 450-torr He gas atmosphere as we described elsewhere.[5,9,12,22-24] A graphite rod filled with an atomic ratio of Gd/Ni/C = 1:1:100 was used as the anode for arc burning. The raw soot was collected and extracted in N,N-dimethylformamide (Beijing Chemical Co. Nishitama, Tokyo, Kyoto, Japan) at 170°C for 12 hours. The N,N-dimethylformamide solution was then transferred into water-free toluene. Gd@C_{82} was subsequently separated by a two-step high-performance liquid chromatography (LC908-C60; Japan Analytical Industry Co., Nishitama, Tokyo, Japan) equipped with a 5PBB column (Nacalai Co., Kyoto, Japan) followed by Buckyprep column (Nacalai Co.). To synthesize metallofullerenol, we mixed Gd@C_{82} solution with 50% NaOH water solution containing 0.1 mL 40% tetrabutylammonium hydroxide (Sigma-Aldrich). After stirring for 12 hours at room temperature (22–28°C), the precipitate was carefully collected. To remove excess tetrabutylammonium hydroxide and NaOH, the precipitate was repeatedly washed by methanol and water. Subsequently, the precipitate was dissolved in water with continuous stirring for 24 hours. To obtain Gd@C_{82}(OH)$_{22}$, the concentrated Gd@C_{82}(OH)$_x$ aqueous solution was purified by a Sephadex G-25 column chromatography with an eluent of distilled water. The molecular

weight was determined by elemental analysis, matrix-assisted laser desorption/ionization–time-of-flight–mass spectrometry (AutoFlex; Bruker Co., Bremen, Germany) and x-ray photo-emission spectroscopy (Beijing Synchrotron Radiation Facility) as we described elsewhere.[24]

Physicochemical characterization and stability evaluation of f-NPs

The morphology of the f-NPs was characterized by transmission electron microscopy (TEM, CM120; FEI, Hillsboro, Oregon). Particle size and zeta potential were measured in pure water, saline, and saline supplemented with 1% mouse serum by ZetaSizer Nano (Malvern Instruments, Worcestershire, United Kingdom). All the measurements were performed at a particle concentration of 100 μg/mL.

To evaluate the stability of f-NPs, transparency check, dynamic light scattering (DLS), and inductively coupled plasma mass spectroscopy (ICP-MS) analysis were performed. f-NPs were suspended in saline with or without 1% mouse serum at 100 μg/mL and sonicated for 10 minutes before the experiment. Particle size kinetics measurements were conducted using DLS from 0 to 6 days. Photographs of the f-NPs suspension were taken at days 0 and 6. To determine whether Gd^{3+} ions could be released from the carbon cage, a dialysis experiment was performed. The dialysis bag (1000-Da cutoff size) was filled with 5 mL 100 μg/mL f-NPs suspension, then dialyzed against 200 mL saline with or without serum. The Gd concentrations in the dialysis bags were measured at days 0 and 6 by ICP-MS analysis.

Cell culture

MDA-MB-231 and MDA-MB-231-luc (constitutively expressing luciferase) cancer cells were cultured in Dulbecco's modified Eagle medium (DMEM; Gibco, Frederick, Maryland) containing 10% fetal bovine serum, 100 U/mL penicillin, 100 μg/mL streptomycin, and 2 mM L-glutamine. To generate a MDA-MBA-231 cell line constitutively expressing green fluorescent protein (GFP), 1×10^5 cancer cells were transduced with lentivirus in a six-well tissue culture plate. The virus-containing medium was removed after 16 hours and the cultures replenished with fresh DMEM. Cells were allowed to proliferate to 1×10^6 cells. The GFP cancer cells were used within five generations after transduction. U937 macrophages were cultured in DMEM (Gibco) supplemented with 10% fetal bovine serum, 100 U/mL penicillin, and 100 μg/mL streptomycin.

Determination of MMP in macrophage or cancer cell–macrophage co-cultured system

MDA-MB-231 cancer cells were seeded into an upper inserted chamber that was supported by a permeable membrane with 3-μm pores. U937 macrophage cells were seeded into the lower chamber of the transwell in 2 mL complete DMEM. Cancer cells and macrophages were exposed to f-NPs at indicated concentrations for 96 hours. In parallel, U937 cells were solely cultured in the same medium in the presence of f-NPs at indicated concentrations for 96 hours. RNA samples were collected for quantitative polymerase chain

reaction (qPCR) analysis. The total protein was collected for the western blotting experiment.

RNA extraction and qPCR analysis

To identify the amount of MMP-2 and MMP-9 messenger RNA (mRNA), cell and tumor samples were collected for qPCR analysis. Total RNA was extracted using the commercially available kit (NucleoSpin RNA II; Macherey-Nagel, Bethlehem, Pennsylvania) according to the manufacturer's protocol. qPCR analysis was performed using the iQ 5 multicolor qPCR detection system (Bio-Rad Laboratories, Hercules, California). The sequence-specific primer pairs are as follow. For tumor tissue samples, MMP-9-up: 5′-TGAATCAGCTGGCTTTTGTG-3′; MMP-9-down: 5′-GTGGATAGCTCGGTGGTGTT-3′; MMP-2-up: 5′- GGTCTCGATGGTGTTCTGGT-3′; MMP-2-down: 5′-GTCGCCCCTAAAACAGACAA-3′. For cell samples, MMP-9-up: 5′- GCCATTCACGTCGTCCTTAT-3′; MMP-9-down: 5′-TTGACAGCGACAAGAAGTGG-3′; MMP-2-up: 5′-ATGACAGCTGCACCACTGAG-3′; MMP-2-down: 5′-ATTTGTTGCCCAGGAAAGTG-3′. Results were analyzed using the ABI Prism SDS 2.0 software (Applied Biosystems, Foster City, California). Both tested genes were compared with β-actin for normalization.

Western blotting

To examine the MMP-2 and MMP-9 expression in cells or tumor tissues, the samples were washed in phosphate buffered saline and lysed in a lysis buffer containing protease inhibitor. The protein content in the extraction was determined by the Bradford method. Eighty micrograms of total protein were electrophoresed by 10% sodium dodecyl sulfate–polyacrylamide gel electrophoresis and transferred to a polyvinylidene fluoride membrane. After blocking using 5% milk, the membranes were incubated with 1:1000 dilution of primary monoclonal antibody to MMP-9 and MMP-2 (Santa Cruz Biotechnology, Santa Cruz, California) at 4°C overnight, respectively. The membranes were overlaid with secondary antibody (1:1000 dilution) before the addition of the horseradish peroxidase–conjugated streptavidin-biotin complex. The proteins were detected using ECL reagent (Invitrogen, Carlsbad, California) according to the manufacturer's instructions.

Matrigel invasion assay

MDA-MB-231-GFP and U937 cells were suspended to a final concentration of 1×10^5 cells and 2×10^4 cells in 500 μL serum-free DMEM in the upper insert that had been precoated with Matrigel (BD Science, Sparks, Maryland) and treated with f-NPs at various concentrations. We also included phorbol-12-myristate-13-acetate (PMA)[25] (0.1 nmol/mL), which is capable of enhancing the level of MMPs and caffeine[26] (150 nmol/mL) capable of suppressing MMPs in this assay. We also included small-molecule MMP inhibitors, CID 10667540 (MMP-2/MMP-9 inhibitor, 100 nM) and CP 471474 (broad-spectrum MMP inhibitor to MMP-1/-2/-3/-9/-13, 100 nM), in this assay. Twenty-four hours after various treatments, fluorescence intensity of GFP-expressing cancer cells that migrated through the Matrigel was detected. The nontreated cells were regarded as 100% in the invasion index calculation.

Animal

Athymic BALB/c nu/nu female mice (~16 g) were maintained under specific pathogen-free conditions. All animal experiments were performed under protocol approved by the Animal Care and Use Committee.

Tissue invasion model

The tumor cell suspension (0.2 mL, 1×10^7 cells/mL) was injected subcutaneously into mice. Thirty days after injection, the mice were killed and the subcutaneous tumors were divided into small pieces (3–4 mm^3). The small tumor tissues were then subcutaneously inoculated into the left inguinal region of mice using a trochar needle. Ten days after implantation, the mice were randomly divided into two groups ($n = 6$) and received daily intraperitoneal (i.p.) injections of f-NPs saline solution (2.5 μmol/kg) or saline alone for 6 weeks. Tumor metastasis was examined by bioluminescence imaging (BLI) at the end of treatments.

Blood vessel metastasis model

To see the effect of f-NPs in the situation in which a small amount of invasive cancer cells have already escaped from the primary site, 0.1 mL cancer cell suspension containing 1×10^6 cells was directly injected through tail vein. Seven days after injection, the mice were daily dosed with f-NPs at 2.5 μmol/kg or saline alone for 6 weeks by i.p. administration. Tumor metastases in lung were monitored weekly by BLI and magnetic resonance imaging (MRI). At the end of the experiment, positron emission tomography imaging was performed.
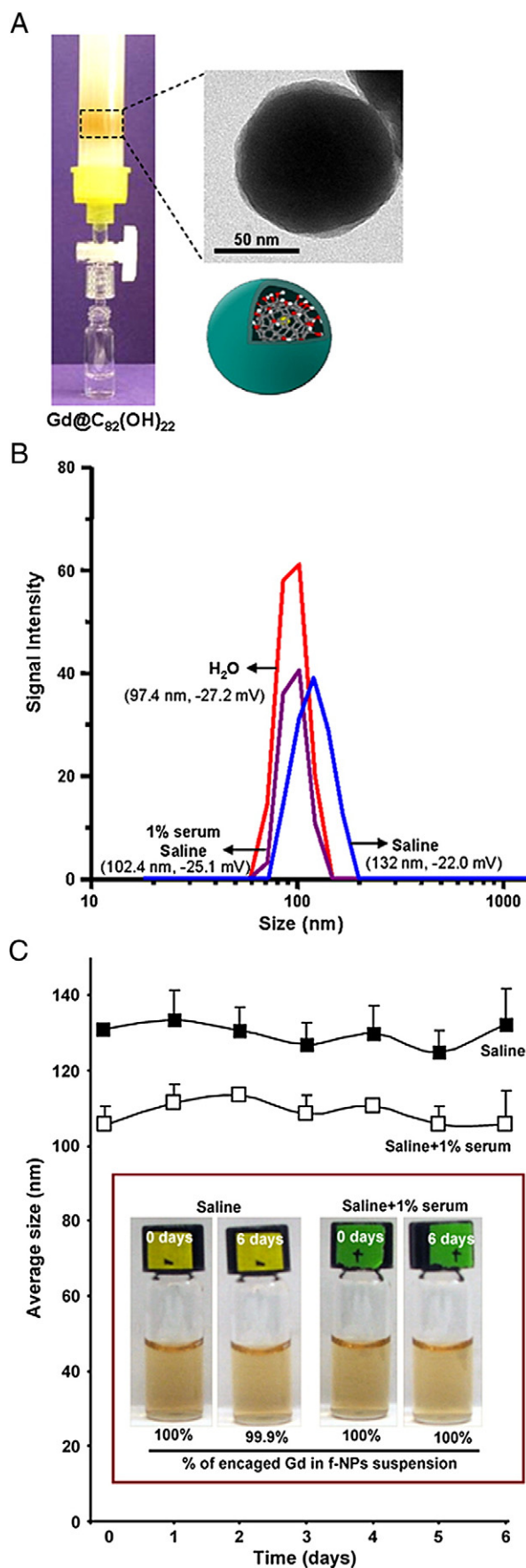
Bioluminescence imaging

To visualize the tumor metastasis, anesthetized tumor-bearing mice were injected intraperitoneally with 75 mg/kg D-luciferin (Caliper Life Sciences, Hopkinton, Massachusetts). The images were acquired using an IVIS Imaging System (Xenogen, Caliper Life Sciences). Acquisition time was 2 minutes. Analyses were performed with LIVINGIMAGE software (Caliper Life Sciences) by measuring photon flux in the region of interest. Note that the lower parts of the mouse body required covering so as to achieve adequate contrast for imaging at the ectopic site.

Histological examination

In a tissue invasion model, the primary tumor tissue together with major organs (heart, lung, spleen, liver, kidney, brain, bone, and muscle) were quickly collected and fixed for histology analysis. Parts of the tumor tissues were used for hematoxylin-eosin and Van Gieson (VG) staining. In a bloodstream transfer model, the lung tissues as well as normal tissues such as liver and kidney were collected for histology analysis. The sections were examined by light microscopy.

Figure 1. Synthesis and characterization of $Gd@C_{82}(OH)_{22}$ nanoparticles (f-NPs). **(A)** The hydroxyl-functionalized $Gd@C_{82}$ nanoparticles were purified by Sephadex G-25 column chromatography with an eluent of distilled water. TEM image shows the morphology of f-NPs. Scale bar, 50 nm. **(B)** Size distributions, average sizes (first value in parentheses), and zeta potentials of f-NPs (second value in parentheses) in different physiological aqueous solutions were analyzed. **(C)** Stability of f-NPs in physiological solution was determined by transparency check, DLS, and ICP-MS analysis. f-NPs were suspended in saline with or without mouse serum (w/w, 1%) at 100 µg/mL and sonicated for 10 minutes before the measurement. Particle size measurements were conducted using DLS from 0 to 6 days. Photographs of f-NPs in saline were taken at 0 and 6 days. To determine whether Gd^{3+} ions could be released from the carbon cage, dialysis experiments were performed. The dialysis bags contained 5 mL f-NPs suspension at particle dose of 100 µg/mL, which was dialyzed against 200 mL saline with or without serum. Gd content in dialysis bags were measured at 0 and 6 days by ICP-MS.

Statistical analysis

All of the results were calculated as mean ± SD. The statistical significance of the differences between groups was analyzed by Student's *t*-test as well as analysis of variance using Excel software (Microsoft, Seattle, Washington) at a significance level of 0.05.

Results

Characterization and stability study of the metallofullerenol nanoparticles
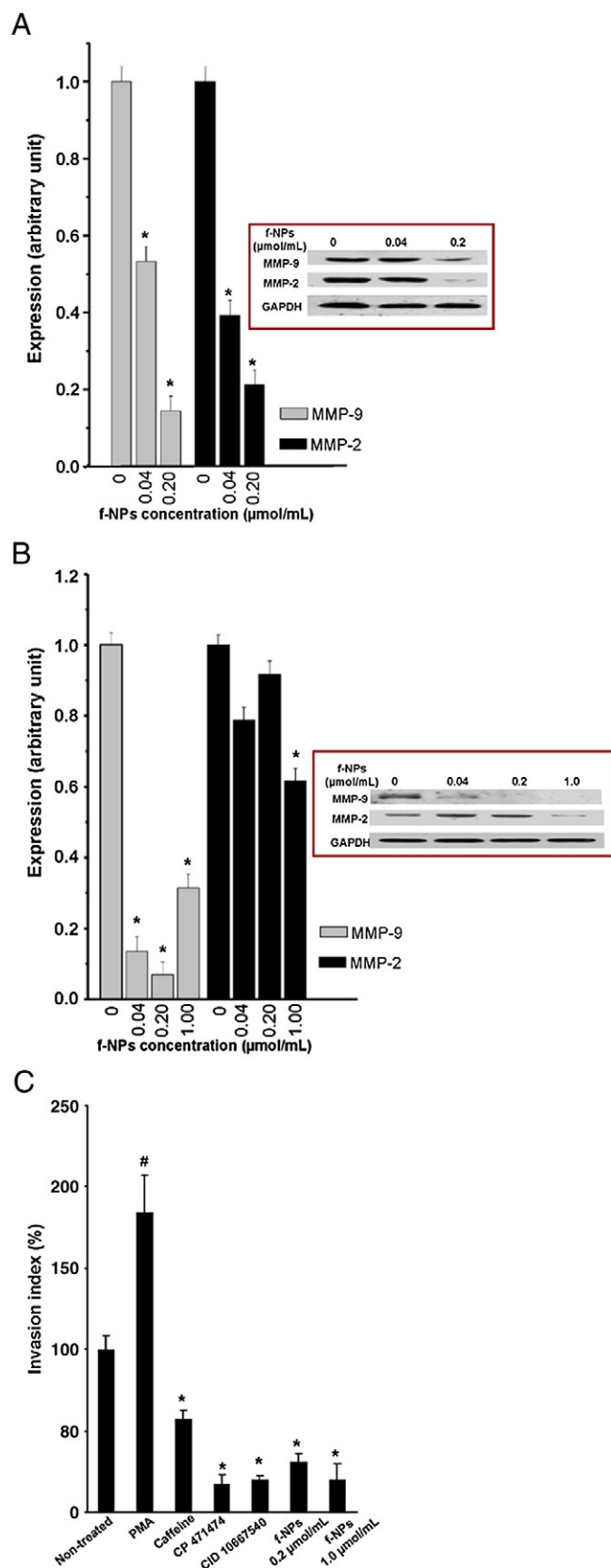
The engineered f-NPs were developed to possess a viruslike nanostructure functionalized with a certain number of hydroxyl groups on the surface. The morphology of the NPs was found to be spherical/ellipsoidal in nature, with a primary size of ~100 nm, as verified using TEM (Figure 1, *A*). The size of f-NPs was corroborated using DLS, with the f-NPs showing a single peak size distribution in physiological medium, all the while exhibiting a negative zeta potential (Figure 1, *B*).

Transparency check, DLS, and ICP-MS analysis were used as three parallel methods to evaluate the stability of f-NPs in physiological conditions. Figure 1, *C* shows that f-NPs maintained optical transparency and remained in the ~100- and ~130-nm size range during the 6-day kinetics study in saline with and without mouse serum, respectively. Using a dialysis experiment, it was possible to determine whether the Gd^{3+} ions could be released during the incubation. The Gd concentration in the dialysis bag at day 0 was used as the reference value to calculate particle stability at a later time point. In agreement with the DLS data, ICP-MS measurement indicated that there was no significant Gd^{3+} ions release within 6 days, an indication of the intrinsic stability of f-NPs in these solutions (Figure 1, *C*).

f-NPs inhibited the production of MMPs and cancer cell invasion in vitro

To test whether TAMs-mediated production of MMP was influenced by f-NPs treatment, we examined the effect of f-NPs in macrophages and in a cancer cell–macrophage co-culture system. MMP-2 and MMP-9 are examined, because many ECM

components (e.g., collagens and gelatin) could be digested by these MMP molecules.[27] The amounts of MMP-9 and MMP-2 mRNA in TAMs following administration of f-NPs were measured, and the results are shown in Figure 2, *A*. The presence of the f-NPs in increasing doses decreased MMP-9 and MMP-2 mRNA expression in human U937 TAMs-like cells (Figure 2, *A*). Significant decreases in both MMP-9 and MMP-2 were observed by f-NPs treatment at 0.04 μmol/mL. The dose-dependent decreasing trends of MMP-9 and MMP-2 expression were confirmed by western blotting (Figure 2, *A*, insert). Please note that non-metallofullerenol $[C_{60}(OH)_{22}]$ and $GdCl_3$ have no effects on inhibiting MMPs expression (Supplementary Figure S1, available online at http://www.nanomedjournal.com). The levels of these MMPs were then examined in an experiment involving co-culture of U937 cells with MDA-MB-231 cancer cells, so as to evaluate the effect of a potential cross-talk between cancer cells and macrophages. As can be seen in Figure 2, *B*, the f-NPs had a dramatic effect on MMP-9 expression, bringing about an enormous and sustained decrease at 0.04 μmol/mL. As is evident, the cancer cells co-incubated with the TAMs were found to have an inhibitory effect on the decrease of MMP-2 expression, highlighting the link that exists between TAMs and cancer cells. Although MMP-2 was not as sensitive as MMP-9 to the f-NPs treatment, the NPs were capable of inducing a ~40% decrease in MMP-2 expression at 1 μmol/mL, whereas for MMP-9, a decrease of 90% occurred at a dose of only 0.04 μmol/mL (Figure 2, *B*). These results were also confirmed by western blotting (Figure 2, *B*, insert).

To escape from the primary tumor site, invasive cancer cells require the assistance of MMP enzymes capable of degrading collagen components in the ECM. We are therefore interested in whether the MMP inhibition could be linked to a decreased cancer invasive potential in the presence of f-NPs in vitro. To answer this question, a Matrigel invasion experiment was used to study the effects of f-NPs. The data showed that PMA (which is able to increase MMP production[25]) significantly promoted cell invasion; however, f-NPs and caffeine (which is able to decrease MMP production[26]) potently inhibited the invasion of MDA-MBA-231 cells in this assay (Figure 2, *C*). To further strengthen our conclusion, we also assayed the effect of small-molecule MMP inhibitors (CP 471474 and CID 10667540). In agreement with the effect of f-NPs, these MMP inhibitors also showed a significant inhibition of cancer cell migration (Figure 2, *C*).

Figure 2. Study of the effects of f-NPs on MMP regulation and cancer cell invasion in vitro. **(A)** qPCR (histogram) and western blotting (insert) were used to study the level of MMP-9 and MMP-2 in U937 cells treated with f-NPs at various concentrations. *$P < 0.05$, compared to control. **(B)** qPCR (histogram) and western blotting (insert) were used to determine MMP-9 and MMP-2 levels in MDA-MB-231/U937 co-cultured system in the presence of f-NPs at indicated concentrations. *$P < 0.05$, compared to control. **(C)** To study the effect of f-NPs on cancer cell invasion, the GFP-labeled cancer cells that were able to pass through the Matrigel-coated membranes toward serum-containing medium (chemoattractant) were detected. PMA-, caffeine-, and small-molecule MMP inhibitors (CP 471474, CID 10667540)–treated cells were included in the assay. Nontreated cells were considered as 100% in the calculation of the invasion index. *$P < 0.05$, significantly lower compared to control; #$P < 0.05$, significantly higher compared to non-treated cells.
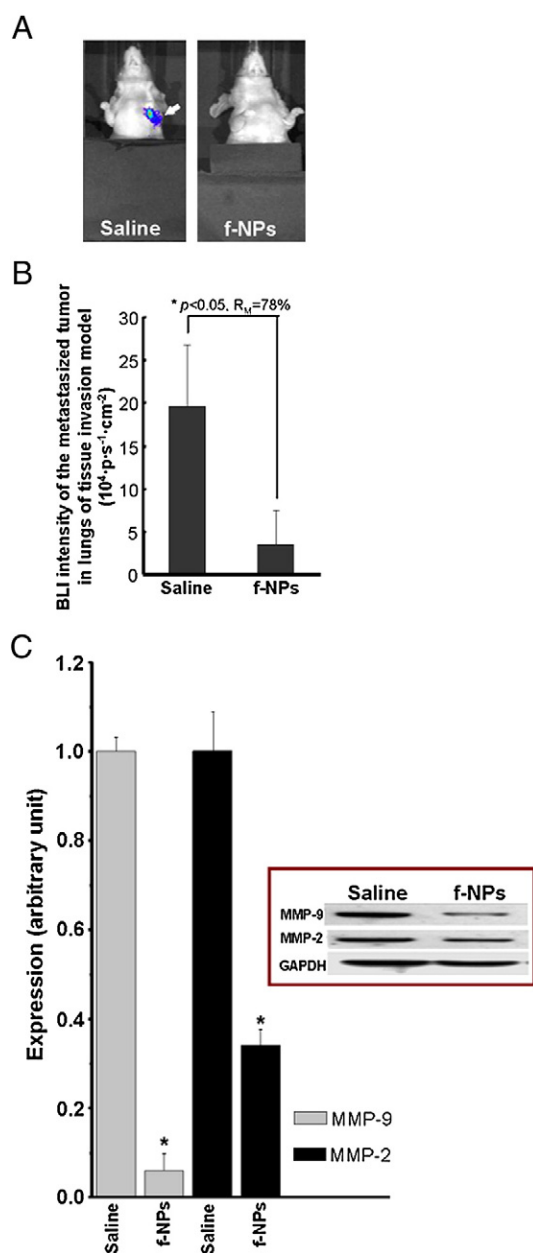
Figure 3. The f-NPs potently inhibited tumor metastasis in the tissue invasion animal model. **(A)** Representative bioluminescence images (BLI) of tumor foci obtained from control (*left*) and the f-NPs–treated animals (*right*) after the course of treatment. **(B)** Quantification of the bioluminescence intensity of tumor foci in the lungs of animals after the course of treatment. f-NPs treatment significantly inhibited tumor metastasis with an $R_M = 78\%$ in the tissue invasion model. *$P < 0.05$, compared with saline control. **(C)** The levels of MMP-9 and MMP-2 in the primary tumor tissues treated with f-NPs or saline were determined by qPCR (histogram) and western blotting (insert). *$P < 0.05$, compared to control.

f-NPs significantly inhibited tumor metastasis in a tissue invasion model along with MMP inhibition

To test whether f-NPs are able to inhibit MMP in vivo, including the capability of inhibition on tumor metastasis, we subsequently examined the effects of f-NPs in an MDA-MB-231

xenograft mouse model where lung metastasis frequently occurs.[28,29] To visualize tumor metastasis in nude mice, MDA-MB-231-luc cells that express a luciferase gene were utilized for the ease of localization via BLI. Ten days after tumor implantation in the groin (primary tumor), the animals received daily intraperitoneal injections of either the f-NPs at 2.5 μmol/kg or saline, for a sustained duration of 6 weeks. Consistent with our previous findings,[5,8,15] the f-NPs–treated animals showed significant tumor inhibition of the primary tumor (which was covered by black paper) compared to saline control. Following examination of tumor metastasis, tumor foci were only observed in the lungs and lymph of mice receiving saline injections 6 weeks after implantation, but not in animals treated with f-NPs (Figure 3, A). To quantify the ability of f-NPs to inhibit the metastatic potential of tumors, the inhibition rate of tumor metastasis (R_M) was defined by the following equation:

$$R_M = [1 - (I_{NP} - BG) / (I_S - BG)] \times 100\%$$

where I_S represents the intensity of BLI signal in the saline group, I_{NP} the intensity in the same area of f-NPs–treated mice, and BG is BLI background. The f-NPs treatment significantly inhibited tumor metastasis in the ectopic site and resulted in an average R_M of ~78% (Figure 3, B). Note that no abnormal behavior, body weight loss, and histological abnormalities were observed during the 6-week treatment.

In the tissue culture condition, we have shown that the level of MMP was remarkably inhibited in the presence of f-NPs (Figure 2). In light of these findings, the question remains as to whether MMP inhibition has a role in the therapeutic outcome of f-NPs in vivo. The qPCR results demonstrated a >90% and >60% decrease in MMP-9 and MMP-2 in tumor tissues, respectively, as compared to the control. This result was further bolstered by western blotting (Figure 3, C, insert).

f-NPs isolated cancer cells within a dense fibrous cage

Interestingly, histological examination of primary subcutaneous tumor using VG staining demonstrated a thick fibrous layer on the tumor surface in the f-NPs–treated mice but not in saline-treated mice, the results of which are shown in Figure 4. This dense connective tissue at the tumor boundary is easily discernible given the presence of VG staining, which allows for staining of collagen. Saline control tumors possessed a natural tumor ECM composed of fibrin and type I collagen. The capsule was homogeneous in size throughout, and had an average thickness of ~60 μm (Figure 4, A). In f-NPs–treated animals, the fibrous layer surrounding the surface of the primary tumor was ~450 μm thick (Figure 4, B). A similar fibrous cage was also found in another breast cancer model, MCF-7, showing layers with a thickness of ~32 μm and ~578 μm for saline (Figure 4, C) and f-NPs (Figure 4, D) treatments, respectively. Note that no remarkable deposition of fibrous tissue was observed in other major organs. A closer examination of the tumor tissues from saline- and f-NPs–treated animals was conducted using TEM (Supplementary Figure S2). Saline-treated tumor tissue did not show the presence of collagen fibers under TEM. Contrastingly, collagen fibers can be easily found in tumor tissue treated with f-NPs.
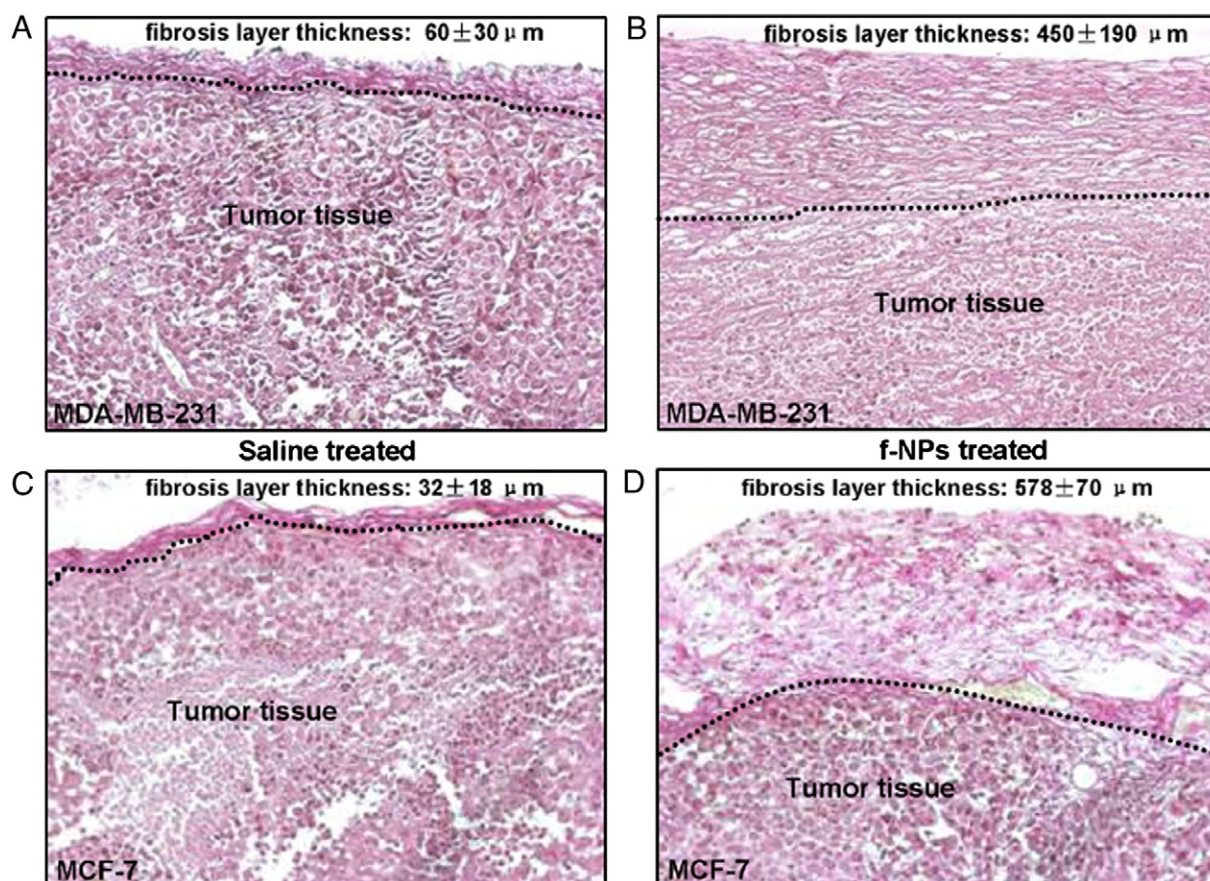
Figure 4. Photomicrographs of histological slides of excised tumors using Van Gieson staining to differentiate collagen fibers at tumor site in control and f-NPs–treated animals, respectively. **(A)** The excised tumors of the control mice and **(B)** of the f-NPs–treated mice of MDA-MB-231 human breast cancer model. **(C)** The excised tumors of the control mice and **(D)** of the f-NPs–treated mice of another human breast cancer model, MCF-7. The dotted line represents the boundary between the tumor and its fibrous capsule. The average thicknesses of fibrous capsules on the tumors in the f-NPs–treated group were 7–18 times larger than those of the control depending on tumor type.

f-NPs significantly inhibited the establishment of tumor foci in lung in a bloodstream transfer model

The prognosis and survival rate greatly depend on the stage of the cancer and the extent of cancer spread.[30] We have demonstrated that f-NPs potently suppress tumor metastasis in a tissue invasion model, but because f-NPs cannot completely eliminate tumor invasion, there is a need for the data in the bloodstream transfer model, in which the cancer cells were directly injected into bloodstream. These data can help determine whether f-NPs would be able to inhibit the establishment of tumor foci and subsequent tumor growth if a small amount of invasive cancer cells have already escaped from the primary site. As can be seen in Figure 5, *A*, tumor signal was detected in the lungs ~21 days after cancer cell injection in the saline group. By contrast, no cancer signal could be detected in mice with f-NPs treatment at this time point, and tumors did not appear in f-NPs group until day 42. Again, R_M was calculated at the end point of experimentation using BLI readout, the results of which can be seen in Figure 5, *B*. The treatment using f-NPs significantly suppressed the establishment of tumor foci in lungs compared to saline control, with an average R_M of 88%. These findings were

further corroborated by ^{18}F-fluorodeoxyglucose positron emission tomography (Supplementary Figure S3) and MRI results (Supplementary Figure S4). These diverse imaging data provide extra resolution by which f-NPs inhibition of tumor metastasis could be monitored in detail. Histological examination of the lungs of animals that received the various treatments further highlight the efficacy of f-NPs treatment. The saline control showed the presence of numerous tumor foci, as evidenced by the clusters of large, irregularly shaped tumor cells with darkly staining nuclei. In contrast, the lungs of animals receiving f-NPs showed minimal signs of tumor presence (Figure 5, *C*).

Discussion

In this study we demonstrated that f-NPs potently suppressed MMPs at mRNA and protein levels in macrophage and a cancer cell–macrophage co-culture system. We further demonstrated that f-NPs caused a suppression of cancer cell invasion through Matrigel. In the tissue invasion animal model, we demonstrated that the treatment using f-NPs potently prevented metastasis and restricted tumor invasion mainly through an MMP-inhibitory process. Interestingly, f-NPs were able to induce a thick and
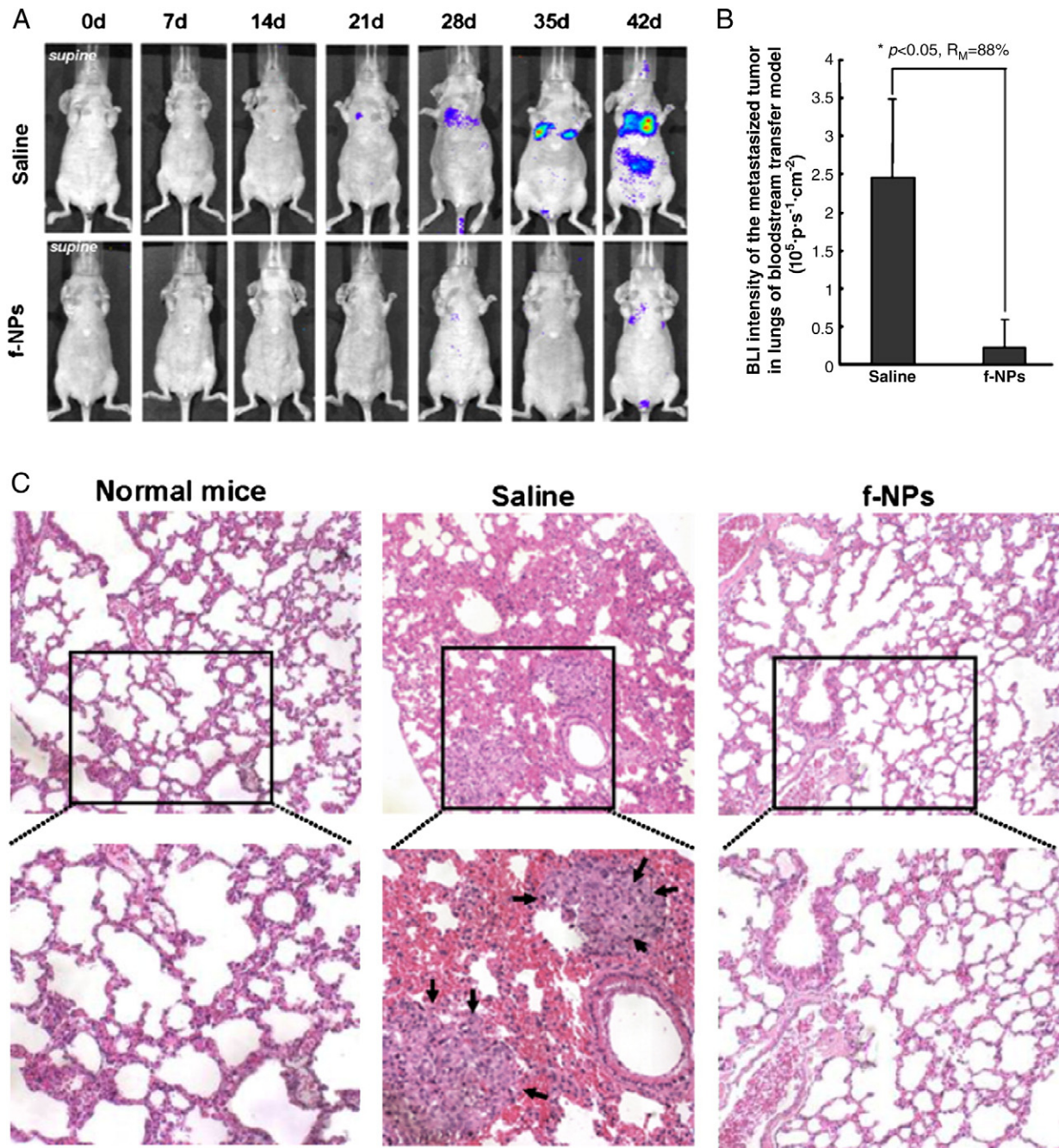
Figure 5. f-NPs potently inhibited the establishment of tumor foci in the blood transfer model of MDA-MB-231-luc cancer mice. **(A)** MDA-MB-231-luc cells were harvested and resuspended at a concentration of 1×10^7 cells/mL in saline. A 0.1-mL cell suspension was injected into the tail vein of the nude mice. Seven days after cancer cell injection, the mice received daily intraperitoneal doses of the f-NPs at 2.5 μmol/kg for a duration of 6 weeks. Saline was used as control. Tumor metastases in lung were monitored weekly by BLI. **(B)** Quantification of the BLI intensity of tumor foci in the lungs of animals after different treatments. f-NPs treatment significantly inhibited tumor metastasis with an R_M = 88% in the bloodstream transfer model. *$P < 0.05$, compared to control. **(C)** Histological examination of the lungs with different treatments was performed. *Arrows* indicate the tumor foci in a saline-treated animal. Higher magnification images of animal lung are shown in the lower panel.

dense fibrous cage. This may be in large part due to the NP treatment's ability to reduce the expression of MMPs and resulting accumulation of fibrous components. In an animal model simulating bloodstream metastasis, f-NPs treatment was also capable of preventing tumor foci establishment in lung. The present findings may suggest a new strategy in cancer

therapeutics using engineered NP, namely imprisoning instead of poisoning cancer cells.

Production of MMPs at tumor sites has been shown to be upregulated in several human tumors, and if left rampant and unchecked, degrades the matrix surrounding the tumor, allowing for tumor invasion into surrounding tissues and the circulation.[31]
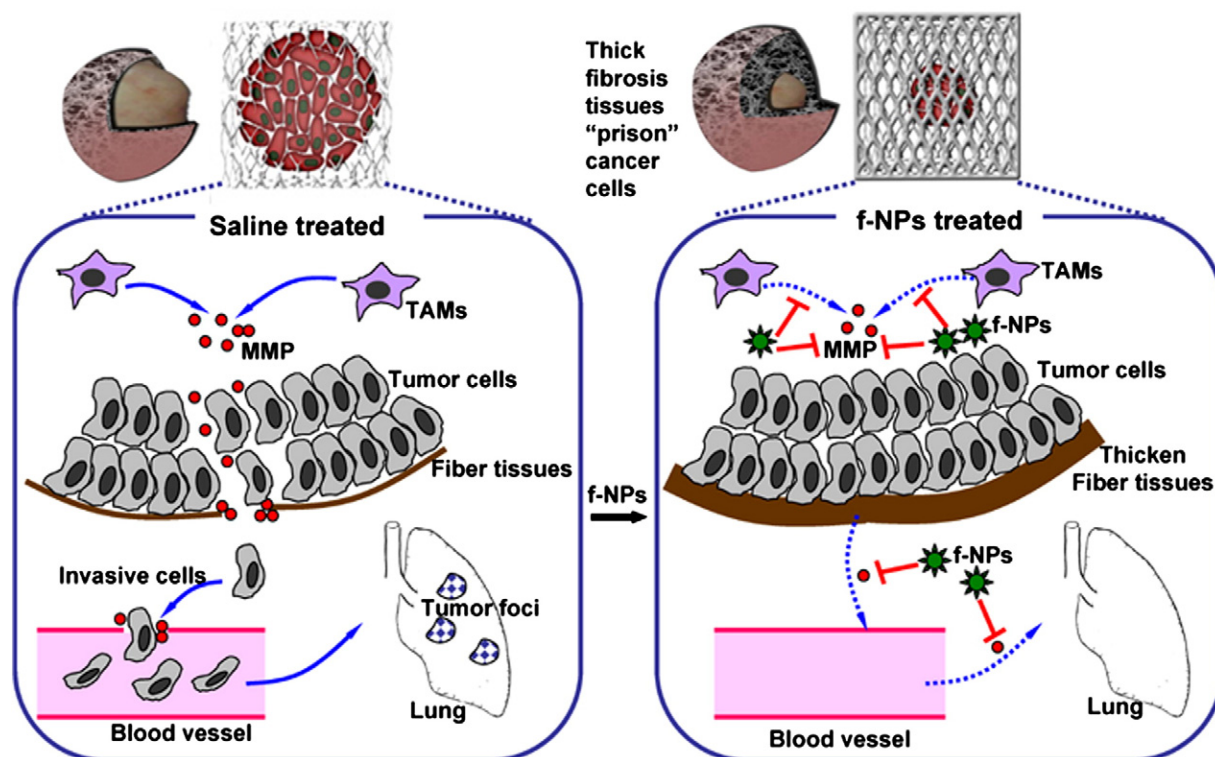
Figure 6. Schematic presentation of possible antimetastasis mechanism of f-NPs. Rather than direct cell killing, the metallofullerenol nanoparticles inhibited tumor metastases mainly through a MMP inhibition process. In the control group (*left panel*), TAMs-secreted MMP enzymes are able to efficiently degrade the fibrous matrices surrounding tumors and facilitate their invasiveness. In the nanoparticle-treated group (*right panel*), f-NPs decreased the production of MMP, subsequently reducing fibrous matrix degradation. The thick fibrous cage may therefore serve as a "prison" that tightly confines the invasive cancer cells within the primary site.

The downregulation of MMP expression in the tumor microenvironment is known as a major contributing factor in the decreased metastatic potential of tumors.[31] It has been demonstrated that small-molecule inhibitors of MMPs, including synthetic and natural compounds–based MMP inhibitors, would be useful to prevent tumor metastasis.[32] However, many MMP inhibitors eventually fail in the clinical trial because of unexpected side effects and toxicity (e.g., musculoskeletal syndrome), poor pharmacokinetic profile, low bioavailability, etc.[32] These disappointing results highlight the need for a new type of MMP inhibitor such as a pharmaceutically active NP, which shows more effectiveness, high bioavailability, and low toxicity.

Another interesting finding in this work is the establishment of fibrous encapsulation that was mainly composed of collagen components (Figure 4). Although we do not have a full understanding of how the fibrous cage was formed, it is worthwhile to consider the important role of the decreased MMP level that is responsible for ECM degradation and further excessive collagen deposition. The lack of MMP expression allowed for thickening of the connective tissue boundary around the tumor, a direct product of the body's natural inflammatory response. This point is in agreement with previous findings[33] and has been experimentally proved by an in vitro collagen degradation assay (Supplementary Figure S5). However, in the presence of abundant MMPs, levels like those found in tumors of control mice, the fibrous layer would have undergone degrada-

tion that facilitates tumor invasion. Aside from the fibrous cage in the MDA-MB-231 breast cancer, a similar fibrous composition was also found in another breast cancer, the MCF-7 cancer model (Figure 4, *C* and *D*). This implies that the novel phenomenon can be applied to several different tumor types.

The thick collagen boundary surrounding the tumor surface may have several important roles in preventing metastasis. First, the fibrous layer separating the invasive cancer cells from normal tissue may act as a barrier that prevented cross-talk and signaling between the cancer cells and TAMs, thereby preventing production of the MMP enzymes. Several novel therapeutic strategies are currently being explored to exploit the link between macrophages, tumors, and metastasis. As an example, depletion of macrophages was able to reduce lung metastases in mouse models of polyoma middle T–induced mammary cancer.[34] Concomitantly, if the phenotype of TAMs can be reversed, macrophages can be used to restrain tumor growth rather than promote it.[35] Second, the thickened capsule that developed around the tumor over the course of f-NPs treatment physically encased the tumor within a matrix that may prevent cancer cells from escaping.[36,37] This possibility is also supported by a previous finding that expansion of tumor cells within a three-dimensional matrix of type I collagen or cross-linked fibrin was restricted in the absence of MMP.[37] With a low level of proteolysis, tumor cells that were embedded in ECM matrices were trapped in a compact, spherical configuration and failed in

the cytoskeletal reorganization that is necessary for tumor growth and invasion.[37] Understanding of the antimetastasis activity of f-NPs may lead to a new approach in cancer metastasis management—namely, solid-tumor encapsulation using engineered NPs instead of direct cell killing as has been largely involved in conventional chemotherapeutics. Indeed, more in-depth mechanistic studies are needed to fully understand the function of this thick collagen layer, including how the layer is formed. This may involve the sophisticated regulatory mechanisms in which f-NPs treatment could influence cytokine and growth factor release (e.g., TGF-β1), alter proliferation and differentiation in fibroblasts, and decrease matrix degradation (e.g., MMP inhibition), etc.

Compared to existing chemicals capable of MMP inhibition, the f-NPs exhibited a safe and efficient nanotherapeutic platform for cancer metastasis management. These NPs hold great potential for antimetastatic treatment because of several properties. First, upon circulation in the bloodstream, f-NPs could preferentially accumulate in the stroma of the tumor surface, which may be due to a result of the enhanced permeability and retention effect.[38] Their particle phase may result in their being phagocytosed by immune cells both in the bloodstream (e.g., monocytes) and partially by resident TAMs at tumor sites, where they can exert immunoregulatory effects, such as affecting cytokine (e.g., MMP) secretion. Second, the f-NPs potently inhibited a series of key factors that triggered tumor metastasis,[12] including MMPs and angiogenesis factors.[12] The multiple bioactivities of the f-NPs may contribute to the therapeutic outcome via a combined and/or synergistic effect.[5,12-15] Third, the nontoxic nature of the f-NPs,[5,12] such as lack of toxicity to normal organs (Supplementary Figure S6) allows patients to receive continuous and long-term treatment, which is usually impossible for most anticancer agents including many existing MMP inhibitors.[32]

In summary, we demonstrated a novel approach using Gd@C$_{82}$(OH)$_{22}$ metallofullerenol nanoparticles to inhibit tumor metastasis. Rather than direct cell killing, the NPs inhibited tumor metastasis mainly through an MMP-inhibitory process. The formation of a thick fibrous cage may serve as a "prison" capable of confining the invasive tumor cells in their primary site (Figure 6). We anticipate that these findings will result in a new approach in the management of tumor metastasis, namely, imprisoning instead of poisoning cancer cells.

Appendix A. Supplementary data

Supplementary data to this article can be found online at doi:10.1016/j.nano.2011.08.019.

References

1. Ferrari M. Cancer nanotechnology: opportunities and challenges. Nat Rev Cancer 2005;106:161-71.
2. Qian X, Peng XH, Ansari DO, Yin-Goen Q, Chen GZ, Shin DM, et al. In vivo tumor targeting and spectroscopic detection with surface-enhanced Raman nanoparticle tags. Nat Biotechnol 2008;26:83-90.
3. Stoeva SI, Lee JS, Smith JE, Rosen ST, Mirkin CA. Multiplexed detection of protein cancer markers with biobarcoded nanoparticle probes. J Am Chem Soc 2006;128:8378-9.
4. Zheng G, Patolsky F, Cui Y, Wang WU, Lieber CM. Multiplexed electrical detection of cancer markers with nanowire sensor arrays. Nat Biotechnol 2005;23:1294-301.
5. Chen C, Xing G, Wang J, Zhao Y, Li B, Tang J, et al. Multihydroxylated [Gd@C$_{82}$(OH)$_{22}$]$_n$ nanoparticles: antineoplastic activity of high efficiency and low toxicity. Nano Lett 2005;5:2050-7.
6. Liu Z, Cai W, He L, Nakayama N, Chen K, Sun X, et al. In vivo biodistribution and highly efficient tumour targeting of carbon nanotubes in mice. Nat Nanotechnol 2007;2:47-52.
7. Liu Z, Davis C, Cai W, He L, Chen X, Dai H. Circulation and long-term fate of functionalized, biocompatible single-walled carbon nanotubes in mice probed by Raman spectroscopy. Proc Natl Acad Sci U S A 2008;105:1410-5.
8. Liang XJ, Meng H, Wang Y, He H, Meng J, Lu J, et al. Metallofullerene nanoparticles circumvent tumor resistance to cisplatin by reactivating endocytosis. Proc Natl Acad Sci U S A 2010;107:7449-54.
9. Xing G, Yuan H, He R, Gao X, Jing L, Zhao F, et al. The strong MRI relaxivity of paramagnetic nanoparticles. J Phys Chem B 2008;112:6288-91.
10. Shu CY, Wang CR, Zhang JF, Gibson HW, Dorn HC, Corwin FD, et al. Organophosphonate functionalized Gd@C$_{82}$ as a magnetic resonance imaging contrast agent. Chem Mater 2008;20:2106-9.
11. Mikawa M, Kato H, Okumura M, Narazaki M, Kanazawa Y, Miwa N, et al. Paramagnetic water-soluble metallofullerenes having the highest relaxivity for MRI contrast agents. Bioconjug Chem 2001;12:510-4.
12. Meng H, Xing G, Sun B, Zhao F, Lei H, Li W, et al. Potent angiogenesis inhibition by the particulate form of fullerene derivatives. ACS Nano 2010;4:2773-83.
13. Liu Y, Jiao F, Qiu Y, Li W, Lao F, Zhou G, et al. The effect of Gd@C$_{82}$(OH)$_{22}$ nanoparticles on the release of Th1/Th2 cytokines and induction of TNF-α mediated cellular immunity. Biomaterials 2009;30:3934-45.
14. Wang J, Chen C, Li B, Yu H, Zhao Y, Sun J, et al. Antioxidative function and biodistribution of [Gd@C$_{82}$(OH)$_{22}$]$_n$ nanoparticles in tumor-bearing mice. Biochem Pharmacol 2006;71:872-81.
15. Yin JJ, Lao F, Meng J, Fu PP, Zhao Y, Xing G, et al. Inhibition of tumor growth by endohedral metallofullerenol nanoparticles optimized as reactive oxygen species scavenger. Mol Pharmacol 2008;74:1132-40.
16. Yin D, Ge Z, Yang W, Liu C, Yuan Y. Inhibition of tumor metastasis in vivo by combination of paclitaxel and hyaluronic acid. Cancer Lett 2006;243:71-9.
17. Jemal A, Siegel R, Ward E, Hao Y, Xu J, Murray T, et al. Cancer statistics, 2008. CA Cancer J Clin 2008;58:71-96.
18. Liotta LA, Steeg PS, Stetler-Stevenson WG. Cancer metastasis and angiogenesis: an imbalance of positive and negative regulation. Cell 1991;64:327-36.
19. Dvorak HF, Senger DR, Dvorak AM. Fibrin as a component of the tumor stroma: origins and biological significance. Cancer Metastasis Rev 1983;2:41-73.
20. Tlsty TD, Coussens LM. Tumor stroma and regulation of cancer development. Annu Rev Pathol 2006;1:119-50.
21. Lewis CE, Pollard JW. Distinct role of macrophages in different tumor microenvironments. Cancer Res 2006;66:605-12.
22. Tang J, Xing G, Yuan H, Cao W, Jing L, Gao X, et al. Tuning electronic properties of metallic atom in bondage to a nanospace. J Phys Chem B 2005;109:8779-85.
23. Tang J, Xing G, Zhao F, Yuan H, Zhao Y. Modulation of structural and electronic properties of fullerene and metallofullerenes by surface chemical modifications. J Nanosci Nanotechnol 2007;7:1085-101.
24. Tang J, Xing G, Zhao Y, Jing L, Gao X, Cheng Y, et al. Periodical variation of electronic properties in polyhydroxylated metallofullerene materials. Adv Mater 2006;18:1458-62.

25. Li Y, Shen F, Liu B, Cheng G. Resveratrol inhibits matrix metalloproteinase-9 transcription in U937 cells. Acta Pharmacol Sin 2003;24:1167-71.
26. Liu WH, Chang LS. Caffeine induces matrix metalloproteinase-2 (MMP-2) and MMP-9 down-regulation in human leukemia U937 cells via Ca^{2+}/ROS-mediated suppression of ERK/c-fos pathway and activation of p38 MAPK/c-jun pathway. J Cell Physiol 2010;224:775-85.
27. Egeblad M, Werb Z. New functions for the matrix metalloproteinases in cancer progression. Nat Rev Cancer 2002;2:161-74.
28. Richert M, Phadke P, Matters G, DiGirolamo D, Washington S, Demers L, et al. Metastasis of hormone-independent breast cancer to lung and bone is decreased by alpha-difluoromethylornithine treatment. Breast Cancer Res 2005;7:R819-27.
29. Ran S, Mohamedali KA, Luster TA, Thorpe PE, Rosenblum MG. The vascular-ablative agent VEGF121/rGel inhibits pulmonary metastases of MDA-MB-231 breast tumors. Neoplasia 2005;7:486-96.
30. Merck Manual Online. Breast cancer. Whitehouse Station, NJ: Merck Sharp & Dohme [updated 2008 Nov]. Available from: http://www. merck.com/mmpe/print/sec18/ch253/ch253e.html.
31. Coussens LM, Fingleton B, Matrisian LM. Matrix metalloproteinase inhibitors and cancer—trials and tribulations. Science 2002;295:2387-92.
32. Mannello F. Natural bio-drugs as matrix metalloproteinase inhibitors: new perspectives on the horizon. Recent Pat Anticancer Drug Discov 2006;1:91-103.
33. Sierevogel MJ, Velema E, van der Meer FJ, Nijhuis MO, Smeets M, de Kleijn DP, et al. Matrix metalloproteinase inhibition reduces adventitial thickening and collagen accumulation following balloon dilation. Cardiovasc Res 2002;55:864-9.
34. Lin EY, Nguyen AV, Russell RG, Pollard JW. Colony-stimulating factor 1 promotes progression of mammary tumors to malignancy. J Exp Med 2001;193:727-40.
35. Bingle L, Brown NJ, Lewis CE. The role of tumour-associated macrophages in tumour progression: implications for new anticancer therapies. J Pathol 2002;196:254-65.
36. Yamada KM. Cell biology: tumour jailbreak. Nature 2003;424:889-90.
37. Hotary KB, Allen ED, Brooks PC, Datta NS, Long MW, Weiss SJ, Membrane type I. matrix metalloproteinase usurps tumor growth control imposed by the three-dimensional extracellular matrix. Cell 2003;114:33-45.
38. Maeda H. The enhanced permeability and retention (EPR) effect in tumor vasculature: the key role of tumor-selective macromolecular drug targeting. Adv Enzyme Regul 2001;41:189-207.

Appendix 5   Abstracts

1. Wang PC. Nanoparticles as Targeted Drug Delivery Vehicles for Molecular Imaging and Chemotherapy Applications. Hebei People's Hospital, Shijiazhuang, Hebei, China, Sep 13, 2011.

2. Wang PC. Nanoparticles as Targeted Drug Delivery Vehicles for Molecular Imaging and Chemotherapy Applications. Peking Union Medical College, Beijing, China, Sep 15, 2011.

3. Wang PC. Applications of Nanoparticles for In Vivo Imaging. Institute of Biophysics, Chinese Academy of Sciences, Beijing, China, Sep 16, 2011.

4. Wang PC. Nanoparticles as Targeted Drug Delivery Vehicles for Molecular Imaging and Chemotherapy Applications. Chinese National Center for Nanoscience and Nanotechnology, Beijing, China, Sep 16, 2011.

(These similar seminars were presented in four institutions in China within four days)

Abstract: Nanoparticles, which hold many unique properties, including versatility, tunable size, and highly adaptable surface chemistry, have been used successfully as imaging agents for in vivo imaging of various diseases. Using nanoparticles as imaging agents has significantly improved the detection sensitivity and specificity. Nanoparticles have great potential for early detection of cancer, genetic defects, cardiovascular and neurodegenerative diseases.

Using nanoparticles as an imaging agent provides new paradigms for every imaging modality: CT, MRI, PET, SPECT, Ultrasound, and Optical Imaging. Each imaging modality differs in detection sensitivity, depth penetration, spatial resolution, temporal resolution, costs, and whether it involves ionization radiation. Various materials, including liposome, dendrimer, micelle, polymer, gold nanoshell, colloidal gold, and fullerene, have been used to compose nanoparticles as imaging agents suitable for different imaging modalities. The physicochemical properties such as size, charge, shape, flexibility, hydrophilicity, and surface modification greatly influence the pharmacokinetics of nanoparticles, affecting their success as imaging agents. The nano-sized imaging agents need to stay within the system for a sufficient time in order to produce the desired image enhancement effects. Reducing exposure to foreign material by optimizing clearance is a central principle for minimizing unwanted effects of any foreign materials within the human body. Nanoparticles are cleared from the vascular compartment through three primary mechanisms: renal clearance with excretion into the urine, hepatic clearance with biliary excretion, or uptake by macrophages into the reticuloendothelial system. For clinical application, renal clearance will be a preferred route for nanoparticles as imaging agents.

Although many studies have accomplished making nanoparticles to be more effective imaging agents, there are still challenges ahead for nano imaging agents to be translational into routine clinical practice, including further improvement of targeting efficiency and specificity, and how to overcome the associated toxicity to the patients.

5.   **Wang PC. Nanoparticles as Targeted Drug Delivery Vehicles for Molecular Imaging and Chemotherapy Applications. University of Rhode Island, Kingston, RI, November 18, 2011.**

Nanoparticles as Targeted Drug Delivery Vehicles for Molecular Imaging and Chemotherapy Applications

Paul C. Wang, Ph.D.
Department of Radiology, Howard University, Washington, DC

Nanotechnology is a multidisciplinary scientific undertaking involving the creation and utilization of materials, devices, or systems on the nanometer scale. It is currently undergoing explosive development on many fronts and is expected to spark innovation and play a critical role in various biomedical applications, especially in drug delivery. Advances in nanotechnology that enable drugs to preserve their efficacy while being delivered to precise therapeutic targets are creating a host of opportunities for drug developers. By combining nanotechnology-based target-specific drug therapy with methods for early diagnosis of pathologies, we are getting closer to creating the ultimate functional drug carrier for personalized medicine. In this presentation, the molecular imaging techniques based on optical imaging and MRI will briefly be introduced. Two research studies, (1) using liposome labeled florescent dye and encapsulated MRI contrast agent as a dual probe for imaging, and (2) using metallofullerene nanoparticles to circumvent tumor resistance to cisplatin, will be presented as examples of applications of nanotechnology in imaging and therapy. Some challenges of using nanoparticles as drug delivery vehicles will also presented.

6.   **Wu CS, Huang S, Korotcov AV, Lin S, Andreev OA, Reshetnyak YK, Wang PC. pH Sensitive Nanoprobe for Tumor Targeting. Howard University Health Sciences Research Day 2012, Howard University, Washington, DC, April 13 2012, p. 21.**

Title: pH Sensitive Nanoprobe for Tumor Targeting

Authors: Chung-Shieh Wu, Sophia Huang, Alexandru Korotcov, Stephen Lin, Oleg A. Andreev, Yana K. Reshetnyak and Paul C. Wang[*], Department of Radiology

Background: pHLIP is a low pH-sensitive peptide that transforms into a α-helix and insert across a cell membrane at a low pH (<7.0) environment. In almost all solid tumors, the increased glucose catabolism results in significant production of lactate and H^+ ions which are pumped out from the intracellular space, producing an acidic extracellular tumor environment. Therefore, this peptide can be used to target acidic tumors *in vivo*. In this study, tumor uptake and the targeting capability of fluorescently labeled pHLIP probe in breast cancer model was investigated.

Methods: pHLIP was prepared by solid-phase peptide synthesis and conjugated with fluorescence dye (Alexa 750). The breast cancer tumor model was established by subcutaneous injection of $1×10^6$ MDA-MB-231-luc cells in female athymic nude mice. Caliper Spectrum Imaging machine was used for bioluminescence and fluorescence imaging. Bioluminescence images were used to monitor tumor growth. The fluorescence experiment was run when tumors reached 8-10 mm in diameter. Mice were intravenously injected with 40 µM of pHLIP probe in 100 µl of phosphate buffered saline (PBS). Fluorescence imaging was acquired every 15 minutes during the first 1 hour, and then was acquired for 23 hours hourly and daily for another 5 days after injection of pHLIP.

Results: High fluorescent signal was observed in the subcutaneous tumors which reflects elevated pHLIP probe uptake in the tumor region. The maximum fluorescence intensity was observed 1 hour post-injection. Fluorescence signal was significant for up to 4 hours in regions of the brain, spine, and kidneys. At 24 hours fluorescence intensity in tumor region was high, and the signal from kidneys was still detectable. The highest tumor to muscle tissue ratio was 24 hours post-injection. 95% of the fluorescent signal in the body was washed out 4 days post-injection.

Conclusions: pHLIP presents a useful tool to target acidic tissue environments. The pH-sensitive nanoprobe demonstrated good tumor-targeting properties in breast cancer xenografts *in vivo*. pHLIP is non-toxic to cells hence can be used as a cancer drug carrier to reduce the side-effects associated with chemotherapy. Therefore, this novel pH-sensitive peptide has the potential for targeted drug delivery, detecting small tumors, performing diagnostic imaging, and treating acidic disease tissue.

7.   Lin S, Korotcov A, Wu CS, Oh L, Wang PC. **In vivo and ex vivo brain and spine magnetic resonance imaging in multiple sclerosis mouse model. Howard University College of Medicine, Research Day Symposium, April 13, 2012**

Title: *In vivo* and *ex vivo* brain and spine magnetic resonance imaging in multiple sclerosis mouse model

Authors: Stephen Lin, Alexandru Korotcov, Jay Wu, Paul C Wang, Department of Radiology

Background: Multiple sclerosis (MS) is an autoimmune disease that is characterized by the demyelination of white matter in the brain and spine, resulting in greatly impaired signal conduction. The development of an *in vivo* magnetic resonance imaging (MRI) method that can be used to identify and quantify MS lesions will allow the longitudinal monitoring of disease progression as well as therapy.

Methods: Mice with experimental autoimmune encephalomyelitis (EAE) were used as an animal model for MS. For *ex vivo* MRI, EAE and naïve mice were sacrificed and perfused, and brain and lumbar section of the spine were harvested.

The brains and spines were imaged in a 9.4T vertical bore MRI (Bruker Biospin, Billerica, MA). *Ex vivo* and *in vivo* axial and coronal brain images, and *ex vivo* axial spine images were acquired using a rapid acquisition with refocused echoes (RARE) spin echo imaging sequence, with TE=20ms, TR=1500-3000ms, echo train length=4. *Ex vivo* images were acquired with a voxel size of 40μm×40μm with a slab thickness of 300μm, using 128 averages. *In vivo* images were acquired with a voxel size of 78μm×78μm with a 1mm slab thickness, using 32 averages.

Histological slices were acquired from one of the spines used in the *ex vivo* imaging. CD3 and myelin basic protein immunohistochemical staining was performed to identify regions of inflammation and demyelination, respectively.

Results: Comparing the high resolution *ex vivo* EAE spine images with the naïve spine images revealed multiple hyperintense areas, possibly indicating a demyelinated lesion caused by EAE. A slice in the corresponding MRI was identified and a 40μm×20μm demyelinated region in the histological image was found to be co-localized with the hyperintense region in the MRI.

The *ex vivo* high resolution MRI sequence resulted in Signal-to-Noise ratios (SNRs) in the grey matter (GM) and white matter (WM) of 17.03, and 10.67, respectively while the *in vivo* MRI sequence resulted in SNRs of 17.12 and 7.37. The GM/WM contrast ratio for the *ex vivo* MRI was 1.66 and the GM/WM contrast ratio in the *in vivo* MRI was 1.19.

Conclusions: The comparison of the *ex vivo* images to histology suggests that the GM/WM contrast and SNR achieved in the MRI were high enough to allow visual identification of suspected lesion regions. *In vivo* imaging demonstrated that GM/WM contrast and SNR comparable to *ex vivo* imaging could be acquired, albeit with decreased resolution. A lesion with similar dimensions to the one identified in the high resolution *ex vivo* image would appear as an 5×2 pixel lesion, which could still be identifiable. These results highly suggest the ability of *in vivo* and high resolution *ex vivo* MRI to detect and track the progression of disease in a MS mouse model.

Please make your selection:

Topic Category: Theme __2__

Preferred Presentation: x Oral   ☐ Poster

Study of TOPO-Quantum Dot Degradation by ^{31}P NMR

Paul C. Wang[1,*], Tongxin Wang[1,2], Alexandru V. Korotcov[1], Rajagopalan Sridhar[3],
Yue Chen[1], James Mitchell[2]

[1]Molecular Imaging Lab, Department of Radiology, Howard University, Washington, DC
[2]CREST Center for Nanomaterials, Howard University, Washington, DC
[3]Department of Radiation Oncology, Howard University, Washington, DC
Email: pwang@howard.edu

Purpose: The commonly used trioctylphosphine oxide (TOPO) coated semiconductor quantum dot nanocrystals (QDs) for biomedical imaging, may be unstable under physiological conditions because of ligand exchange between QDs and reactive nucleophilic biomolecules. In this study, ^{31}P NMR spectroscopy was used to monitor the interaction between TOPO-QDs and biologically abundant mercapto (-SH) group.

Procedures: Mercaptoethanol was selected to mimic nucleophilicity of biologically abundant protein thiols. In order to monitor the ligand exchange reaction between QDs and thiol, mercaptoethanol (1 mM - 90 mM) was added to the suspension of QDs (56 mg/mL). The ^{31}P NMR spectra were obtained with a 400 MHz Bruker Advance spectrometer.

Results: The ^{31}P NMR spectra of QDs did not display any obvious peak related to phosphorus containing species when the concentration of thiol is very low (less than 10 mM). When the concentration of thiol was 15 mmol/L or more, a sharp peak around 45.5 ppm could be detected indicating that a phosphorus containing species was cleaved from QDs by the action of thiol.

Conclusions: This study demonstrates that TOPO-QDs are relatively unstable and that TOPO can be cleaved from QDs in the presence of a nucleophilic agent such as thiol, which is widely distributed in tissue and physiological fluids. This research provides preliminary information about the potential risk presented by the degradation of TOPO-QDs in physiological systems.
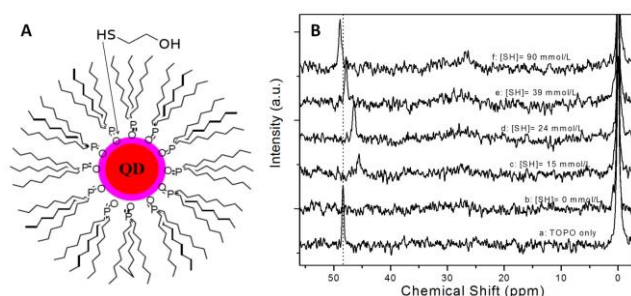
Figure (A) Nucleophilic attack of thiol on TOPO-QDs which leads to cleavage of TOPO from the surface of QDs. (B) ^{31}P NMR spectra of QDs in the absence and presence of different concentration of thiol as well as that of pure TOPO in CDCl3.

1. Bruchez M, Jr., Moronne M, Gin P, et al. Semiconductor nanocrystals as fluorescent biological labels. Science, 1998, 281:2013-2016.
2. Chan WC, Nie S. Quantum dot bioconjugates for ultrasensitive nonisotopic detection. Science, 1998. 281:2016-2018.